Ph.D. DISSERTATION

A Study on Low-Cost, Effective, and Reliable Liquid Crystal Polymer-Based Cochlear Implant System

액정 폴리머 기반의 저가, 고효율, 장기 안정적인

인공와우 시스템에 대한 연구

BY

JIN HO KIM

FEBRUARY 2015

DEPARTMENT OF ELECTRICAL ENGINEERING AND COMPUTER SCIENCE
COLLEGE OF ENGINEERING
SEOUL NATIONAL UNIVERSITY

A Study on Low-Cost, Effective, and Reliable Liquid Crystal Polymer-Based Cochlear Implant System

액정 폴리머 기반의 저가, 고효율, 장기 안정적인 인공와우 시스템에 대한 연구

指導敎授　金 成 俊

이 論文을 工學博士 學位論文으로 提出함

2014年 12月

서울大學校 大學院

電氣컴퓨터 工學部

金 鎭 浩

金 鎭 浩의 工學博士 學位論文을 認准함

2014년 12월

委 員 長 : ____________________________

副委員長 : ____________________________

委　　員 : ____________________________

委　　員 : ____________________________

委　　員 : ____________________________

Abstract

The pace of technological change in implantable devices such as cochlear implants, artificial retinas, and deep brain stimulators has been relatively slow compared to that in other areas, such as memory and mobile phones. Most implantable devices, including cochlear implants, still use bulky titanium electronic packages with complex fabrication processes and wire-based electrodes which are manually fabricated by skilled workers. As a result, the cost of these devices is very high and the widespread use of these devices is limited in low- and middle income countries. Innovative approaches are essential to make implantable devices as affordable as possible while not sacrificing their performance metrics. In this study, we adopt high-performance liquid crystal polymer (LCP) as a backbone for a novel polymer-based cochlear implant. As a material for cochlear implants, LCP enables new capabilities such as miniaturization, a simpler manufacturing process, better long-term reliability, and MRI compatibility, all of which are distinct from the properties of conventional cochlear implants. Moreover, LCP also enables an extremely low-cost device based on mass production with low materials and labor costs.

In this study, we report a fabrication method for the creation of a LCP-based cochlear implant system. Specifically, LCP-based electronics and packaging techniques are addressed in detail. Previous studies of LCP-based packaging use a thermally deformed package cover to secure the electronics cavity and additional laser-cut LCP bonding layers with lower melting temperatures. This method, however, requires additional metal jigs to deform the package cover, and it requires a cavity-filling material such as PDMS. We applied a recessed cavity for the electronics with the stacking of laser-cut LCP multilayers. All packaging layers are composed of the same LCP films, which have a low melting temperature. Thus, the stacked multilayer structure itself acts as a bonding layer. This packaging technology enables the device packaging with a thin credit-card shape for miniaturized, simply fabricated and less invasive devices. Implantable electronics components were also fabricated using copper-clad LCP films with PCB technology. A patterned planar coil was integrated into an LCP electronics board to replace the thick platinum coil of the conventional implant, which is located outside of the metal package. Thus, we can reduce the device dimensions and realize a more efficient receiving coil with greater uniformity. Our group has developed an atraumatic 16-channel LCP-based cochlear electrode array using MEMS technology. This electrode array was used to develop the first functional prototype of an all-LCP-based cochlear implant system.

We also evaluated the effectiveness of the developed LCP-based cochlear implant. The device was implanted into an animal model and the electrically evoked auditory brainstem response was successfully measured. We also verified the MRI compatibility of the LCP-based device compared to a metal-based implant, showing that the developed device has greatly superior MRI compatibility compared to a conventional metal-based device in a 3.0-T and an ultra-high 7.0-T MRI machine.

In order to enhance the long-term reliability of the LCP-based device, we developed novel leak-barrier structures which have a nanoporous surface and microscale barriers with an anti-trapezoidal cross-sectional shape. This structure increases the water leakage path length and improves the mechanical interlocking force between the polymer and the metal layer. The reliability of the leak-barrier structure was determined by accelerated lifetime soak tests (110, 95, 75 ℃). Preliminary results show that both the nanoporous surface and microscale barriers make significant contributions to improving the lifetime of the polymer-based electrode array.

Lastly, we conducted a manufacturing cost analysis of the developed LCP-based cochlear implant system for a better understanding of the detailed cost structure and to determine if the cost could be reduced further. Our group also has experience in the development of cochlear implant systems, including titanium packages and wire-based electrode arrays similar to those in conventional devices, and the system developed by our group had been approved by the Korean FDA. The manufacturing costs of devices developed in the past were also analyzed for a comparison with the cost of an LCP-based device. The analysis revealed that the developed LCP-based cochlear implant has a significantly lower cost with regard to the materials. Also, the manufacturing cost per unit is approximately 10 % of the cost of a titanium-based cochlear implant. Also, the LCP-based device is a batch-processable product that therefore requires less labor. Thus, the manufacturing cost is greatly reduced in proportion to the overall production. This reduction in the manufacturing cost enables disruptive opportunities with regard to the use of cochlear implants in developing countries.

Keywords: cochlear implant, liquid crystal polymer, low-cost, implantable package, hermetic package, long-term reliability, magnetic resonance imaging compatibility, polymer based neural prosthesis

Student Number: 2008-30871

Contents

Abstract ---------- 3

Contents ---------- 7

List of Figures ---------- 11

List of Tables ---------- 21

Chapter 1 Introduction ---------- 22

1.1 Overview of Cochlear Implants ---------- 23

1.2 Review of Cochlear Implant Research ---------- 25

1.3 Challenges for Future Cochlear Implant Systems -- 28

1.4 Proposed Cochlear Implant System ---------- 32

1.5 Objectives of the Dissertation ---------- 36

Chapter 2 Materials and Methods ---------- 37

2.1 System Description ---------- 38

2.1.1 External Speech Processor ---------- 39

2.1.1.1 Hardware Design and Implementation based on Traditional Approach ---------- 39

2.1.1.2 Speech Processing Strategy for Cochlear Stimulation ---------- 43

2.1.1.3 Novel Speech Processor using Smartphone ---------- 46

2.2 Liquid Crystal Polymer (LCP)-Based Implantable Cochlear Implant System -- **49**

2.2.1 Implantable Electronic Module for the LCP-based Cochlear Implant --- **49**

2.2.1.1 Electronics Design --- **49**

2.2.1.2 Electronics Fabrication and Assembly ---------------- **54**

2.2.2 Electronics Packaging for the LCP-based Cochlear Implant --- **57**

2.2.3 LCP-based Thin-Film Cochlear Electrode Array --------- **61**

2.3 System Evaluation -- **63**

2.3.1 Bench-Top Tests of the Fabricated LCP-based Cochlear Implant System --- **63**

2.3.2 Preliminary *In Vivo* Animal Study ------------------------------ **63**

2.3.2.1 Animal Preparation -- **63**

2.3.2.2 Experimental Setup and Protocol --------------------- **64**

2.3.3 *In Vivo* Animal Study -- **66**

2.3.3.1 Animal Preparation -- **66**

2.3.3.2 Improved Experimental Setup and Protocol -------- **67**

2.3.4 Magnetic Resonance Imaging Compatibility Tests ------- **72**

2.4 Leak-Free LCP-based Neural Electrode using Multiple Barrier Structures -------------------------------------- **74**

2.4.1 Test Devices and Sample Categorization --------------------- **75**

2.4.2 Fabrication Methods -- **77**

2.4.3 Electrochemical Characterization of the Electrode ------ 79
2.4.4 Long-Term Reliability Test of the Leak-Free LCP-Based Neural Electrode -- 80
2.5 Manufacturing Cost Analysis ------------------------------------ 85
2.5.1 Overview of the Cost Structure --------------------------------- 85
2.5.2 Comparative Analysis of the Manufacturing Cost of the LCP- and Titanium-Based Cochlear Implants ------------- 87
Chapter 3 Results --- 89
3.1 Fabricated System -- 90
3.1.1 External Speech Processor -- 90
3.1.2 LCP-based Cochlear Implant ------------------------------------ 91
3.1.2.1 Packaging Process --- 91
3.1.2.2 Fabricated LCP-based Cochlear Implant ------------ 94
3.1.2.3 Bench-Top Test of the LCP-based Cochlear Implant --- 96
3.2 *In Vivo* Animal Study -- 99
3.3 Magnetic Resonance Imaging Compatibility -------- 104
3.4 Leak-Free LCP-based Neural Electrode using Multiple Barrier Structures ------------------------------------ 107
3.4.1 Fabricated Electrode -- 107
3.4.2 Characterization of the Electrode ---------------------------- 110
3.4.3 Long-Term Reliability -- 112

3.5 Comparative Analysis of the Manufacturing Cost of the LCP- and Titanium-based Cochlear Implants -- 118

Chapter 4 Discussion --- 127

4.1 LCP-based Electronics Packaging -------------------------- 128

4.2 Comparison of LCP-Based Cochlear Implant to Conventional Metal-Based Cochlear Implant ------ 130

4.3 Effectiveness of the LCP-Based Cochlear Implant -- 132

4.4 Reliability of the Titanium- and LCP-Based Neural Prostheses --- 134

4.5 MRI Compatibility -- 141

4.6 Manufacturing Cost Analysis ---------------------------------- 148

Chapter 5 Conclusion -- 151

References --- 154

Abstract in Korean --- 162

감사의 글 -- 166

List of Figures

Figure 2.1 Conceptual drawing of the liquid crystal polymer (LCP)-based cochlear implant system. LCP circuit board including a receiver coil is monolithically packaged with LCPs. Cochlear electrode array is also fabricated onto the LCP using thin-film microfabrication processes and laser micromachining [51]. Leak-barrier structures can be applied to the polymer-based electrode array for enhanced reliability. ------------------ 39

Figure 2.2 Internal architecture of the external speech processor --------------------- 40

Figure 2.3 Block diagram of the analog front-end for the external speech processor --- 40

Figure 2.4 Simplified schematic of the Class-E amplifier ----------------------------- 42

Figure 2.5 Block diagram of the speech processing strategy for cochlear implant --- --- 43

Figure 2.6 Data telemetry protocol for bit-stream generation which is transmitted to the implantable unit. -- 46

Figure 2.7 Block diagram of the smartphone-based cochlear implant system. -------- --- 47

Figure 2.8 Circuit block diagram of the implantable electronics for LCP-based cochlear implant. --- 50

Figure 2.9 Block diagram of the cochlear stimulator IC. ------------------------------ 51

Figure 2.10 (a) Schematic of the current stimulator (b) Charge balanced biphasic pulse generated by current stimulator. Current flows from Ref to Ch1 (blue arrow) when A_1=0, B_1=1, R_{anodic}=0, $R_{cathodic}$=1, and other channels are off-state. Thus, cathodic current is generated. On the other hand, current flows from Channel 1 (Ch1) to Ref (red arrow) when A_1=1, B_1=0, R_{anodic}=1, $R_{cathodic}$=0, and generates anodic current. --------------- 53

Figure 2.11 CAD designs for three versions of the cochlear electronics. (a) First version of the electronics. Double sided planar coil is located in the upper area. (b) Second version of the electronics. Planar coil is stacked onto the circuit board to decrease the board dimensions (c) Third version of the electronics. Location of contact pads is modified to apply the recessed cavity (third packaging method). The board outline is also changed with consider of location of an alignment magnet as well as high coupling efficiency between coils. ------------------------------------- 56

Figure 2.12 Optimized location of the alignment magnet to become the highest coupling efficiency between RF transmitting and receiving coil. ------ 56

Figure 2.13 (a) Package stack-up of first packaging method. Chip protection guard which is made of 1 mm thick high temp LCP guard is applied to protect interconnection wires of stimulator IC. (b) Packaging condition. ----- 58

Figure 2.14 (a) Package stack-up of the second packaging method and (b) its packaging condition. -- 59

Figure 2.15 (a) Packaging procedure for LCP-based cochlear implant system. (b) Cross-sectional package stack-up, (c) Packaging condition. ------------ 61

Figure 2.16 Implant surgery procedures for the LCP-based cochlear implant. -------- --- 64

Figure 2.17 (a) System setup for EABR recording in the guinea pig implanted with LCP-based cochlear implant. (b) Photograph of the EABR measurement setup. --- 65

Figure 2.18 (a) Improved experimental setup to measure EABR. (b) Photograph of the improved EABR measurement setup. ----------------------------------- 68

Figure 2.19 (a) 'Electrode Test' mode of the Mapping software to control multiple stimulation parameters. (b) Generated biphasic current pulse train and EN_STIM pulses. Inset shows the enlarged view of the single biphasic and EN_STIM pulse. --- 69

Figure 2.20 (a) AUX 4 (Trigger-In) port of the Universal Smart Box of the EABR recording system. (b) SmartEP 4.20 software setting to use external trigger for EABR recording (Stimulus>Modality>eABR). -------------- 70

Figure 2.21 Experimental setup to compare magnetic resonance image artifacts caused by metal- and LCP-based cochlear implants. --------------------- 72

Figure 2.22 Conceptual drawing of the polymer-based thin-film neural electrode and the leak-barrier structure to increase the long-term reliability. Each leak barrier has a nanoporous surface and an anti-trapezoidal cross-section to increase water leakage path length as well as mechanical adhesion force. -- 75

Figure 2.23 (a) Apparatus of the polymer-based electrode used to evaluate long-term reliability. Overall dimensions of the electrode are 9 mm (W) x 103 mm (L), and interdigitated electrodes (IDEs) which have 80 μm width and 100 μm spacing are integrated for leakage current measurements. Dimensions of the working electrode are 800 x 800 μm^2. (b) Test group 1, 2 and 3 from the top to evaluate effectiveness of the leak-barrier structure (Group 1, with a smooth metal surface and without microscale barriers; Group 2, with a nanoporous metal surface and without microscale barriers, and Group 3, with a nanoporous metal surface and with microscale barriers). -- 76

Figure 2.24 Major fabrication processes of a polymer-based electrode with leak-barrier structures. --- 78

Figure 2.25 (a) Accelerated soak test setup. All samples are immersed in the phosphate buffered saline (PBS) at elevated temperatures. Deionized water is continuously supplied to the bath to sustain water levels. During soaking, biphasic current pulses are continuously applied to the electrode site (stimulation parameters: 1 mA in pulse amplitude, 32 μs duration/phase, and 1 kHz pulse rate). Leakage current between interdigitated electrodes are periodically measured using a picoammeter with 5 V dc bias. (b) Interfacing circuit for accelerated soak test. ----- 81

Figure 2.26 (a) Brief circuit diagram of the custom-made multichannel current stimulator for current pulsing during accelerated soak test. (b) Apparatus of the fabricated multichannel current stimulator. ----------- 82

Figure 2.27 Custom-made LabView program for leakage current measurements. ---- --- 83

Figure 2.28 Cost structure. -- 86

Figure 3.1 (a) Developed external speech processor based on traditional approach. (b) PWM data and amplitude modulated signal with 2.5 MHz carrier in Class-E amplifier. --- 90

Figure 3.2 (a) First version of the LCP-based cochlear electronics. (b) LCP encapsulated electronics using first packaging method. (c) Harvested sample after 15 days of soaking in 75 ℃ PBS. Packaged LCP layers were removed to observe the water permeation path. Dashed area shows the traces of water penetration. --- 92

Figure 3.3 (a) Second version of the LCP-based cochlear electronics. (b) LCP encapsulated electronics using second packaging method. Blue arrows indicate the small size wrinkles. --- 93

Figure 3.4 (a) Third version of the LCP-based cochlear electronics. (b) LCP encapsulated electronics using the third packaging method. No observable wrinkles were generated in the package. Dashed box indicate recessed cavity before LCP packaging. --------------------------- 94

Figure 3.5 Developed *LCP- and conventional titanium-based cochlear implant system for size comparison. Inset of the top panel shows the cross-sectional dimensions of two devices. Bottom two panels show conventional wire- and LCP-based cochlear electrode arrays [51]. --- 95

Figure 3.6 (a) Bench-top test setup of the LCP-based cochlear implant. (b) Measured biphasic pulse with 1 kΩ resistive load in air. Amplitude and duration of the stimulation current pulse are set to 1.8 mA and 24 μs, respectively. --- 97

Figure 3.7 (a) Voltage transients in response to the pulse amplitude variation in PBS. (b) Voltage transients in response to the pulse duration variation in PBS. -- 98

Figure 3.8 (a) X-ray image after cochlear implantation to the guinea pig. Inset indicates the enlarged view of the electrode array and interconnection lead. (b) Measured EABR waveform when applying 800 μA, 32 μs biphasic pulse. Stimulus artifact was presented in 0-3 ms, and followed by wave V of the EABR in 4 ms. -- 100

Figure 3.9 Measured EABRs according to varying stimulation amplitude from 1,825 μA to 73 μA when stimulation duration was fixed to (a) 32 μs/phase and (b) 48 μs/phase. -- 102

Figure 3.10 (a) Measured EABRs according to varying stimulation duration from 56 μs/phase to 24 μs/phase when stimulation amplitude was fixed to 1,825 μA. (b) Measured EABRs before and after scarification of the experimental animal. Stimulation amplitude and duration was set to 1,825 μA and 48 μs/phase, respectively. ----------------------------------- 103

Figure 3.11 T1-weighted 3.0 T magnetic resonance images of the head: axial (a) and coronal (b) plane views when the LCP- and metal-based cochlear implants are attached to the left and right side of the head, respectively. Asterisk indicates the side of the LCP-based device. -------------------- 105

Figure 3.12 T2*-weighted ultra-high 7.0 T magnetic resonance images of the head: axial (a) and coronal (b) plane views when the LCP- and metal-based cochlear implants are attached to the left and right side of the head, respectively. Asterisk indicates the side of the LCP-based device. -------- --- 106

Figure 3.13 Micrograph of IDEs (top panels) and bottom-right corner of metal sites (bottom panels) before insulation process. (a) Group 1, (b) Group 2, (c) Group 3. --- 107

Figure 3.14 SEM images of the LCP-based electrode with leak-barrier structure after packaging (Group 3). (a) Top view of the electrode site. Dimensions of the electrode site are 800 x 800 μm^2 (b) Cross-sectional image of the leak-barrier sample. LCP substrate and insulation layer are seamlessly bonded each other. (c) Cross-sectional image (A-A') of the leak-barrier sample. Each leak-barrier has anti-trapezoidal interface for improved mechanical adhesion. (d) High magnification of dashed box of the (c). LCP insulation layer was tightly bonded to the leak-barrier without voids. -- 109

Figure 3.15 Result of the electrochemical analysis. (a) Electrochemical impedance spectroscopy and (b) cyclic voltammogram of the fabricated polymer-based electrode in three test groups. -- 111

Figure 3.16 Result of the highly accelerated soak test in 110 ℃ PBS. Blue line with triangle marker indicates Group 1 sample. Green line with circle marker presents the leakage current curve of the Group 2 sample. Red line with square marker is the result of the Group 3 sample. ---------------------- 113

Figure 3.17 Microscopy images of harvested samples after 110 ℃ highly accelerated soak test. (a), (b) and (c) show the electrode site area (left panels) and IDE part (right panels) of Group 1, 2, and 3, respectively. In right panels of (a) and (b), LCP cover layer was removed. In right panel of (c), LCP cover layer was not removed due to high level of adhesion between LCP cover and metal layer with leak-barrier structure. ------ 114

Figure 3.18 SEM images of test samples harvested after soaking in 110℃ PBS. (a) Cross-sectional image (B-B') of the Group 1 sample, (b) Cross-sectional image (B-B') of the Group 2 sample, (c) Consecutive cross-sectional image (C-C') of the Group 3 sample. In (a) and (b), delamination between LCP cover and metal layer was clearly observed. In contrast, no visible delamination was observed in (c). ----------------------------- 116

Figure 3.19 Ongoing accelerated soak test results in (a) 95 ℃ and (b) 75 ℃ PBS. -- 117

Figure 3.20 Distribution of costs of the (a) titanium- and (b) LCP-based cochlear implants. -- 124

Figure 3.21 Distribution of costs per functional part of the (a) titanium- and (b) LCP-based cochlear implants. -- 126

Figure 4.1 Size of the LCP-based cochlear implant in comparison to commercial devices. Alignment magnet was not considered in the package thickness. The figure was modified from [60]. --- 131

Figure 4.2 Reference EABR waveforms in the guinea pig. (a) and (b) were adopted from [61] and [62], respectively. -- 133

Figure 4.3 Cross-sectional diagrams of (a) titanium- and (b) LCP-based implantable devices. -- 136

Figure 4.4 (a) Cross-section of the test sample with additional titanium layer for adhesion promotion between LCP and metal layer. (b) IDE part of the titanium deposited test sample before lamination. ----------------------- 138

Figure 4.5 (a) Cross-section of the test specimen for XPS analysis. (b) XPS depth profile of the test specimen. -- 139

Figure 4.6 (a)-(c) The XPS spectrum of the O1s, C1s, Ti2p, respectively. (d) Binding energy at the peak point and its binding state. ----------------- 140

Figure 4.7 Illustration of the cochlear implant based on eye glasses type speech processor. Microphone and speech processing module is integrated into the leg or frame of the glasses. Transmitter coil is connected to the end of the frame-leg and interfaced with the LCP-based implantable unit. -- 144

Figure 4.8 (a) Components of the eye glasses type speech processor. (b) Two types of LCP-based implantable unit according to the location of the planar type receiving coil (type 1: stacked coil, type 2: separated coil). (c) How to implant a device based on type 2 coil. ---------------------------------- 146

Figure 4.9 Economies of scale which presents manufacturing cost per unit with varying the volume of annual production from 100 to 10,000. -------- 150

List of Tables

Table 1.1 Physical, chemical, mechanical, and electrical properties of biocompatible polymers (LCP, polyimide, and parylene-C). ---------- 33

Table 2.1 Component list for LCP-based cochlear Implant. ------------------------ 50

Table 2.2 Data decoding criteria for pulse counting logic. ----------------------------- 52

Table 3.1 Size comparison table of the LCP- and titanium-based cochlear implant. -- 96

Table 3.2 Summary of manufacturing cost analysis of the titanium-based cochlear implant. --- 120

Table 3.3 Summary of manufacturing cost analysis of the LCP-based cochlear implant. --- 122

Table 4.1 Gross national income; classifications of developing countries. Adopted from [81]. --- 150

Chapter I

Introduction

1.1 Overview of Cochlear Implants

Neural prostheses are the electronic devices that can replace or restore a nervous system which has been partially damaged by disease, an accident, or through genetics. In general, neural prostheses consist of an external unit which collects signals from the environment and which processes and transmits the signals, and an implantable unit which receives transmitted data/power from the external unit and generates stimulation pulses delivered to an electrode array implanted in the vicinity of the target tissue. Cochlear implants are a type of neural prostheses which can partially restore the hearing in people who have suffered sensorineural hearing loss caused by damage to their hair cells. Hair cells, the primary auditory receptor, are located in the cochlea of the inner ear. Mechanical vibration signals from the outer/middle ear are detected by movements of the stereocilia of the hair cells and are encoded by electric signals which are transferred to the upper auditory pathway. Therefore, hair cells act as a biological transducer. Hair cells can be damaged by drug abuse, continuous noise exposure, infection, and by deafness genes. Most sensory hearing loss is due to poor hair cell function. Also, hair cells do not grow back naturally in mammals. Cochlear implants bypass damaged hair cells in the inner ear and directly interface with the auditory nerve through an electrical link. Cochlear implants also include an external speech processor and an implantable unit, like generic neural prostheses. The external speech processor is composed of a microphone which picks up sounds, a speech processing module which performs frequency decomposition like the biological cochlea, and a transmitter which sends the processed data and power through an inductive link. The implantable unit is composed of a receiving coil which receives signals from the external speech processor, an electronic circuit (or stimulator) which generates electrical pulses according to the received data and which is also hermetically sealed, and a cochlear electrode array which collects the electric pulses from the stimulator and sends them to different regions of the auditory nerve. Cochlear implants are the most successful sensory neural prosthesis. They have helped more than 120,000 people since the first multichannel cochlear implant was approved by the FDA in the 1980s. They have an excellent perception performance rate of 80-90% of average speech in a quiet environment. The delicate structure of the cochlea and innervation of the spiral ganglion cells play a key enabling role in the success of a cochlear implant. The spiral-shaped cochlea has three compartments: the scala vestibule (SV), the scala media (SM), and the scala tympani (ST). The SV and the ST are connected to each other in the apical region of the cochlea, which is called the helicotrema. Hair cells exist in the basilar membrane, i.e., the floor of the SM, and on the roof of the ST as well. The basilar membrane has a narrower width at the base and is wider width at the apex. It is also stiffer in the basal end than in the apex [1]. Due to its gradual change in stiffness, the basal region of the basilar membrane has a higher resonant frequency, while the apical region has a lower resonance frequency. Thus, it acts as a biological spectrum analyzer with its action referred to as tonotopicity. Spiral ganglion cells, which form basis of the auditory nerve, also have the best frequency, corresponding to the characteristic frequency of the basilar membrane. They are, as well, innervated with a spiral shape. The ST naturally provides an optimized space for interfacing with spiral ganglion cells. A multichannel cochlear electrode array is inserted into the ST and electrically stimulates cells to restore hearing artificially. There are three major cochlear implant manufacturers in the world: Cochlear (Australia), Med-El (Austria), and Advanced Bionics (USA).

1.2 Review of Cochlear Implant Research

Developments in the area of cochlear implants have thus far mainly focused on improving the speech processing strategy of the external unit. In the early stage of the development of the cochlear implant, the compressed analog (CA) approach served as the speech processing strategy [2]. In the CA strategy, the signal is initially compressed using an automatic gain control method. The compressed signal is then filtered into multiple frequency bands and converted into a current waveform by multiple current sources. The filtered current waveforms are delivered simultaneously to the intracochlear electrodes in analog form. A major problem with the CA strategy is channel interaction caused by the summation of the electromagnetic fields from individual electrodes. The stimulus waveform is distorted by channel interaction and therefore degrades the perception of speech. Wilson et al. developed what is known as the continuous interleaved sampling (CIS) strategy, which uses pulsatile processing [3]. In the CIS strategy, biphasic current pulse trains are delivered to the electrodes in a non-simultaneously pattern to remove channel interaction. They showed that the CIS process provides significantly higher speech perception scores than the CA strategy. The CIS strategy is currently being used in all commercially available cochlear implant devices.

The hardware of the external speech processor is continually reduced relative to the size of the earlier body-worn type. Currently, a behind-the-ear type is possible with advances in VLSI technology. In 2013, Med-el GmbH (Austria) launched the Rondo processor, which combines the coil, signal processor, and battery pack into a single unit, which is directly attached to the head without an extra cable. In 2008, Cochlear Ltd. (Australia) reported speech perception test results using a research prototype of a totally implantable cochlear implant [4]. The totally implantable device has a package-mounted internal microphone, sound processing electronics, and a rechargeable battery. Thus, the device is fully functional without the use of an external secondary device. However, speech perception scores were significantly lower than those of a conventional device due to the reduced sensitivity of the subcutaneous microphone and body noise interference, such as the blood stream or flying hair. The estimated battery lifetime was about six years, and system was bulky and heavier than the conventional device. However, other efforts towards the development of a totally implantable cochlear implant based on bio-inspired acoustic sensor are emerging [5-7]. A bio-inspired sensor (or artificial basilar membrane) mimics the basilar membrane of the biological cochlea. It replaces the conventional microphone and speech processor with a tiny MEMS sensor while maintaining low power consumption and a compact size.

In 2008, Wise et al. developed high-density cochlear implants using silicon-based thin-film technology [8]. Their system uses lithographically defined cochlear electrode arrays which include position-sensing strain gauges and a microprocessor housed in a silicon-glass package. However, this system is not a finished cochlear implant but is rather is a platform for exploring the use of new technology for implanted electronics and electrode arrays.

Also, some efforts have been made to create low-cost cochlear implants. In 1998, Wilson et al. proposed a device based on four inductively coupled coil pairs [9]. In the proposed system, the speech processor had a microphone, a four-channel speech processor, and four-channel transmitting coils, while the implantable unit had only four-channel receiving coils and a four-channel monopolar electrode array. The implantable unit had no active circuits to avoid becoming too expensive, and is used a complicated hermetic sealing process. Their system showed speech perception performance equal to a standard CIS processor in a patient who had an Ineraid device. In spite of the excellent concept of the passive coil system, the system had some limitations. It uses biphasic voltage pulses which are induced by transmitting coils to stimulate auditory neurons. Therefore, the voltage level in the receiving coil varies with the distance between the transmitting and the receiving coil pairs. The amount of charge delivered to the auditory neurons also changes because the electrode impedance varies with time. Moreover, system tends to be bulky and thick due to its multiple coils and the relatively wide spacing between the coils to decrease crosstalk and the large number of coil turns to maintain sufficient inductance. Also, the system lacks a backward telemetry function for impedance measurements given the absence of active electronics in the implantable unit.

In 2007, An et al. reported the design of a simplified cochlear implant system which was intended to overcome the weaknesses of the prior design noted above [10]. Their design utilizes active electronics in an implantable unit. All system options including number of channels, speech processor chip, communication methods, and the functions of the stimulator chip were parsimoniously selected to achieve minimal requirements. They developed a cochlear implant system through academia-industry collaboration to reduce the research and development cost. The system showed speech perception scores similar to those of a standard CIS processor in four subjects with Ineraid devices [11]. It uses a titanium case to seal the active electronics hermetically, as well as a wire-based electrode array.

1.3 Challenges for Future Cochlear Implant Systems

Despite the surprising success of present-day cochlear implants, there remain many problems, such as patient variations, music/tone perception issues, speech recognition in a noisy environment, and sound localization, among others. In terms of these systems, performance improvements and more advanced research efforts have focused on external speech processors thus far. The implantable unit has not evolved significantly since the first multi-channel cochlear implant was developed. The implantable unit of the present-day cochlear implant is composed of a platinum coil, electronic circuits, titanium packages, and an electrode array. Titanium packages are used to protect the electronics from body fluids, and *vice versa*. Although titanium packaging provide excellent hermetic sealing, it tends to be thick and bulky and requires complicated packaging processes such as laser/resistive welding and brazing due to the need for platinum feedthroughs and ceramic plates. Moreover, the system design requires a one-to-one connection from the electrode to the feedthrough and is thereby limited to low-complexity systems [12]. Also conventional cochlear electrode array is fabricated via manual processes involving skilled workers using fine Pt:Ir (90:10) wires, which also limits the integration density of the system. These factors, i.e., the complicated packaging and electrode fabrication processes, the use of noble metals and the labor-intensive manufacturing process, greatly increase the device cost of cochlear implants, which also makes mass production difficult. At present, the device cost of a cochlear implant is around 30,000 USD, not including the implantation surgery and the pre- and post-operative services. Given the obvious need for and proven benefits of cochlear implants, the cost appear to be the main barrier preventing the increased use of this technology [13]. According to a 2005 report by the World Health Organization, 278 million people had moderate to profound hearing impairment in both ears, and 80% of them live in low- and middle-income countries. With an average household income in these countries of less than $1,000, most deaf people cannot afford a cochlear implant. Thus, the development of a low-cost device without compromising its performance is a meaningful research area.

The bulky size of metal package-based cochlear implants is a serious problem in infant patients. Bulky devices require more invasive skin incisions and skull drilling for cochlear implantation. Today, the majority of cochlear implant patients are infants and toddlers, and such patients have thin craniums. In these patients, the dura is frequently exposed during implantation surgery due to the thick implantable receiver-stimulator [14]. Dura exposure may cause cerebrospinal fluid (CSF) leaks or a viral infection of the CSF.

In clinical aspects, another major problem with present-day cochlear implants is their incompatibility with magnetic resonance imaging (MRI) due to the interference between the magnetic field and the metallic package of the implantable unit. Titanium is not a ferromagnetic but a paramagnetic material. Therefore, it does not cause a missile effect under an MR environment but generates image artifacts due to the surface scattering of radio frequency pulses in an MRI machine. These MR image artifacts hinder the diagnosis of brain-related diseases in cochlear implant recipients. Also, MR image artifacts block the use of MRI as a cognitive neuroscience tool or a top-down approach. Such approaches are useful for investigations of neural pathways from the primary cortex to the sensory nerves.

Neural electrodes provide a bridge which connects the electronics module and targeted neuronal cells. In cochlear implants, for example, the multichannel electrode array is placed into the scala tympani of the cochlea and interfaces with tonotopically organized spiral ganglion cells through pulsed stimulation or electrically evoked compound action potential recording. A high-density and multi-functional electrode array is essential for a closer mimicking of a biological sensory system. Recently, polymer-based electrode arrays using thin-film processes have become widely used in many studies for neural applications [15-22]. Microfluidic channels [23-27], optical waveguides [28], and MEMS sensors [29, 30] are integrated into polymer-based thin-film electrodes. Despite the innovative progress in the area of polymer-based thin-film electrodes, they have yet to be implemented in commercial neural implants. The principal reason for this limitation is a lack of long-term reliability of the electrode. Specifically, delamination is the most commonly occurring failure mechanism in polymer-metal-polymer electrodes [31]. Some researchers have focused on adhesion improvements between the polymer substrate and the metal layer. Dean et al. tested a method that enhanced the adhesion of metal onto the polymer substrate according to various surface treatments and showed related chemical bonding mechanisms [32]. They demonstrated that the deposition of a thin film titanium layer after argon ion ablation on a liquid crystal polymer substrate provided sufficient adhesion at the polymer-titanium interface through the formation of titanium carbide, leading to the realization a high yield and ultra-fine pitch traces.

1.4 Proposed Cochlear Implant System

It is not easy to achieve miniaturized, MRI compatible and mass-producible cochlear implants with conventional materials and fabrication technologies using titanium packaging with feedthroughs and a wire-based electrode array. In this study, we aim to develop a novel polymer-based cochlear implant system without increasing the cost or sacrificing the reliability, MRI compatibility, or mass-producibility. With a polymer, we can fabricate a miniaturized device simply using MEMS technologies, which are compatible with mass production processes. Also, wafer-scale high-density electrode fabrication can be readily achieved with semiconductor thin-film processes. Most polymers show similar magnetic susceptibility levels to water and are thus transparent to radio frequencies. As a result, polymers do not generate image artifacts under MRI exposure. Despite these advantages, polymers have not been used in commercial neural prostheses, mostly due to their lower hermeticity levels than metals. Traditionally, polyimide and parylene-C are commonly used in biomedical applications [33-36]. As shown in Table 1.1, however, these polymers show a relatively high water absorption rate. Implantable units are always surrounded by salted body fluids, and polymers with a high water absorption rate degrade in aqueous environments over time.

Table 1.1 Physical, chemical, mechanical, and electrical properties of biocompatible polymers (LCP, polyimide, and parylene-C).

	LCP [37, 38]	**Polyimide** [39]	**Parylene-C** [40]
Melting Temperature (℃)	280~335	>400	290
Tensile Strength (MPa)	270~500	128	69
Young’s Modulus (GPa)	2~10	2.4	3.2
Water Absorption	0.02~0.04	2.8	0.06 ~ 0.6
Dielectric Constant @ 1MHz	2.9	3.3	2.95

In this study, we adopted a high-performance liquid crystal polymer (LCP) as the material for the cochlear implant. LCPs are biocompatible materials which are compliant with the United States Pharmacopoeia (USP) Class VI guidelines and ISO 10993-1 [41, 42]. LCPs are also listed in the FDA Drug Master File (DMF) and the Device Master File (MAF) [43]. Bae et al. showed that LCP/gold microelectrode arrays meet the criteria of biocompatibility as specified by ISO 10993-5 [44]. Currently, LCPs are not used in commercial neuroprosthetic implants, but they are used in numerous surgical instruments, replacing bulky metal instruments to reduce the cost [45, 46]. Stieglitz wrote as follows: “*LCPs were promised to become the new shooting star in neural interfaces due to the low water uptake and the manufacturing technology*” [42]. As noted in the quotation, LCPs have extremely low moisture absorption and permeability rates (0.02 %, see Table 1.1). Therefore, LCPs are referred to as near-hermetic materials. Lee et al. showed that the encapsulation performance levels of LCPs are compared to those of polyimide and parylene-C. Multiple interdigitated electrode (IDE) arrays were patterned and then encapsulated by polyimide, parylene-C, and LCP [47]. All samples were immersed in a 75 ℃ phosphate buffered saline (PBS) solution and the leakage currents between IDE fingers were periodically measured to detect encapsulation failures (failure criteria: leakage current > 1μA). The test results revealed that the polyimide sample failed within 75 days of soaking, contrary to parylene-C, which failed after 115 days of soaking. The LCP encapsulated device was maintained for more than one year. This demonstrates that LCP is capable of superior encapsulation performance compared to other polymers.

Although the moisture barrier properties of the LCP play an important role in the achievement of a long-term reliable implant package, there are still potential water leakage paths. One is the metal site window of the LCP-based electrode. The heterojunction between the metal layer and the polymer insulation layer is the part most vulnerable to the permeation of body fluids, as it can undergo metal corrosion, interconnection failure, and delamination of the electrode. In addition, water can permeate into the package via buried feedthroughs. In this study, we developed a novel leak-barrier structure to mitigate the occurrence of water permeation through the electrode site.

LCP has outstanding electrical properties as a substrate for circuits and RF coils (dielectric constant=2.9, dissipation factor=0.0025). Pham measured the dielectric constant and loss tangent while varying the relative humidity in the range of 20~100% [48]. In polyimide and FR-4 samples, the values of the dielectric constant and loss tangent changed with the humidity, while the LCP samples maintained constant values in all humidity conditions due to the low moisture absorption rate. Based on the outstanding electrical characteristics of LCP, it has been widely studied with regard to RF applications as an encapsulation material for RF MEMS and monolithic microwave integrated circuits (MMICs) [48-50].

The design intent of the system proposed in this study is to create a low-cost LCP-based cochlear implant without compromising the efficacy, reliability, MRI compatibility, and mass producibility characteristics.

1.5 Objectives of the Dissertation

The specific objectives of the dissertation are given below.

(1) The suggestion of an electronics packaging technique for thin and miniaturized LCP-based neural prostheses

(2) The development of an LCP-based cochlear implant based on the suggested packaging techniques

(3) Verification of the efficacy of the developed LCP-based cochlear implant system by measuring the electrically evoked auditory brainstem response and behaviors in an animal model

(4) Verification of the MRI compatibility of the LCP-based cochlear implant system

(5) The suggestion of a novel leak-barrier structure for long-term reliable polymer-based neural prostheses and its evaluation through accelerated ageing tests

(6) A comparative analysis of the manufacturing cost of the LCP-based and conventional titanium-based cochlear implants

Chapter II

Materials & Methods

2.1 System Description

Cochlear implant system consists of an external speech processor that is worn by patients, and an implantable unit for electrical stimulation of the auditory nerve as shown in Figure 2.1. Our group has developed a speech processor with concept of parsimonious design through academia-industrial collaboration [10], and the author was also involved in the development process of the speech processor as well as preclinical trials to verify the device performance. The developed speech processor (namely SNU-NB processor) was used in this study. Device description on SNU-NB processor was provided in the section 2.1.1. Novel system approach to design speech processor based on smartphone was also suggested in section 2.1.1.3.

An implantable unit is located beneath the skin of temporal area of the head, and interfaces with the speech processor through an inductive link. The implantable unit has a receiving coil collecting data and power, a stimulator chip to generate biphasic pulse train, and an electrode array to deliver pulse train to the auditory nerve. In this study, we focused on developing the implantable unit using the LCP material while maintaining small size, low-cost, MRI compatibility, and batch processability. Novel LCP packaging techniques for thin and compact implantable devices were developed and evaluated. The leak-barrier structures for enhancing reliability of polymer-based device were also suggested and verified.

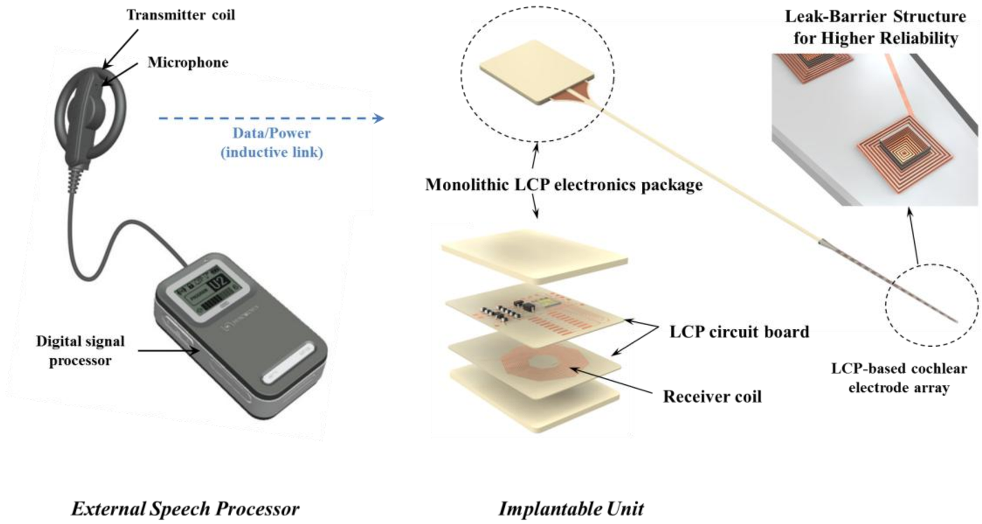

Figure 2.1 Conceptual drawing of the liquid crystal polymer (LCP)-based cochlear implant system. LCP circuit board including a receiver coil is monolithically packaged with LCPs. Cochlear electrode array is also fabricated onto the LCP using thin-film microfabrication processes and laser micromachining [51]. Leak-barrier structures can be applied to the polymer-based electrode array for enhanced reliability.

2.1.1 External Speech Processor

2.1.1.1 Hardware Design and Implementation based on Traditional Approach

The main function of the speech processor is to analyze audio signal picked up by the microphone and send the resulting digital data about stimulation parameters to the implantable unit. The processor also provides user interface to control the system function and indicate the system status. The internal architecture of the speech processor is illustrated in Figure 2.2.

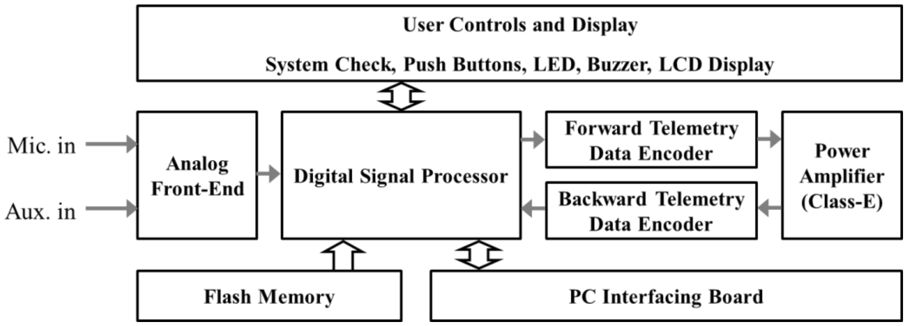

Figure 2.2 Internal architecture of the external speech processor

The analog front-end stage receives audio signals from the microphone or the other audio sources that are connected via the auxiliary input socket. It consists of pre-emphasis filter, first pre-amplifier, bandpass filter, automatic gain controller, and second amplifier, as illustrated in Figure 2.3. The signal from the microphone is delivered to the pre-emphasis filter (high-pass filter, cutoff frequency: 1.2 kHz, gain=1) for attenuation of strong and not very informative components below 1.2 kHz, and then amplified by first pre-amplifier with a gain of 17. The amplified signals are passed by unity-gain 4^{th}-order Butterworth bandpass filter to extracts a significant speech information in a frequency range of 300~8,000 Hz. Then, the second amplifier gives a gain of 1.8 to the filtered signals and finally delivered to the digital signal processor (DSP) chip.

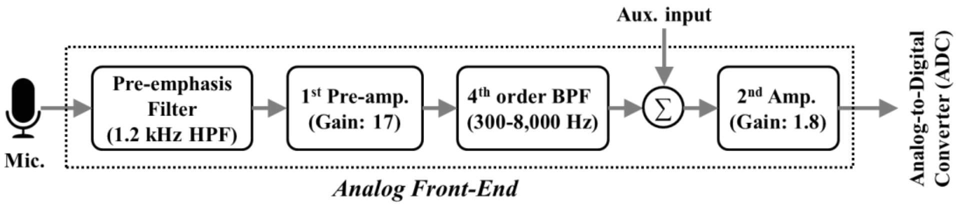

Figure 2.3 Block diagram of the analog front-end for the external speech processor

The DSP is the nucleus of the external speech processor. It performs a digitization of the pre-processed audio signal, and real-time frequency decomposition on the digitized audio signal. Developed speech processor uses a 16-bit TMS320VC5509A model (Texas Instruments Inc., Dallas, TX, USA) due to high performance, low power consumption, multiple general-purpose I/O (GPIO), and built-in analog-to-digital converter (ADC). According to the speech processing algorithm of the DSP, it determines the stimulation parameters such as how much current into what electrode. The detailed speech processing algorithm of the DSP chip will be described in section 2.1.1.2.

The forward telemetry encoder converts binary digital data into pulse width modulation (PWM) coded digital data frames. One data frame is composed of total 15 binary bits including 13 bits for stimulation and mode controls, 1 bit for parity check, and 1 bit for the end-of-frame. And data rate is about 120 kbps (8,000 frames/sec x 15 bits/frame). For backward telemetry, the system uses a load modulation method. The backward telemetry decoder decodes the peak voltage of transmitter coil to digital signal and transfers the decoded data to the GPIO of the DSP.

The Class-E amplifier was adopted to convert the data frame into a form that can be transmitted to the implantable unit. In general, Class-E amplifier shows significantly higher efficiency than conventional Class-B or –C amplifiers. In Class-E, the transistors operates as an on/off switch and the load network shapes the voltage and current waveforms to prevent simultaneous high voltage and high current in the transistor that minimizes power dissipation, especially during the switching transitions. The schematic of developed Class-E amplifier used in the speech process is illustrated in Figure 2.4. The circuit modulates the PWM-encoded data to 2.5 MHz carrier frequency and transfers the modulated signals and power to the implantable unit through an inductive link. A high level of the PWM-encoded signal is 3.3 V and a low level is 0 V. The range of input signals is scaled up to the level of 40 V_{PP} by a miniature transformer (5:50).

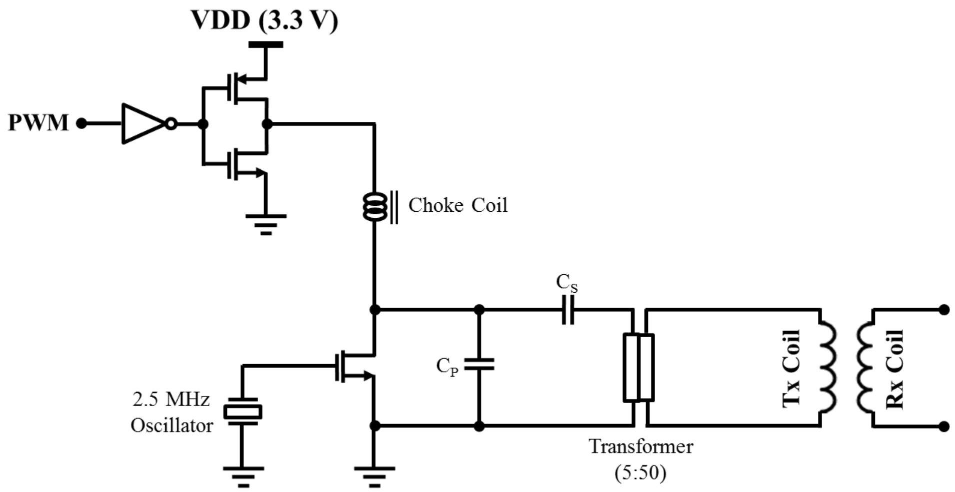

Figure 2.4 Simplified schematic of the Class-E amplifier

2.1.1.2 Speech Processing Strategy for Cochlear Stimulation

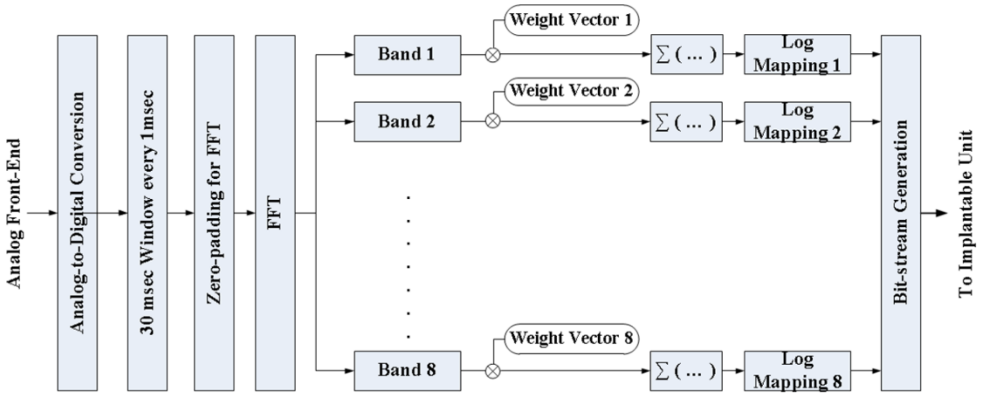

Figure 2.5 Block diagram of the speech processing strategy for cochlear implant

The speech processor implements 8-channel CIS strategy to analyze the speech input signal and to generate data frame delivered to the implantable unit. Overall speech processing strategy is briefly illustrated in Figure 2.5. First, the DSP performs an analog-to-digital conversion on the output signal from the analog front-end stage using a built-in 10-bits ADC. According to the bandwidth of a speech signal, the sampling rate of the ADC is set to be 16 kHz. Digitized signal was segmented by 30 ms (480-points) hamming window with sliding span of 1 ms. Sliding span (or overlap size between windows) on the time axis decides the amount of the smoothing on the frequency axis. In other words, higher overlap size reduces the fluctuation on the spectral energy. The DSP performs a 512-points real-term Fast Fourier Transform (FFT) from the hamming windowed signal (30 ms, 480-points) with an update period of 1 ms. For FFT, hamming windowed signal was zero-padded to make 2^9 (512) samples. Then filter bank calculation extracts energy of power spectrum for eight channels. In this process, weight vector was multiplied to the extracted spectral energy of each channel to make sloped filter skirt. Weight vector array was pre-defined and stored in a form of table within extra flash memory of the speech processor. Calculated spectral energy per FFT index (256-points) of the each frequency band is added up. After calculation of the spectral energy, log-mapping was applied to determine the final amplitude level per channel. The log mapping is necessary for compressing dynamic range of the acoustic signal into electrical amplitudes between threshold level (T-level) and the most comfortable level (C-level). In conversational speech, the acoustic amplitudes may vary over a range of 30 dB [2]. Developed speech processor has dynamic range of 50 dB, range from 40 dB Sound Pressure Level (SPL) to 90 dB SPL. Implantable listeners, however, may have a dynamic as small as 5 dB [2]. Thus, log mapping provide dynamic range matching of the loudness between acoustic and electrical amplitudes. The following equation is used to determine the final stimulation levels.

$$y = Ax^{p} + B$$

where,

$$A = \frac{C - T}{x_{max}^{p} - x_{min}^{p}} \quad , \quad B = T - Ax_{min}^{p}$$

Above equation shows the relation of sound input (x) and the final electrical stimulation level (y). The x_{min} and x_{max} are the mean minimum and maximum values of acoustic dynamic range, respectively. The A and B are constants determined by C-level (C) and T-level (T). The steepness of the log mapping curve can be controlled by varying the value of the exponent p. The T-and C-levels are defined differently for each channel. Real-time calculation based on above equation in all channels requires extremely huge operations in the DSP. Therefore, we adopted pre-defined look-up table stored in the external flash memory to reduce the operation quantity as well as computational time. After calculating stimulation level of the channel, bit-stream is generated according to customized data protocol between external processor and implantable unit as illustrated in Figure 2.6. A bit-stream (or data frame) consists of 15 binary data bits, and there are four possible modes that are determined by the first 3 bits in the frame (Figure 2.6). In the case of MODE 00, first 3 bits of the frame is ‘000’. MODE 00 data frame contains information about stimulation duration and stimulation mode (Bipolar/Monopolar). In the case of MODE 01, first 3 bits of the frame is ‘001’. MODE 01 data frame is sent to the integrated circuit when the supply voltage of the integrated circuit needs to be checked. In the case of MODE 10, first 3 bits of the frame is ‘010’. MODE 10 data frame is sent when the electrode impedance needs to be recorded. MODE 11 data frame whose first 3 bits is ‘011’ is sent when the crosstalk between the electrodes needs to be checked. Stimulation command frame determines the stimulation electrode and the stimulation current amplitude. Finally waiting command frame is used when the speech processor is waiting the response of the implantable unit. Each data frame ends with ‘end of frame’ bit that follow even parity bit.

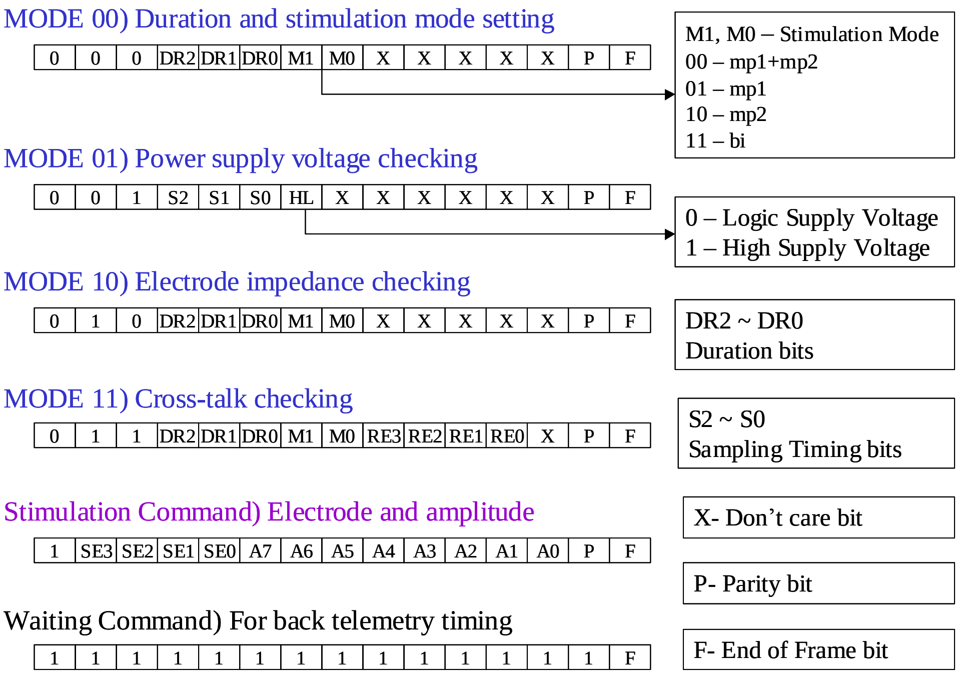

Figure 2.6 Data telemetry protocol for bit-stream generation which is transmitted to the implantable unit.

2.1.1.3 Novel Speech Processor using Smartphone

Traditional approach to develop customized external speech processor using DSP was described in previous section. We adopted commercially available DSP chip to decrease the cost for developing customized processor. Present cochlear implant manufacturers use DSP chips from semiconductor IP core vendors such as CEVA, AMIS, VeriSilicon, and Freescale through very expensive licensing agreements (about million dollars). We can cut down expenses for chip licensing by adopting generic DSP chip. However, the external device based on traditional approach still requires bulky extra speech processor that has to be attached to the patient's head nearby implantable unit. As a result, it limits the use of the device during hard exercise or sleeping. In this study, we suggest a novel speech processor using a smartphone to overcome aforementioned limitations. Present-day smartphones already have an integrated microphone for detecting speech signals, high-performance microcontroller for signal processing, and wireless data transceiver for delivering data packet to the implantable unit. In addition, they provide easy and powerful platform to develop custom applications. Thus, constitution of the smartphone fits well with requirements for the conventional speech processor of the cochlear implant.

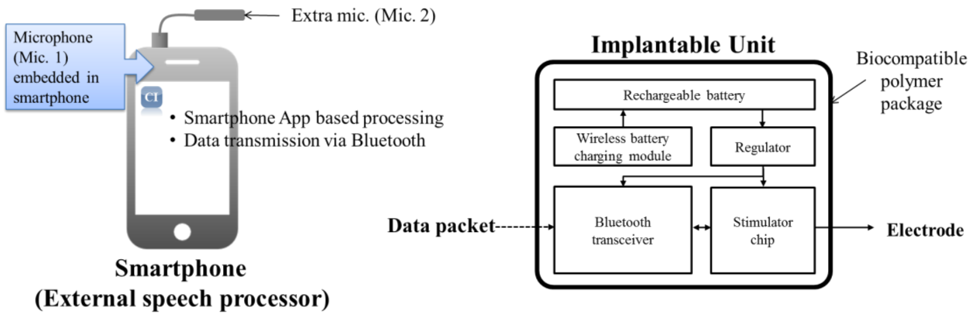

Figure 2.7 Block diagram of the smartphone-based cochlear implant system

Figure 2.7 shows the block diagram of the cochlear implant system based on the smartphone. The system uses smartphone application (hereafter app)-based signal processing, and the identical speech processing algorithm as shown in Figure 2.5 can be used. First, sound was picked up by a microphone integrated into the smartphone or by an extra microphone connected to the I/O terminal. The extra microphone with cable provides convenience to the recipients by properly locating the miniature microphone nearby sound sources. When app is running, signals from the microphone is continuously processed through embedded microcontroller, and then the controller generates data packets. The data packets are transmitted to the implantable unit through an embedded Bluetooth transceiver instead of an inductive coupling, and it enables expansion of communication distance from 10 mm (in case of inductive coupling) to several tens of meters. Therefore, the patient does not have to wear the device near the implantable unit.

For using smartphone as a speech processor and a transmitter of the cochlear implant, the implantable unit also has an additional power source such as a rechargeable battery, battery charging module, and Bluetooth transceiver. The rechargeable battery is periodically charged through an inductive coupling, and the Bluetooth transceiver receives the data packet transmitted from the smartphone. Stimulator chip generates biphasic pulse trains according to the decoded data packet.

2.2 Liquid Crystal Polymer (LCP)-Based Cochlear Implant System

2.2.1 Implantable Electronics Module for the LCP-based cochlear implant

2.2.1.1 Electronics design

A circuit block diagram of the implantable electronic module for LCP-based cochlear implant is illustrated in Figure 2.8. The electronics consist of a receiver RF coil, a tuning capacitor, a load modulation circuit for a backward telemetry, two half-wave rectifiers, a high-pass filter for DC offset cancellation, a Zener diode for the over-voltage protection, a capacitor for the supply voltage regulation, and the current stimulator IC. A 2.5 MHz RF modulated PWM signal is delivered to the receiver coil through a transmitter coil of the external speech processor described in section 2.1.1.1. The signal is divided into two pathways by two half-wave rectifiers: one is a path for regulated power supply, and another for data extraction. In the power supply pathway, half-wave rectified signal was regulated by capacitor, and maximum voltage was limited using a Zener diode (16 V) to prevent stimulator IC breakdown caused by excessive DC voltage. As a result, about 10 V DC was supplied to the stimulator IC. In the data pathway, half-wave rectified signal was high-pass filtered for removing undesired DC offset from RF modulated PWM signal. Demodulated PWM signal was directly applied to the stimulator IC. The electronic components used in this study are listed in Table 2.1. All components are carefully selected considering its dimensions, thickness to realize a thin and small sized implant package. The maximum thickness of the components is as small as 1 mm. Degradation temperature of the components is also reviewed to protect them from the subsequent packaging temperature. We tested and confirmed that selected electronic components endure 300 ℃ during 30 min.

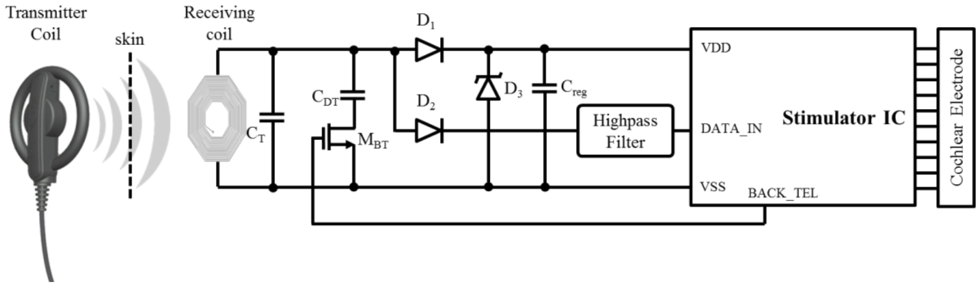

Figure 2.8 Circuit block diagram of the implantable electronics for LCP-based cochlear implant

Table 2.1 Component list for LCP-based cochlear implant

Part No in Figure 2.8	***Role***	***Model***	***Package Type***
D_1	Half-wave rectifier	SDMP0340LAT	SOT-523
D_2	Half-wave rectifier		
D_3	Stimulator IC protection	MM3Z16VST1	SOD-323
C_T	Coil tuning	300 pF	0603
C_{DT}	Coil detuning in backward telemetry mode	100 pF	0603
C_{reg}	Voltage regulation	1 μF	0603
M_{BT}	Switch for backward telemetry mode	DMG1012T	SOT-523

Previously, our group has reported the details of the stimulator IC [10, 52]. We used identical stimulator IC for newly developed LCP-based cochlear implant. Detailed block diagram of the IC and functions of each block are described below. Figure 2.9 depicts the simplified block diagram of the stimulator IC. Data decoder consists of envelope detector and pulse counting logic circuit. The envelope detector generates a 0-5 V clock signal using input RF modulated PWM signal, and then the pulse counting logic counts the number of pulses during envelope extraction. The number of pulses is decoded into digital data (0, 1, end-of-frame (EOF)). For example, when the number of pulses in the burst is 5, digital data means ‘0’. When the number of pulses is 10, the data means that it is the end of the frame. When the number is 15, the data means ‘1’. Marginal pulses (+/- 2 pulses) was considered to the binary data decoding, because detected number of pulses may be varied by changing distance between transmitting and receiving coils. Data decoding criteria for pulse counting logic is summarized in Table 2.2.

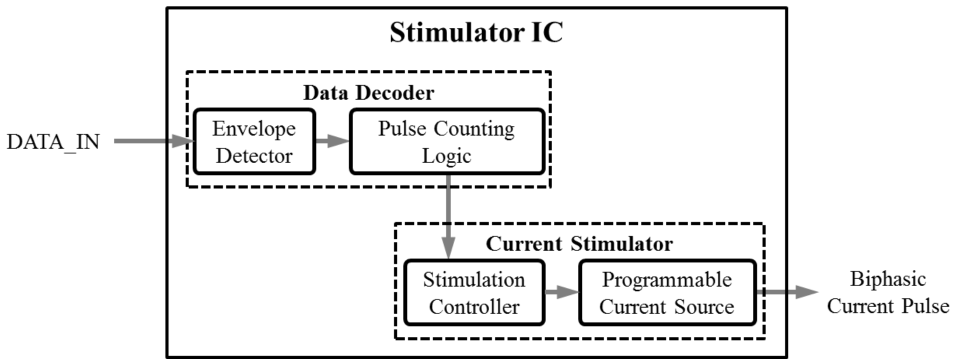

Figure 2.9 Block diagram of the cochlear stimulator IC

Table 2.2 Data decoding criteria for pulse counting logic

Number of Pulses	***Meaning of Digital Data***
<3	Error
3-7	Binary '0'
8-12	End of frame
13-17	Binary '1'
>17	Error

Decoded binary data frame is used to produce biphasic current pulses. Current stimulator consists of stimulation controller and programmable current source. Circuit diagram of the current stimulator is illustrated in Figure 2.10 (a). The stimulation controller generates bidirectional current pathway by controlling MOS switches' on/off status and timing. Pulse polarity and duration are determined by stimulation controller. In the Figure 2.10 (a), $R_{cathodic}$ and B_1 are on and all other MOS switches are off, current flows from reference to channel 1 electrode. Thus, cathodic current is generated in terms of channel like a blue arrow in Figure 2.10 (a). Also, 'A_1 and R_{anodic}' are on, and other switches are off, current flow from channel 1 to reference. And it generates anodic current like a red arrow in Figure 2.10 (a). Also, duration of on status determines the stimulation pulse duration per phase. Figure 2.10 (b) shows the example of the charge balanced biphasic pulse generated by the current stimulator.

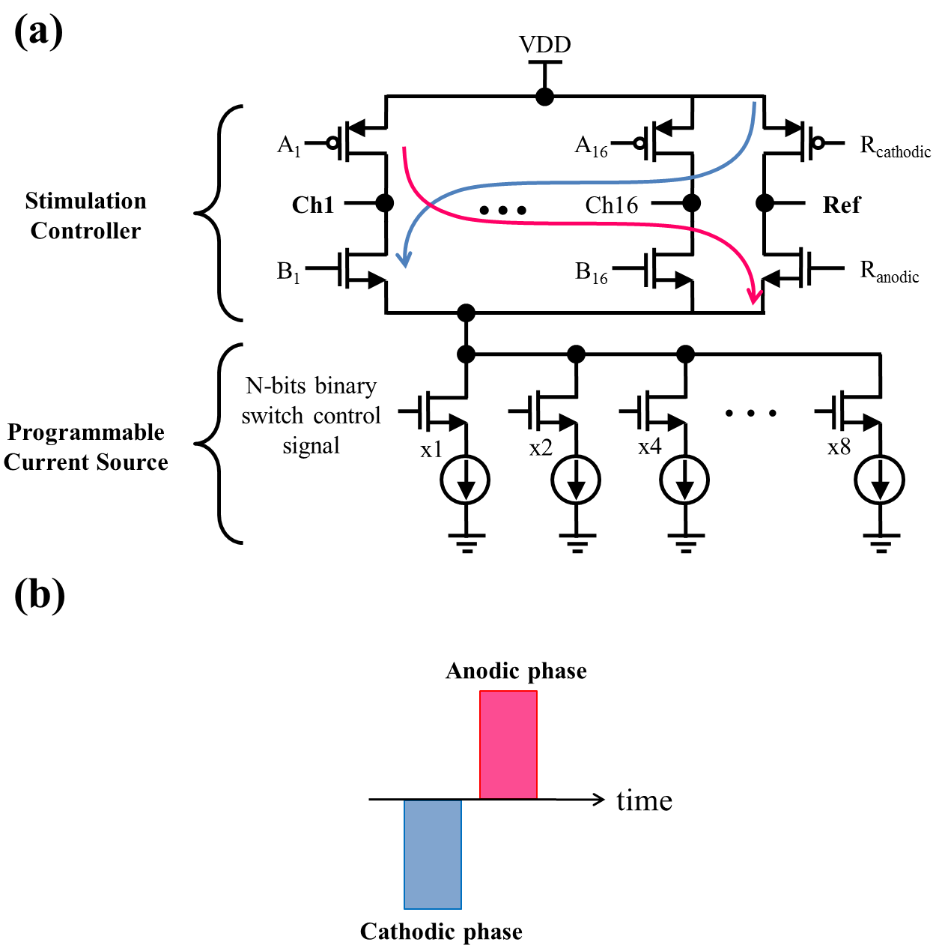

Figure 2.10 (a) Schematic of the current stimulator (b) Charge balanced biphasic pulse generated by current stimulator. Current flows from Ref to Ch1 (blue arrow) when A_1=0, B_1=1, R_{anodic}=0, $R_{cathodic}$=1, and other channels are off-state. Thus, cathodic current is generated. On the other hand, current flows from Channel 1 (Ch1) to Ref (red arrow) when A_1=1, B_1=0, R_{anodic}=1, $R_{cathodic}$=0, and generates anodic current.

Also, amplitude of the biphasic pulse is determined by a programmable current source. It comprises switchable eight constant current sources that current values are increase by multiples of two. Thus, 256 (=2^8) levels of the stimulation current level are implemented using a combination of switches' on/off status. Figure 2.10 (b) shows the example of the charge balanced biphasic pulse generated by current stimulator. Generated biphasic pulse trains are transmitted to the electrode array for stimulation of the auditory neurons. Designed stimulator IC is fabricated in Austria Microsystems (AMS) 0.8 μm high voltage CMOS (CXZ) process.

2.2.1.2 Electronics fabrication and assembly

Three versions of circuit board depicted in Figure 2.11 were fabricated using copper clad LCP films. The circuit board was revised according to the modification of electronics packaging techniques which will be described in section 2.2.2 and miniaturization as well. All electronics are fabricated using copper clad LCP films (R-F705T, Panasonic Corp., Japan) which have high melting temperature (high temp LCP, T_m=310 ℃) using flexible PCB technology.

Figure 2.11 (a) shows the CAD design for the first version of the LCP circuit board. Double sided planar coil is located in the upper area, and multiple pads for electronic components and interconnection lines are placed in the lower area. The second version of the LCP circuit board was fabricated utilizing a multilayered structure for miniaturization as illustrated in Figure 2.11 (b). Double-sided planar coil and metal pads including interconnection lines are fabricated on separate LCP films. Two layers of LCP films are stacked and bonded each other with a low-temp LCP film (CT-F, Kuraray Co., Japan) or an adhesive layer (NC0204, Namics Co., Japan), and electrically linked each other through blind vias.

Final version of the LCP circuit board is illustrated in Figure 2.11 (c). In this version, placements of the electronic component are slightly changed according to the modification of the LCP packaging method. Components are densely placed to allow packaging based on a recessed cavity. Also, the board outline was slightly rearranged with consider of alignment between transmitting and receiving coils for higher coupling efficiency. Figure 2.12 shows the optimized location of the alignment magnet to become the highest coupling efficiency between two coils. The magnet will be placed surface of the LCP package after packaging process, and then molded with silicone elastomer with a magnet pocket.

Discrete components listed in Table 2.1 are assembled to the fabricated circuit board using a biocompatible silver paste (EPO-TEK H20E, Epoxy Technology Inc., MA, USA) which meets USP Class VI criteria. Stimulator IC was wire bonded to the circuit.

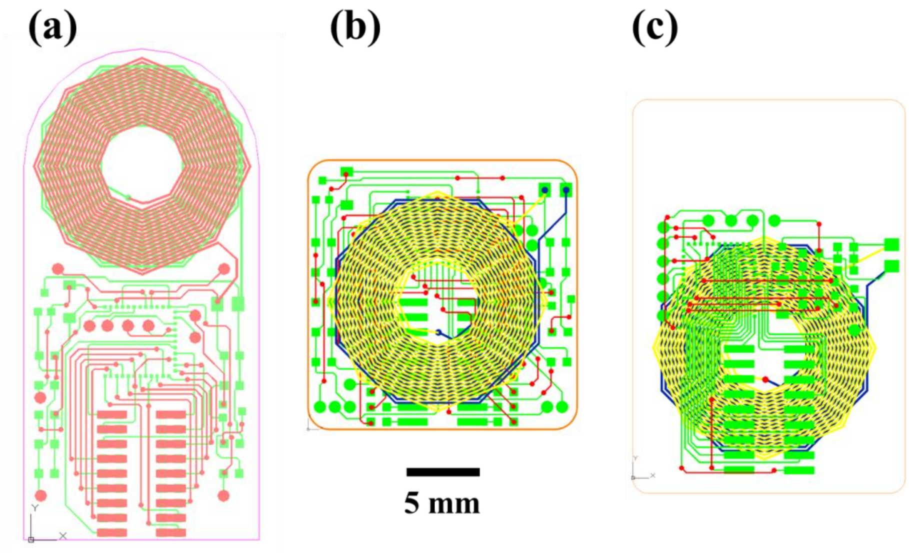

Figure 2.11 CAD designs for three versions of the cochlear electronics. (a) First version of the electronics. Double sided planar coil is located in the upper area. (b) Second version of the electronics. Planar coil is stacked onto the circuit board to decrease the board dimensions (c) Third version of the electronics. Location of contact pads is modified to apply the recessed cavity (third packaging method). The board outline is also changed with consider of location of an alignment magnet as well as high coupling efficiency between coils.

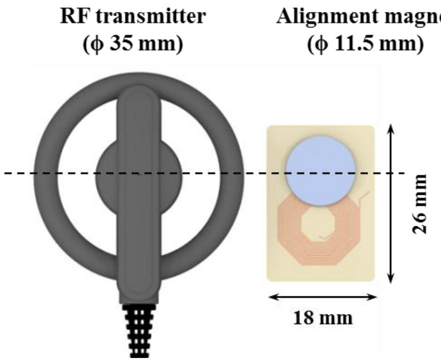

Figure 2.12 Optimized location of the alignment magnet to become the highest coupling efficiency between RF transmitting and receiving coil.

2.2.2 Electronics Packaging for the LCP-based Cochlear Implant

Assembled electronics are monolithically packaged with LCPs. Conventionally, high temp LCPs are used to package lid and substrate, and low temp LCP layer (T_m=280 ℃) is used as an adhesion layer [47]. In conventional packaging method [47], package lid is thermoformed using a couple of aluminum jig before lamination process. In this study, we used low temp LCP films only instead of combinations of high temp and low temp LCPs. Therefore, we omitted the pre-shaping of package cover to achieve thin card-shaped package. Three packaging methods are suggested and evaluated. First packaging method uses 16 layers of 50 μm thick low temp LCP film as a package cover, and 4 layers of 50 μm thick LCP films as a package substrate as shown in Figure 2.13 (a). The feature of the package stack-up is the application of chip protection guard which is made of 1 mm thick high temp LCP. The guard is affixed around the stimulator IC, and protects interconnection wires of stimulator IC from vertical mechanical stresses during lamination process. Thickness of stimulator IC is about 500 μm, and thus it does not affect the increase of final package thickness. Teflon films are applied to the top and bottom side as a release layer after packaging. Also, 2 mm thick ceramic paper covered by aluminum foil is applied to the top side for the mild press of the electronic components. Package stack-up is pressed by custom-made aluminum press jig. Aforementioned packaging method is applied to the first version LCP electronics. Package stack-up is laminated each other using thermal press (Model 4122, Carver, Wabash, IN, USA). Packaging condition is illustrated in Figure 2.13 (b). First, package stack-up is preheated at 150 ℃ for 30 minutes, which is followed by fusion bonding process at 285 ℃ for 20 minutes. Low temp LCPs have 280℃ of melting temperature, and thus they become molten state and bonded each other by interdiffusion of polymer molecules. The temperature is increased the speed of 7 ℃ per minutes, and naturally cool down to the room temperature. The pressure is uniformly applied to the mold maintaining 20 kg.

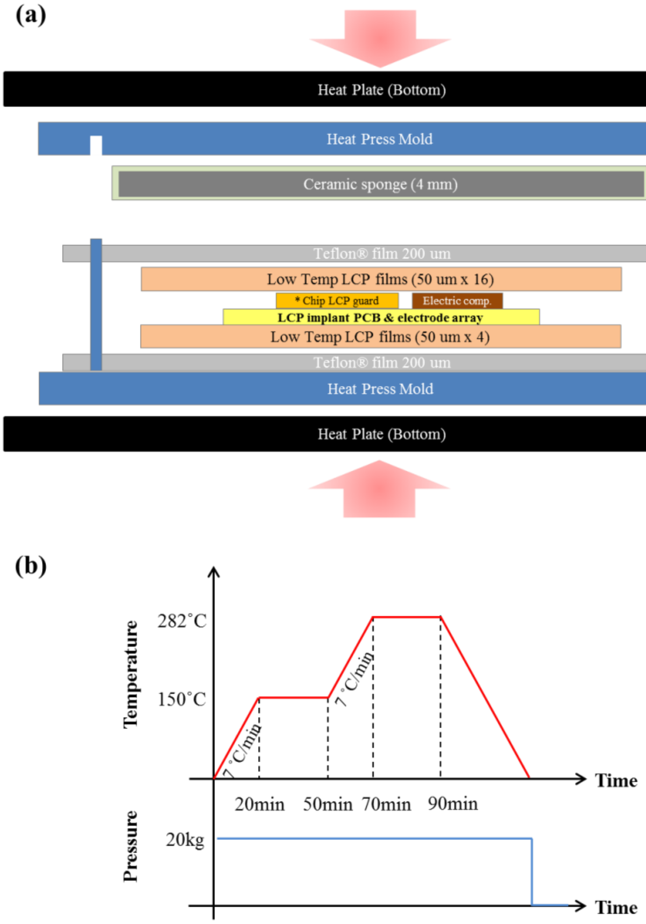

Figure 2.13 (a) Package stack-up of first packaging method. Chip protection guard which is made of 1 mm thick high temp LCP guard is applied to protect interconnection wires of stimulator IC. (b) Packaging condition.

Figure 2.14 (a) shows the modified package stack-up for the second packaging method. The notable change of the package stack-up is a structure of the top plate of press jig. It is designed for the localized press on the circuit board outline. In the second packaging method, pressure for thermal lamination of LCP films has increased from 20 kg to 70 kg. Other setup is identical to the first packaging method.

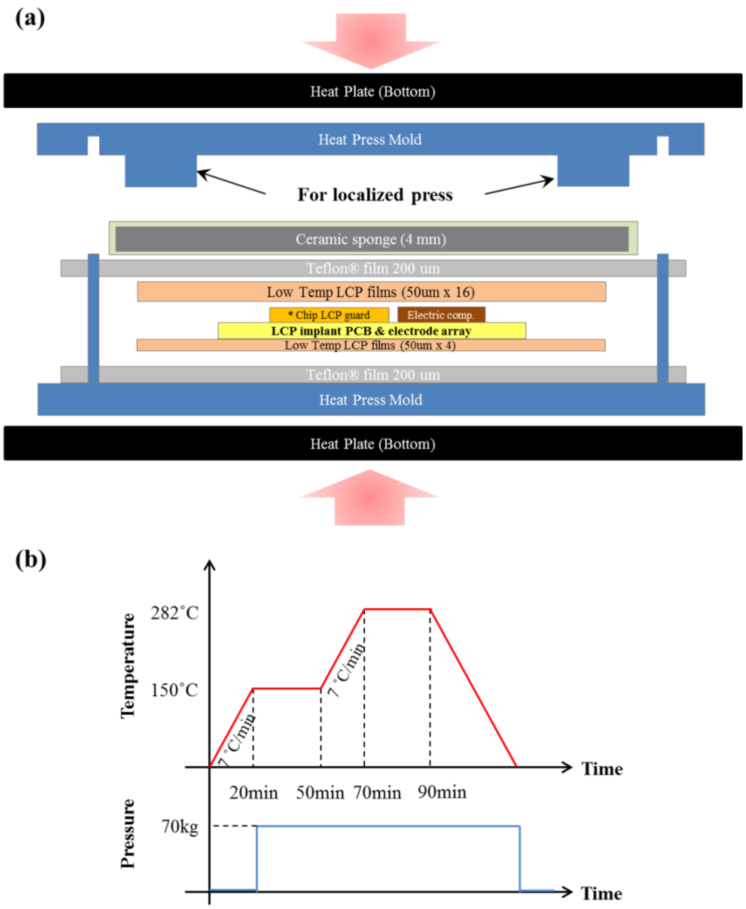

Figure 2.14 (a) Package stack-up of the second packaging method and (b) its packaging condition.

Figure 2.15 (a) shows the step by step processes of final packaging method. First, aluminum mold is prepared which has alignment pins for LCP film insertion, and then bottom laser-cut 100 μm thick LCP film is placed onto the bottom plate of the mold. Second, electronic board with cochlear electrode array is placed onto the bottom LCP film. Third, twelve layers of 100 μm-thick low temperature LCP films which have laser-cut cavity for electronic components are placed onto the electronic board. By stacking multilayers of laser cut LCP films, they create a recessed cavity for electronic components, and provide mechanical protection of electronic components and its interconnection during subsequent packaging procedure. Fourth, laser-cut LCP film which is identical to bottom LCP film is applied, and then top plate of the aluminum mold is covered. Finally, package stack-up is laminated by thermal compression process as illustrated in Figure 2.15 (b). Figure 2.15 (c) shows the packaging conditions of the (b). After final lamination process of LCP, device outline cutting using UV laser machine is applied.

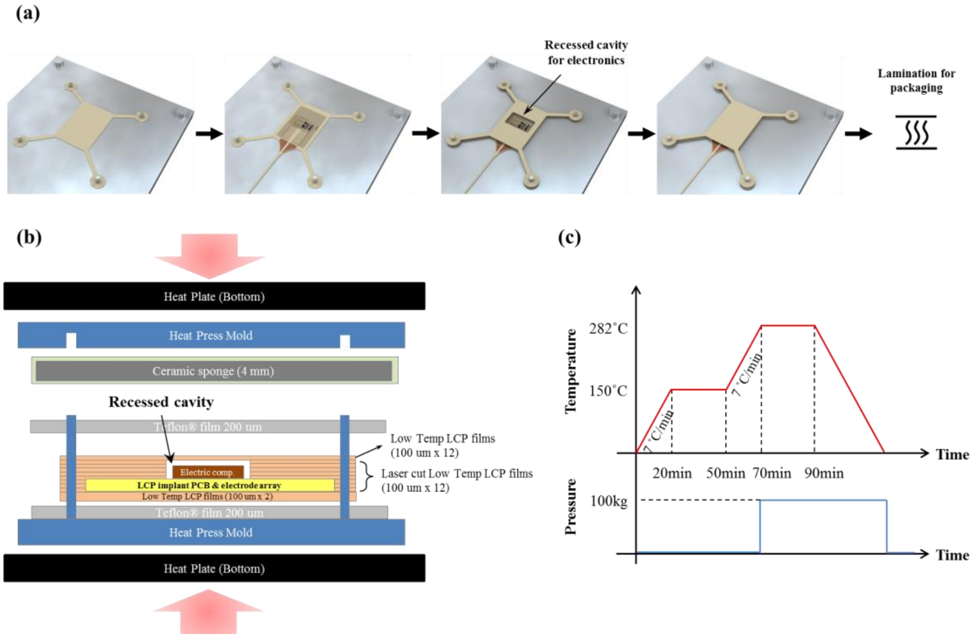

Figure 2.15 (a) Packaging procedure for LCP-based cochlear implant system. (b) Cross-sectional package stack-up, (c) Packaging condition.

2.2.3 LCP-Based Thin-Film Cochlear Electrode Array

Using thin-film process of LCP-film-mounted silicon wafer and thermal press lamination process, Min et al. developed an LCP-based thin-film cochlear electrode array [51]. To reduce the rigidity and increase the flexibility of the electrode, they adopted silicone elastomer encapsulation with self-aligning molding process. They performed five cases of human temporal bone insertion test to verify the mechanical safety of the developed LCP-based cochlear electrode array. Results showed that two cases of human temporal bone insertion showed no observable trauma, whereas three cases showed a rupture of the basilar membrane.

We developed advanced LCP-based cochlear electrode array for further enhancement of flexibility as well as deeper insertion. Multilayered structure with variable layers of LCP films, tapered structure, and peripheral blind via technique were adopted to achieve flexible tip and basal rigidity of the electrode. Flexible tip of the electrode plays an important role in atraumatic insertion, whereas basal rigidity is beneficial for deeper insertion of the electrode. Also, peripheral blind via techniques is helpful to decrease the width of the electrode. Feasibility of the advanced LCP-based cochlear electrode array is verified through human temporal bone insertion study. Five electrode arrays are inserted without trauma at the first turn of the cochlea.

Newly developed advanced LCP-based cochlear electrode array is used to build the LCP-based cochlear implant system. The electrode array is assembled to the fabricated electronics using a biocompatible silver paste (EPO-TEK H20E, Epoxy Technology Inc., MA, USA) before final LCP lamination for packaging.

2.3 System Evaluation

2.3.1 Bench-Top Tests of the Fabricated LCP-based Cochlear Implant System

Functionality of the assembled electronics is verified through bench-top tests while changing multiple stimulation parameters with an external speech processor. Voltage measurement probe pair of the oscilloscope (DPO4054, Tektronix Inc., Beaverton, OR, USA) with differential preamplifier (ADA400A, Tektronix Inc., Beaverton, OR, USA) are connected between designated stimulation site and reference electrode. Biphasic current pulse was measured with 1 kΩ load in air. Also, voltage transients were measured in phosphate buffered saline with changing pulse amplitude and duration. Pulse amplitude was varied from 219 μA to 1.752 mA by 219 μA step, and pulse duration was varied from 8 μs to 56 μs by 8 μs step.

2.3.2 Preliminary *In Vivo* Animal Study

2.3.2.1 Animal Preparation

After checking the functionality of the fabricated system prototype, we implanted the system into the guinea pig to measure the electrically evoked auditory brainstem response (EABR) activated by LCP-based cochlear implant. The Hartley guinea pig (4 week, female, 290 g) was anesthetized by an intramuscular injection of a mixture of ketamine (40 mg/kg) and xylazine (10 mg/kg). Sixteen channel cochlear electrode array was partially inserted into the left cochlea using cochleostomy. Package body and interconnection lead were inserted into the dorsal area of the experimental animal with incision from left pinna to dorsal area. The wounds were sutured after implantation of the system. Figure 2.16 shows surgical procedures for implanting LCP-based cochlear implant in the guinea pig.

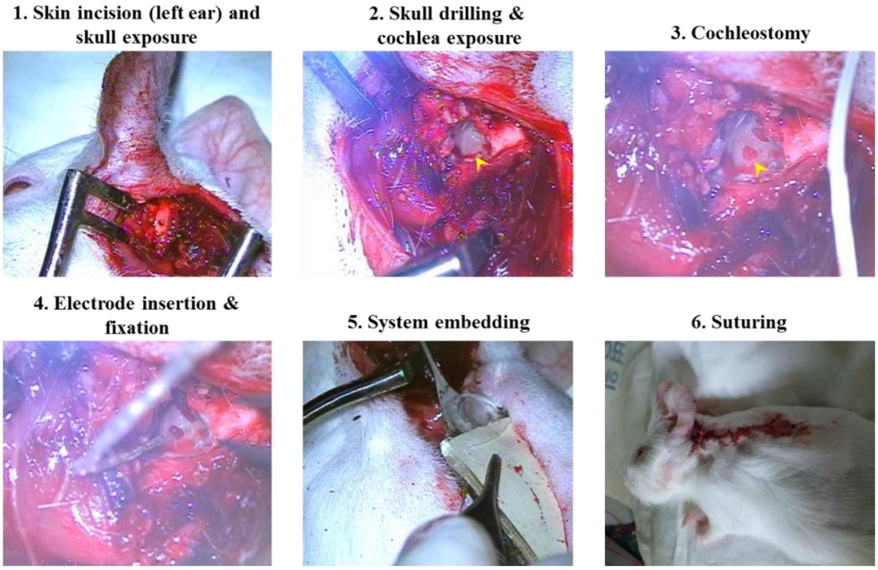

Figure 2.16 Implant surgery procedures for the LCP-based cochlear implant.

2.3.2.2 Experimental Setup and Protocol

EABRs were measured using an ABR recording system (SmartEP, Intelligent Hearing Systems, Miami, FL, USA) in a sound-proof chamber. Figure 2.17 (a) shows the system diagram for EABR recording in the guinea pig implanted with LCP-based cochlear implant. Subdermal needle recording electrodes were placed in a vertex-to-mastoid configuration (+: vertex electrode, -: left mastoid, ground: right mastoid). Eight click stimuli at 100 dB SPL were delivered to the microphone of the speech processor using a transducer of the ABR recording system (ER-2, Etymotic Research Inc., Elk Grove Village, IL, USA). The speech processor generates corresponding stimulation parameters, and data were transmitted to the implant through transcutaneous link. The implant decodes the signal and generates biphasic pulse (cathodic first, amplitude: 800 μA, duration: 32 μs/phase). The most apical site of the electrode was used as a stimulating channel with a monopolar mode. Signals collected in recording electrodes were amplified (x 100,000), and filtered (100-1,500 Hz). Figure 2.17 (b) shows the photograph of the EABR measurement setup. Animal experiments were approved by the Seoul National University Institutional Animal Care and Use Committee (SNU IACUC, Permit No. SNU-12-0379-C1A1). Experiments were performed with the helps from Prof. Seung Ha Oh at Seoul National University Hospital's Otorhinolaryngology of Department.

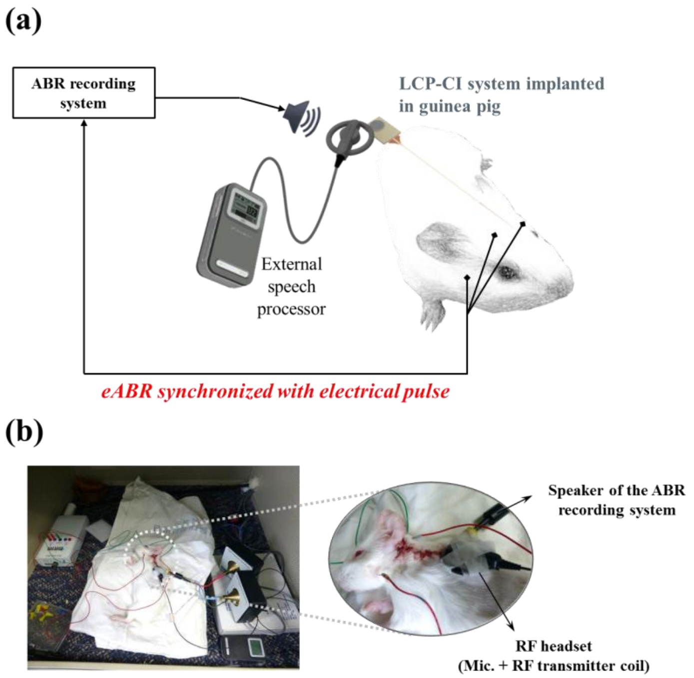

Figure 2.17 (a) System setup for EABR recording in the guinea pig implanted with LCP-based cochlear implant. (b) Photograph of the EABR measurement setup.

2.3.3 *In Vivo* Animal Study

After conducting preliminary EABR recording experiments, we found out that the experimental setup in Figure 2.17 (a) has some limitations. In preliminary study, for example, we used microphone input of the external speech processor as a trigger signal between LCP-based cochlear implant and EABR recording system. In this setup, stimulation pulse was generated when speaker of the EABR recording system is activated because experimental animal is located in the sound proof chamber. However, time lag between speaker activation and pulse generation was varied from every EABR recording trial, because stimulation rate of the channel is fixed to 1,000 pps and stimulation pulse was not precisely synchronized with the speaker. Therefore, it is difficult to achieve EABRs with a large number of averaging (e.g., 512 sweeps). Also, we measured EABRs in single stimulation condition (800 μA, 32 μs/phase). In general, EABRs were measured in multiple stimulation levels to show peak amplitude growth and then determine the threshold stimulation level. We performed new animal experiments to measure EABRs with improved experimental setup and protocol.

2.3.3.1 Animal Preparation

We used Hartley guinea pig (female, 343 g) as an animal model. Anesthesia and surgical procedures are identical to method described in section 2.3.2.1. The only difference is LCP-based cochlear electrode array is inserted into the cochlea of the animal through a round window approach instead of the cochleostomy. Two apical electrodes were inserted into the scala tympani of the cochlea. Insertion depth of the electrode array was approximately 3 mm from the round window.

2.3.3.2 Improved Experimental Setup and Protocol

Figure 2.18 presents an improved experimental setup to measure EABRs. In improved test setup, we used stimulation enable signal (EN_STIM, 0-5V) of the stimulator IC as a TTL trigger pulse between the LCP-based cochlear implant and the EABR recording system. We also used mapping software (Nuro Smart fitting v0.9) to control the LCP-based cochlear implant. In ‘Electorde Test’ mode of the mapping software, we can control the multiple stimulation parameters including stimulation mode, activation of stimulation sites, pulse amplitude and duration, and repetition number of biphasic current pulses as shown in Figure 2.19 (a). After choosing stimulation parameters, pulse trains were generated when ‘start’ button was pushed. Figure 2.19 (b) shows the generated current pulse train and EN_STIM TTL pulses. Inset of the Figure 2.19 (b) shows the enlarged view of the single biphasic and EN_STIM pulse.

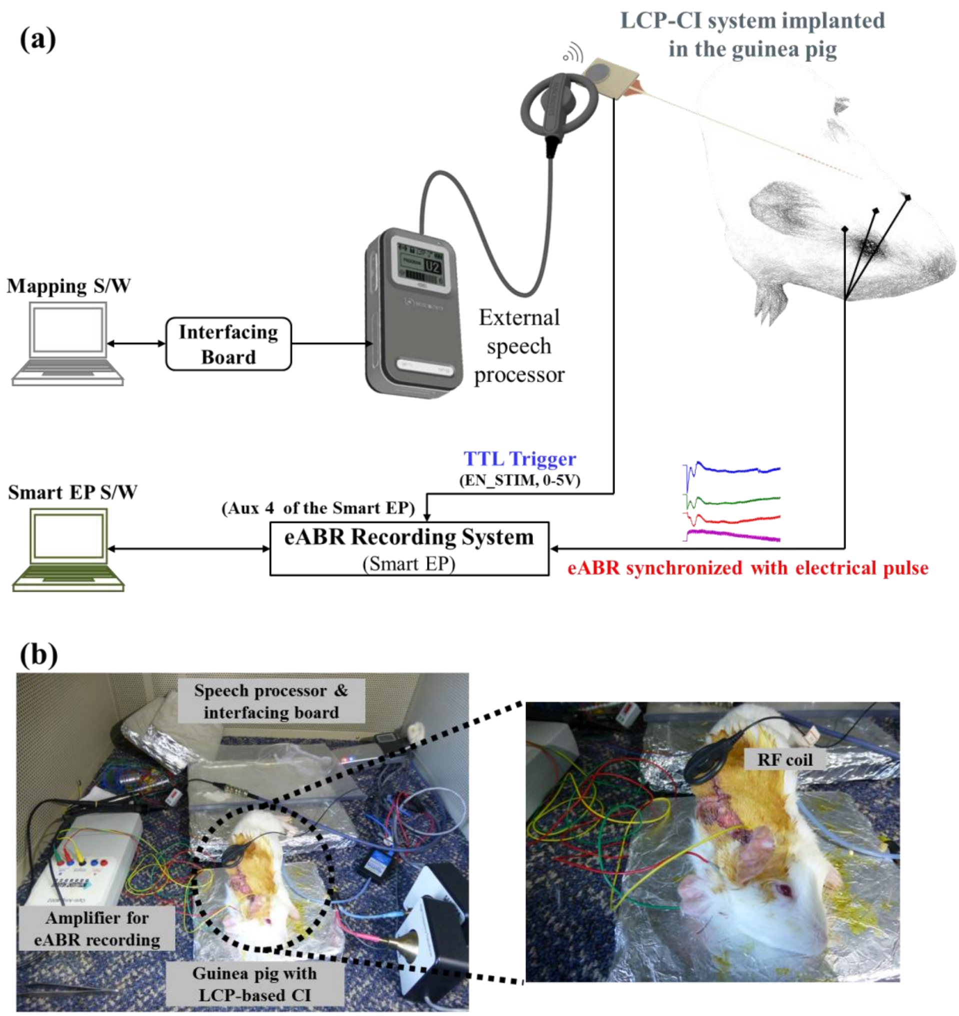

Figure 2.18 (a) Improved experimental setup to measure EABR. (b) Photograph of the improved EABR measurement setup.

(a)

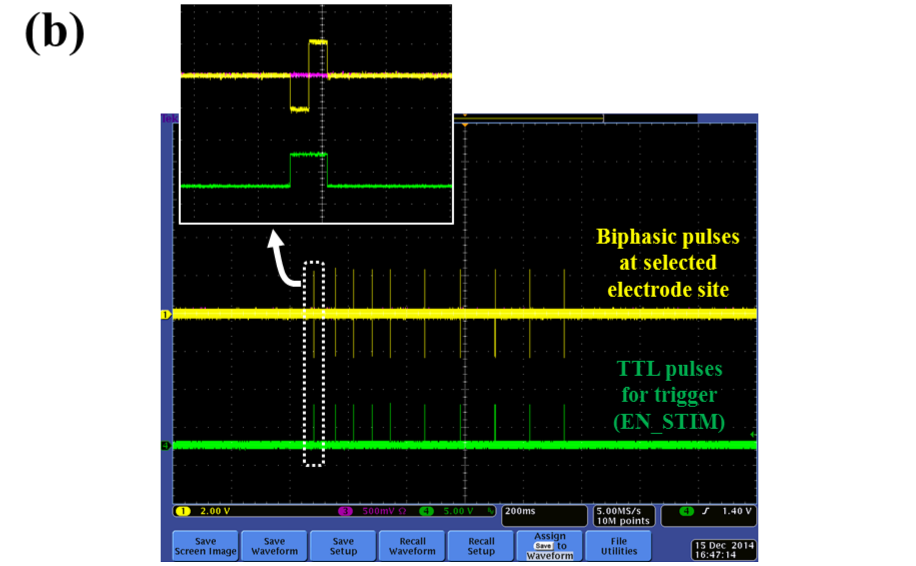

(b)

Figure 2.19 (a) ‘Electrode Test’ mode of the Mapping software to control multiple stimulation parameters. (b) Generated biphasic current pulse train and EN_STIM pulses. Inset shows the enlarged view of the single biphasic and EN_STIM pulse.

Current pulses were delivered to the cochlear electrode array implanted in the cochlea of the guinea pig, and EN_STIM pulses were delivered to the AUX 4 (Trigger-In, see Figure 2.20 (a)) port of the Universal Smart Box of the EABR recording system. In the 'eABR modality' mode of the SmartEP 4.20 software (Stimulus>Modality>eABR, see Figure 2.20 (b)), EABRs were acquired when trigger pulses were applied.

(a)

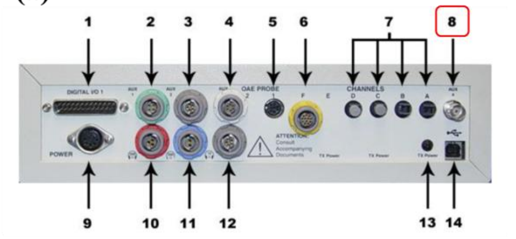

Name on Panel	Type of Connector
1. Digital I/O 1	Male DB25 Connector
2. AUX 1	4-pin Green Fischer Connector
3. AUX 2	5-pin Grey Fischer Connector
4. AUX 3	6-pin White Fischer Connector
5. OAE Probe	1/8" stereo jack or 7 Pin Din
6. Somatosensory Channel F	12-pin Yellow Fischer Connector
7. Channels A-D	Fiber Optic Receptacle
8. AUX 4 (Trigger-In)	BNC Connector
9. Power Connector	5-DIN Jack
10. 300Ω Earphones	3-pin Red Fischer Connector
11. 300Ω Bone Vibrator	2-pin Blue Fischer Connector
12. 10Ω Earphones	5-pin Grey Fischer Connector
13. TX Power	2-pin Power Jack
14. USB Port	USB-A port

(b)

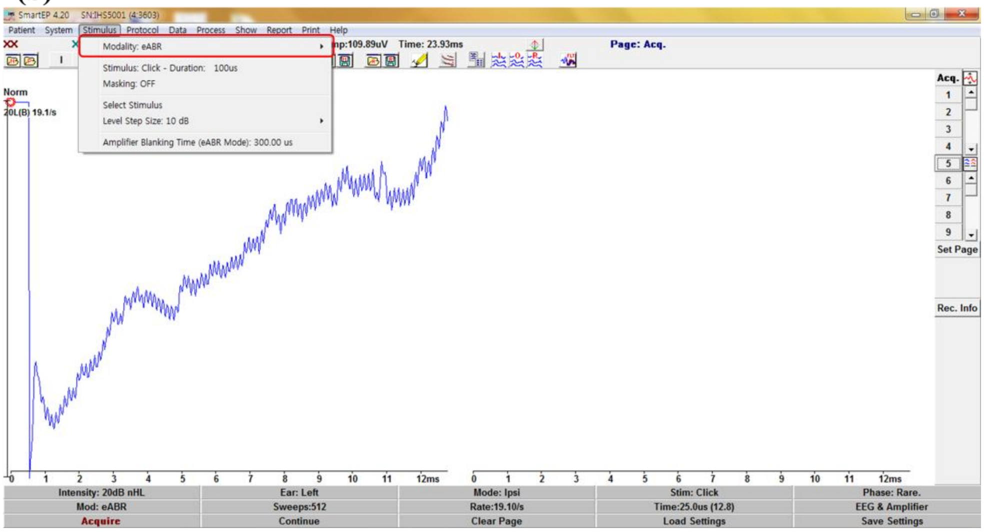

Figure 2.20 (a) AUX 4 (Trigger-In) port of the Universal Smart Box of the EABR recording system. (b) SmartEP 4.20 software setting to use external trigger for EABR recording (Stimulus>Modality>eABR).

With the improved experimental setup, we measured EABR signals in various stimulation conditions. We acquired EABRs with varying pulse amplitudes from 1,825 μA (amplitude 250) to 73 μA (amplitude 10) when pulse duration was fixed to 32 μs/phase or 48 μs/phase. Also, we measured EABRs with varying pulse durations from 24 μs (duration 3) to 56 μs (duration 7) when pulse amplitude was fixed to 1,825 μA. As a control, we performed EABR measurements before and after sacrifice when stimulation amplitude and duration are set to 1,825 μA and 48 μs, respectively. Animal sacrifice was conducted via excessive intramuscular injection of potassium chloride (KCl) solution.

The second electrode from the most apical site was used as a stimulating channel with a monopolar stimulation mode. Reference electrode was inserted into the dorsal area of the experimental animal. Also, EABRs were obtained with 512 sweeps in each stimulation condition. Gain and bandwidth of the EABR recording system was set to 100,000 and 100-3000 Hz, respectively. Also, amplifier blanking time to prevent amplifier saturation was set to 500 μs.

Animal experiments were approved by the Seoul National University Institutional Animal Care and Use Committee (SNU IACUC, Permit No. SNU-12-0379-C1A1). Experiments were performed with the helps from Prof. Seung Ha Oh at Seoul National University Hospital’s Otorhinolaryngology of Department.

2.3.4 Magnetic Resonance Imaging Compatibility Tests

2.3.4.1 Experimental Setup and Protocol

We compared the magnetic resonance image artifacts caused by a conventional titanium-based cochlear implant and a newly developed LCP-based device [53]. We adopted the SNU-Nurobiosys cochlear implant as a conventional metal-based implant sample. LCP- and metal-based devices are attached with a paper tape to the left and right side of the subject's head, respectively, to compare image artifacts simultaneously. Figure 2.21 shows the experimental setup that compares MR image artifacts using both devices. For both devices, the alignment magnet was removed for safety.

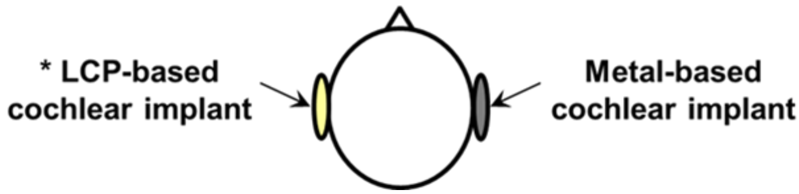

Figure 2.21 Experimental setup to compare magnetic resonance image artifacts caused by metal- and LCP-based cochlear implants.

Two MRI machines were used: a 3.0 T (Magnum, Medinus Co., Yongin, Korea) and an ultra-high 7.0 T research prototype MRI machine (Magnetom, Siemens Co., Erlangen, Germany). Currently, the 7.0 T MRI machine is not available for clinical use. Generally, signal to noise ratio of the MR images is nearly proportional to magnetic-field strength. Thus, we can observe the delicate structure of the brain using 7.0 T MRI even with multiple brainstem nuclei. We included the 7.0 T MRI machine in this study because it will become clinically available in the near future and will eventually substitute the 3.0 T MRI machine. A T1-weighted gradient echo technique (TR, 400 ms; TE, 9 ms) was used to acquire 3.0 T MR images. 7.0 T MR images were acquired using a T2*-weighted gradient echo technique (TR, 576 ms; TE, 17.8 ms). Axial and coronal plane views of the head were obtained to compare image artifacts created by the two units.

We received helps from Prof. Min Hyoung Cho at Kyung Hee University's Department of Electronics Engineering, and Prof. Zang-Hee Cho at Neuroscience Research Institute of Gachon University of Medicine and Science for using 3.0 T and 7.0 T MRI machines, respectively.

2.4 Leak-Free LCP-based Neural Electrode using Multiple Barrier Structures

In this study, we concentrated on the adhesion and reliability improvement between the top metal and the polymer insulation layer rather than polymer substrate. As shown in Figure 2.22, polymer-based electrode consists of three parts: 1) polymer substrate, 2) patterned metal layer consisting of seed layer such as titanium and upper noble metal layer which shows good biocompatibility, inertness and high charge injection capability, and 3) insulating polymer layer which has exposed window for electrode-tissue interface. In wet body environment, exposed metal site is the most vulnerable part to the permeation of body fluid, as it can undergo metal corrosion, interconnection failure, and delamination. Furthermore, site materials such as gold and platinum cannot form long-term stable carbide bonding because of their low reactive willingness with organic material contrast to the underlying seed materials such as titanium, chromium, and nickel [54]. Alternatively, we adopted surface modification strategy to enhance the reliability and adhesion force at polymer-metal interface. As shown in Figure 2.22, metallic leak-barrier structure was fabricated onto the electrode site. Leak-barriers were designed to have an anti-trapezoidal cross-sectional shape and a nanoporous surface. During the polymer insulation process, the polymer and the metal layer which has leak-barrier structures are mechanically interlocked each other to realize an increased water leakage path length as well as a mechanically strengthened metal-polymer junction.

In the following section, the apparatus of the test device, sample categorization for reliability tests, and fabrication methods to build leak-barrier structure is described. Details of reliability test will be presented in section 2.4.4.

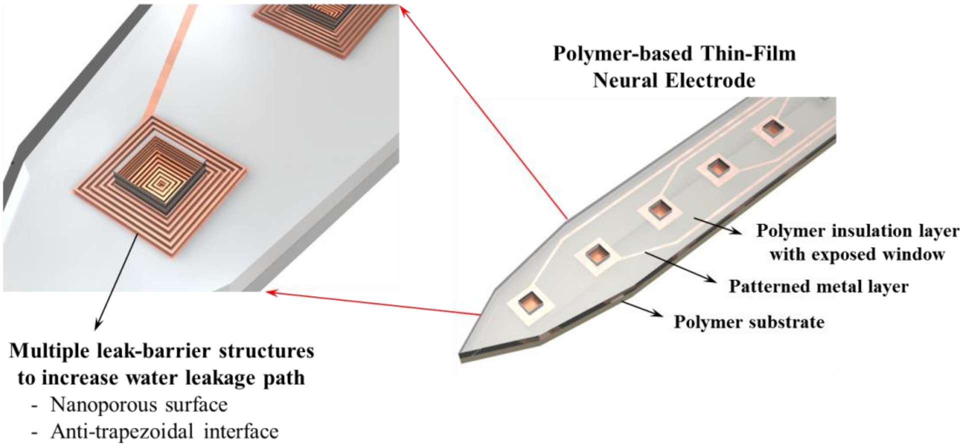

Figure 2.22 Conceptual drawing of the polymer-based thin-film neural electrode and the leak-barrier structure to increase the long-term reliability. Each leak barrier has a nanoporous surface and an anti-trapezoidal cross-section to increase water leakage path length as well as mechanical adhesion force.

2.4.1 Test Devices Design and Sample Categorization

Figure 2.23 (a) describes the apparatus of the LCP-based electrode used in this study. Overall dimensions of the electrode are 9 mm (W) x 103 mm (L). Metal patterns were deposited onto the LCP to create metal site (3 mm x 3 mm), interconnection line (700 μm width), interdigitated electrodes (IDEs) which have 80 μm width and 100 μm spacing, and contact pad. LCP insulation layer has opened window for electrode site and its dimensions are 800 μm x 800 μm. Test samples were divided into three groups according to the surface condition of the metal site: Group 1, with a smooth metal surface and without microscale barriers; Group 2, with a nanoporous metal surface and without microscale barriers, and Group 3, with a nanoporous metal surface and with microscale barriers as shown in Figure 2.23 (b).

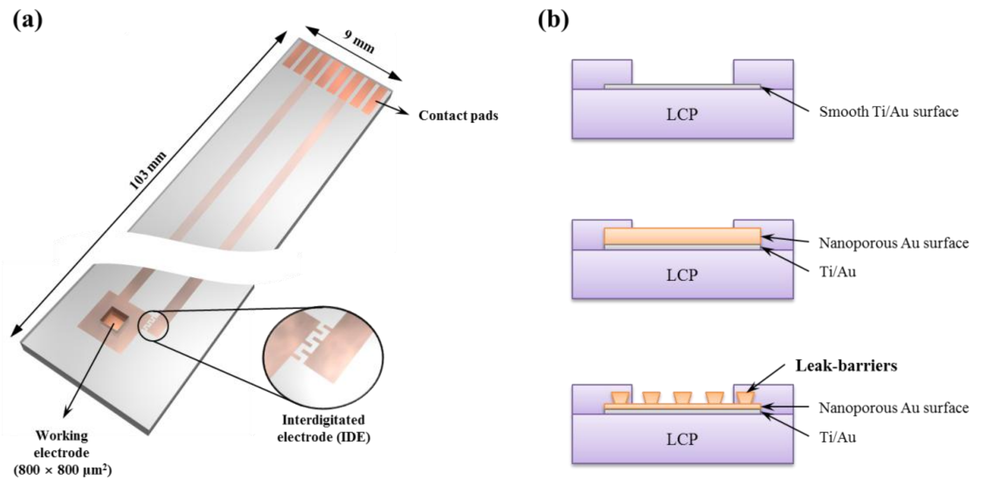

Figure 2.23 (a) Apparatus of the polymer-based electrode used to evaluate long-term reliability. Overall dimensions of the electrode are 9 mm (W) x 103 mm (L), and interdigitated electrodes (IDEs) which have 80 μm width and 100 μm spacing are integrated for leakage current measurements. Dimensions of the working electrode are 800 x 800 μm2. (b) Test group 1, 2 and 3 from the top to evaluate effectiveness of the leak-barrier structure (Group 1, with a smooth metal surface and without microscale barriers; Group 2, with a nanoporous metal surface and without microscale barriers, and Group 3, with a nanoporous metal surface and with microscale barriers).

2.4.2 Fabrication Methods

Figure 2.24 presents the fabrication processes for polymer-based electrode with leak-barrier structures (Group 3). After cleaning in methanol, acetone, and isopropyl alcohol for 1 minute each, an LCP substrate (Vecstar FA-100, Kuraray, Tokyo, Japan) is dry etched using an inductive coupled plasma (ICP) etcher for 3 minutes. Titanium and gold (Ti/Au) layers are deposited on the cleaned LCP film using an e-gun evaporator (ZZS550-2/D, Maestech Co., Ltd., Pyung Taek, Korea) at 300 nm/300 nm (Figure 2.24 (a)). Then, 10 μm thick positive photoresist (Hoechst Celanese, AZ4620, Somerville, NJ, USA) was spin-coated (Figure 2.24 (b)) and first photolithography using a mask aligner machine (MA6/BA6, SUSS MicroTec, Garching, Germany) was performed to generate metal patterns followed by first electroplating of 5 μm thick gold layer (Figure 2.24 (b) and (c)). In this step, thick photoresist with photolithography acts like an electroplating mold of the gold, and electroplated gold has rough nanoporous surface than sputtered or e-gun evaporated gold. After removal of the remaining photoresist (Figure 2.24 (d)), new positive photoresist was spin coated and then second photolithography was performed to generate mold of leak-barrier structure (Figure 2.24 (e)). During the second photolithography, intentional overexposure of light was applied to generate trapezoidal cross-sectional photoresist so that anti-trapezoidal cross-sectional leak barrier structure was fabricated using following second electroplating of 10 μm gold (Figure 2.24 (f)). Subsequently, thin Ti/Au layer was removed from the LCP substrate through wet etching process. Finally, LCP insulation layer (Vecstar FA-25, Kuraray, Tokyo, Japan) which has pre-defined site window by the laser micromachining process (Samurai UV Laser, DPSS Laser Inc., CA, USA) was laminated by thermal press machine (Model 4122, Carver, Wabash, IN, USA) in 285 °C for 20 minutes with maintaining 200 kg.

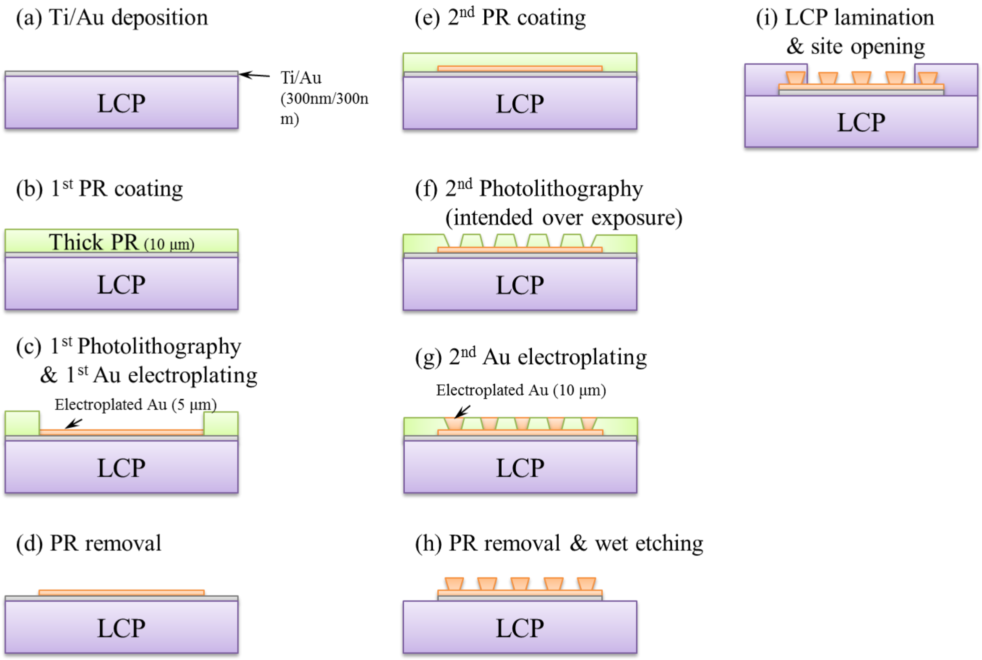

Figure 2.24 Major fabrication processes of a polymer-based electrode with leak-barrier structures.

Group 1 samples which have smooth gold surface and no leak-barrier structure were fabricated by a following procedure. Dual Ti/Au (300 nm/300 nm thick) layers were deposited on the cleaned LCP film using e-gun evaporator, and then additional Ti/Ai (500 nm/500 nm thick) layer was deposited on the LCP substrate by a sputter machine (ALPS-C03, Alpha Plus Co., Ltd., Pohang, Korea). Multilayered Ti/Au was used to protect interconnection from subsequent lamination process. Negative photoresist (Hoechst Celanese Co., AZ5214, Somerville, NJ, USA) was spin-coated on the substrate, and then photolithography was performed using a mask aligner machine (MA6/BA6; SUSS MicroTec, Garching, Germany). Subsequently, the metal patterns were created by a wet-etching process. After removing negative photoresist, LCP cover layer with laser-cut site window was laminated with metal-patterned LCP substrate. Lamination condition was identical to procedure for leak-barrier sample.

Fabrication procedures for Group 2 samples which have a nanoporous gold surface and no microscale barriers were identical to Figure 2.24 except that patterns for leak-barrier structure in Figure 2.24 (f) did not include.

2.4.3 Electrochemical Characterization of the Electrode

Electrochemical analyses including electrochemical impedance spectroscopy and cyclic voltammetry were performed to assess the condition and charge storage capacity of the fabricated electrodes. All electrochemical analyses were conducted with a potentiostat (Solartron Analytical, 1286 and 1287A, Farnborough, UK) and a 3-cell electrochemical system with a platinum counter electrode and a silver/silver chloride (Ag/AgCl) reference electrode. The electrolyte was a phosphate-buffered saline (PBS) solution (Invitrogen Life Technologies, Gibco 10010, Carlsbad, CA, USA) at pH 7.2. Electrochemical impedance spectrum was measured using a 10 mV_{rms} excitation at frequencies ranging from 0.1 Hz to 100 kHz. Cyclic voltammetry was also measured using an identical electrochemical cell. We swept the electrochemical potential from -0.6 to

0.8 V versus an Ag/AgCl electrode at a rate of 100 mV/s. Also, the cathodal charge storage capacity (CSC_C) was determined from the obtained cyclic voltammogram. Electrochemical impedance spectra and cyclic voltammograms were analyzed according to the three groups of test samples.

The scanning electron microscopy (SEM) was also used to scan the junction between LCP insulation layer and leak-barrier structure.

2.4.4 Long-Term Reliability Test of the Leak-Free LCP-based Neural Electrode

To evaluate the efficacy of the leak-barrier structure, we performed accelerated lifetime soak tests. First, we performed highly accelerated test in 110 ℃ condition. Although the elevated temperature for accelerated aging of polymers is generally recommended to be at or below 60 ℃ [55], 110 ℃ was chosen in the preliminary accelerated lifetime test because it was aimed to expedite the encapsulation failure within the limited period of experiment and to compare the “relative” reliability depending on the surface conditioning and leak-barriers. Figure 2.25 (a) shows the setup for highly accelerated soak test in 110 ℃ condition. Devices under test are immersed into the PBS which mimics salted body fluid, and PBS filled bottle was placed in 110 ℃ convection oven. Deionized water is continuously supply through water tank with flow regulator (DOSI-FLOW 10, Leventon, Spain) to maintain the water level. In order to simulate electrical stress, biphasic current pulses with stimulation parameters of 1 mA amplitude, 32 μs duration/phase, and 1 kHz pulses per second were continuously applied to the electrode site relative to the extra reference electrode (platinum rod) through a custom-made multichannel current stimulator (see Figure 2.26).

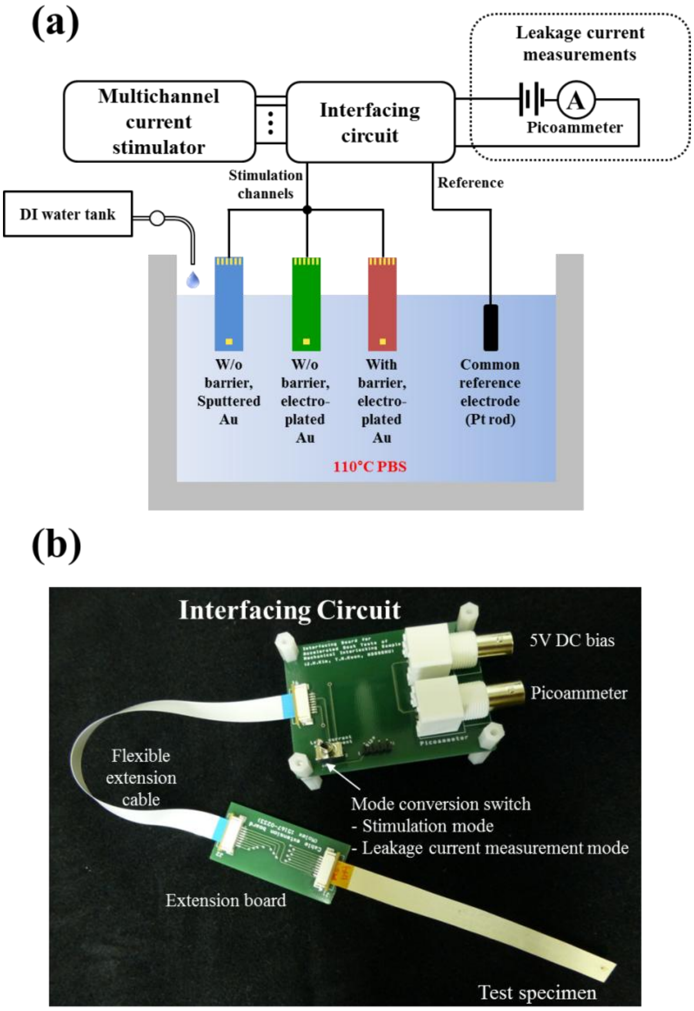

Figure 2.25 (a) Accelerated soak test setup. All samples are immersed in the phosphate buffered saline (PBS) at elevated temperatures. Deionized water is continuously supplied to the bath to sustain water levels. During soaking, biphasic current pulses are continuously applied to the electrode site (stimulation parameters: 1 mA in pulse amplitude, 32 μs duration/phase, and 1 kHz pulse rate). Leakage current between interdigitated electrodes are periodically measured using a picoammeter with 5 V dc bias. (b) Interfacing circuit for accelerated soak test.

(a)

(b)

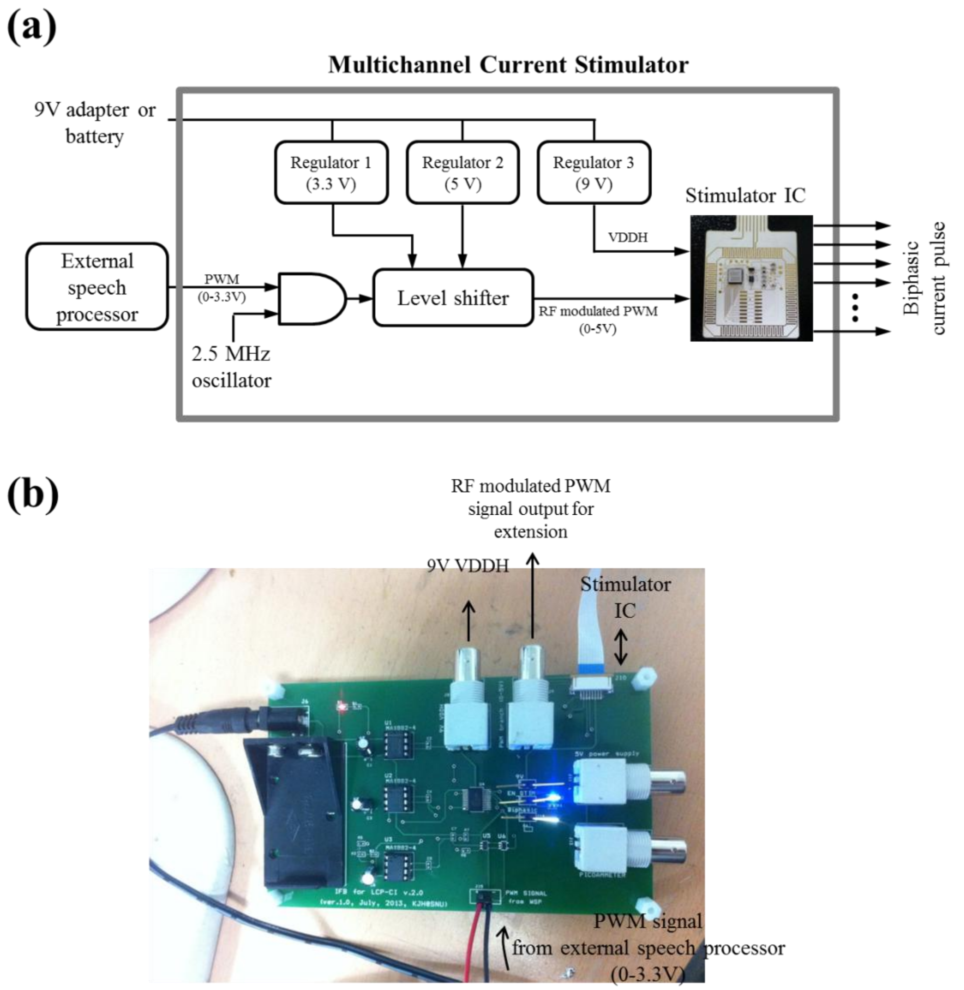

Figure 2.26 (a) Brief circuit diagram of the custom-made multichannel current stimulator for current pulsing during accelerated soak test. (b) Apparatus of the fabricated multichannel current stimulator.

One sample per test group was used as device under test (Group 1, with smooth metal surface and without leak-barrier; Group 2, with a nanoporous metal surface and without microscale barriers, and Group 3, with a nanoporous metal surface and with microscale barriers). Using IDE pairs integrated into the electrodes, leakage currents are periodically measured using a picoammeter (Model 6485, Keithley Instruments, Inc., Cleveland, OH, USA) with 5 volts DC bias. Custom-made interfacing board provides switching between stimulation mode and leakage current measurement mode (Figure 2.25 (b)). Picoammeter is controlled by custom-made LabView software as illustrated in Figure 2.27 (National Instruments, Austin, TX, USA) using GPIB controller (GPIB-USB-HS, National Instruments, Austin, TX, USA). Leakage currents are measured 100 times and then average and standard deviation of the 100 leakage current values are calculated and plotted. Failure criterion for electrode samples is set to the 0.6 μA which is roughly three orders higher than initial leakage current.

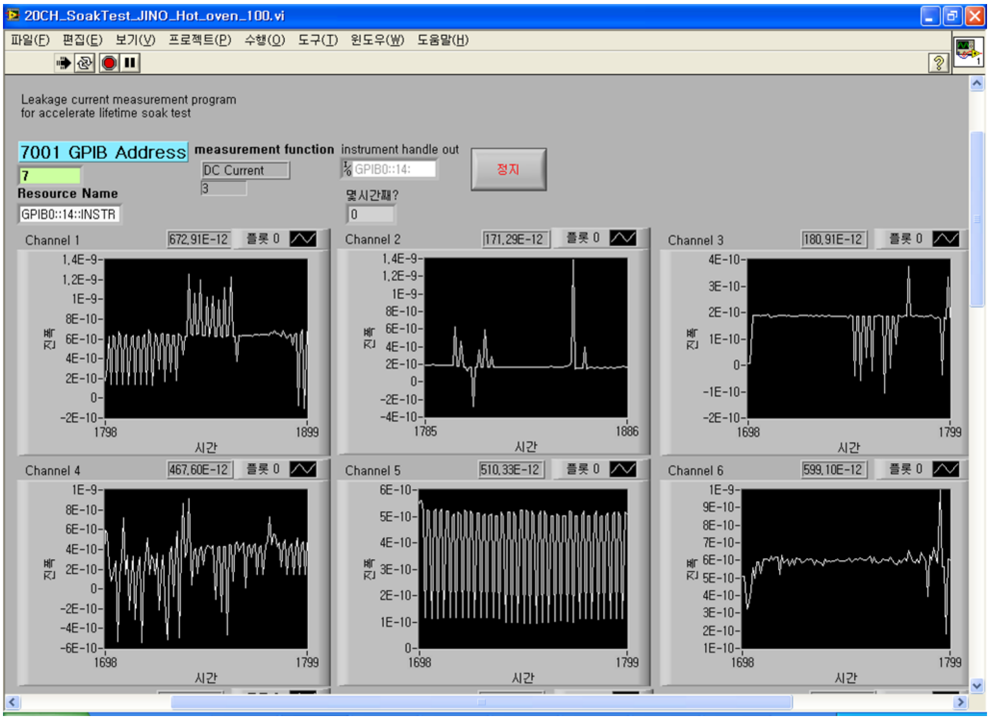

Figure 2.27 Custom-made LabView program for leakage current measurements.

Formal accelerated soak tests were also performed in 75 ℃ and 95 ℃ after identifying the relative reliability between samples through highly accelerated thermal stress condition. If we know the mean time to failure (MTTF) of the samples in more than two temperatures, lifetime at body temperature (37 ℃) can be estimated using following Arrhenius equation [56].

$$\mathrm{AF} = \frac{\mathrm{Rate}\ (T_2)}{\mathrm{Rate}\ (T_1)} = \frac{\mathrm{MTTF}\ (T_1)}{\mathrm{MTTF}\ (T_2)} = exp\left[\frac{E_a}{R}\left(\frac{1}{T_1} - \frac{1}{T_2}\right)\right]$$

where, E_a is the activation energy, T_1 is the use temperature in Kelvin (K=℃+273), T_2 is the elevated, accelerated-test temperature ($T_2>T_1$), and R is the Boltzmann's constant (8.617 x 10^{-5} eV/K). Acceleration factor (AF) was defined as the ratio of the degradation or failure time at the use temperature T_1 relative to that an elevated, accelerated-test temperature T_2 [56]. In Arrhenius model, it is assumed that the mechanism of damage does not change in the process.

Identical soak test setup as illustrated in Figure 2.25 (a) is used for two temperature accelerated soak tests. Group 1 (smooth gold surface, no leak-barrier) was rule out in the two temperature accelerated soak test because they have lacked reliability. Four samples per group (Group 2 and 3) are used as test specimens.

2.5 Manufacturing Cost Analysis

2.5.1 Overview of the Cost Structure

In this section, we look into brief overview of the fundamentals of product cost structure to analyze the manufacturing cost of titanium- and LCP-based cochlear implant. Figure 2.28 shows the basic components of cost and ratio of each factor relative to the sales price. Manufacturing cost is the sum of costs of all resources consumed in the process of making a product [57]. The manufacturing cost can be categorized as direct manufacturing cost and indirect manufacturing cost. Direct manufacturing cost is directly attributable to the production of specific object, and includes direct material cost, direct labor cost, and direct expenses. By adding indirect manufacturing cost which is not directly accountable to a cost object, the manufacturing cost can be obtained. Examples of costs that are included in the indirect manufacturing cost category are depreciation on equipment used in the production process, property taxes on the production facility, rent on the factory building, salaries of maintenance personnel and managers and so on. The total cost can be obtained by adding the sales cost (such an advertisement expenses and sales persons' payment) and general administration cost and research and development cost to the manufacturing cost. Sales price is determined by adding proper profits to the total cost. Ratio of profits relative to sales price is different from manufacturing area to area. According to Korea Health Industry Development Institute's report in 2014, operating profit of 15 global medical device companies such as Medtronic and Johnson & Johnson is about 16.8 % on average in 2013.

Also, ratio of manufacturing cost is approximately 25-30 % of sales price.

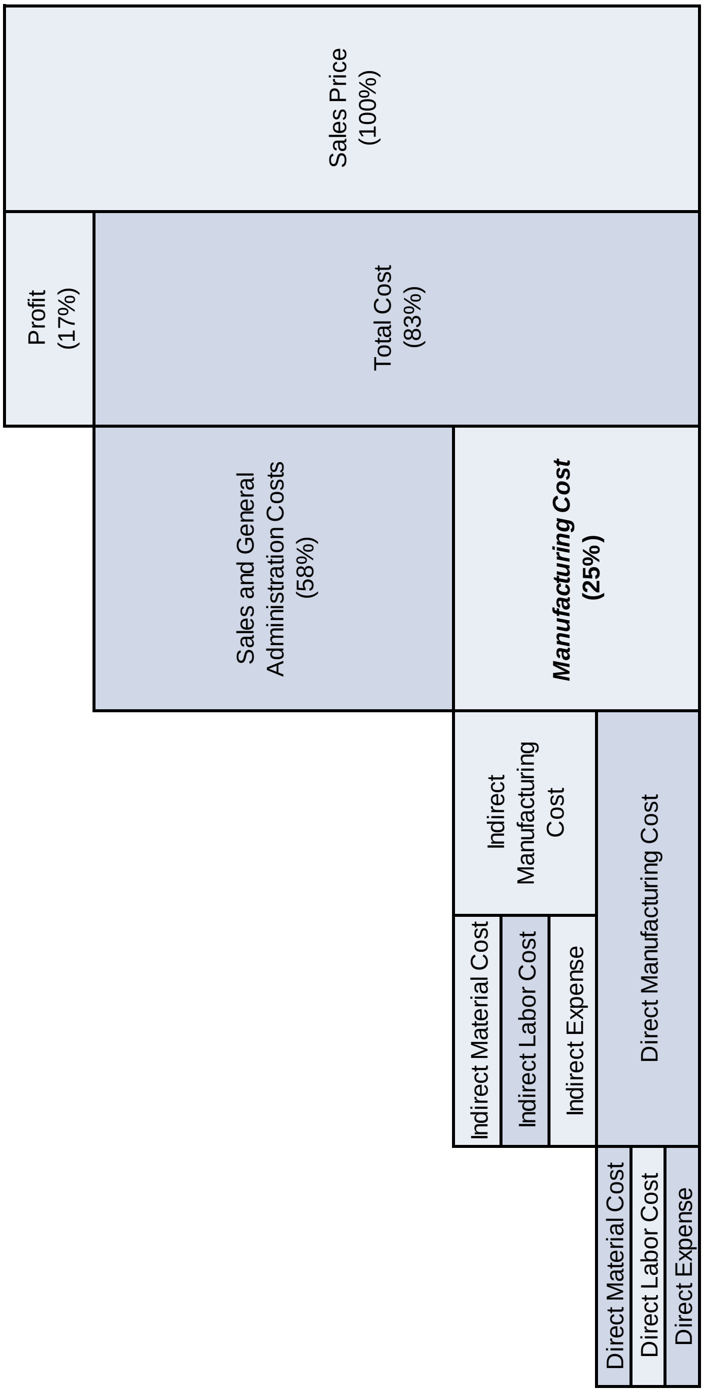

Figure 2.28 Cost structure.

2.5.2 Comparative Analysis of the Manufacturing Cost Analysis of the LCP- and Titanium-Based Cochlear Implants

As mentioned earlier, our group had been developed titanium-based cochlear implant (Nuvoc-A01) through academia-industrial collaboration project, and it was approved by Korean FDA in October, 2010. The developed device has similar composition and materials to conventional cochlear implants produced by big three cochlear implant manufacturers. Based on this device, we analyze the manufacturing cost of the titanium-based cochlear implant. Investigated manufacturing cost of the titanium-based device is compared with those of newly developed LCP-based cochlear implant.

The ‘direct manufacturing cost’ of the device is classified into four parts: Part 1. Electrode Array, Part 2. Electronics, Part 3. Package and Magnet, and Part 4. Coil. Each part is divided into detailed sub-part, and cost of each part is investigated considering yield. We investigate the ‘direct materials cost’ and ‘direct expense’ to produce one hundred devices. ‘Direct labor costs’ to produce one hundred devices were also calculated in each part. In this procedure, we assumed that daily wage for the production worker is 100 $, and jobs of all workers to be maintained during the period of device production. For calculating ‘indirect manufacturing cost (or manufacturing overhead)’, depreciation of the production facilities was only considered. Costs for facilities to produce titanium- and LCP-based device are investigated first of all. After that, we assumed that the period of depreciation of all facilities is 10 years, and then calculate the depreciation costs during the period of manufacturing one hundred devices using straight-line depreciation method that is depreciation is charged uniformly over the life of an asset. Sum of direct manufacturing costs (including direct material costs, direct labor costs, and direct expenses) to produce one hundred devices, and indirect manufacturing costs (the depreciation costs during the period of manufacturing one hundred devices) are defined as total manufacturing cost to produce one hundred units of cochlear implant, and then we finally calculate the manufacturing cost per unit.

Chapter III

Results

3.1 Fabricated System

3.1.1 External Speech Processor

Figure 3.1 (a) shows the apparatus of the developed external speech processor (SNU-NB processor) based on traditional approach. The device is a body worn type, and operated by 3.75 V Li-ion (1,800 mAh) rechargeable battery. Also, it has many functions controlled by LCD-button user interface to provide the degree of freedom for patients' comfort. The size of the device is 89 x 49.2 x 22 mm^3, and weighs 100 g. The power consumption of the DSP and its peripheral circuit is about 375 mW. Also, RF transmitter coil including Class-E power amplifier consumes 67.5 mW. Figure 3.1 (b) shows the PWM data and amplitude modulated signal which is modulated with 2.5 MHz carrier in Class-E amplifier.

(a) **(b)**

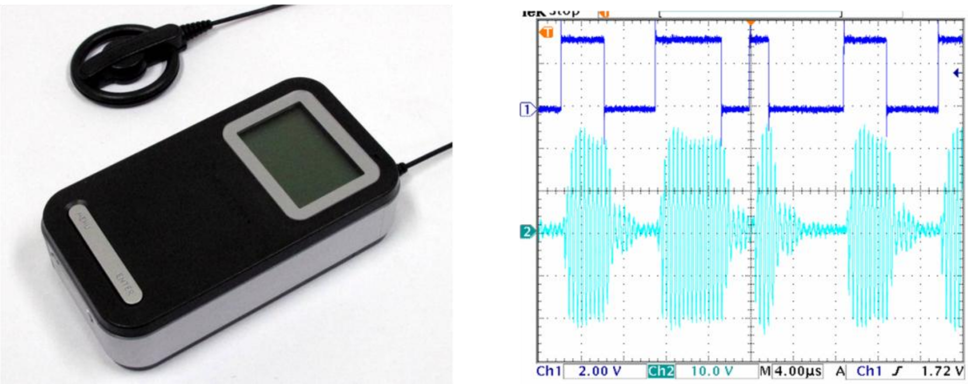

Figure 3.1 (a) Developed external speech processor (SNU-NB processor) based on traditional approach.

3.1.2 LCP-based Cochlear Implant

3.1.2.1 Packaging Process

Figure 3.2 (a) shows the first version of the LCP-based electronics. White arrow indicates the chip protection guard structure which is made from 1 mm thick high temp LCP. Figure 3.2 (b) shows the LCP encapsulated device using first packaging method. Several wrinkles are generated around the device, because there was height difference between guard and multiple LCP cover layers. We immersed the device in 75℃ PBS to quickly identify the possibility of water ingression through the wrinkles while operating the device using an external speech processor. Figure 3.2 (c) shows the harvested sample of the device after 15 days of soaking. LCP packaging layers were carefully removed to observe traces of water ingression. As a result, water was penetrated into the wrinkle area (dashed area) as shown in Figure 3.2 (c). Interconnection metal lines are corroded due to shortage between metal traces by permeated water.

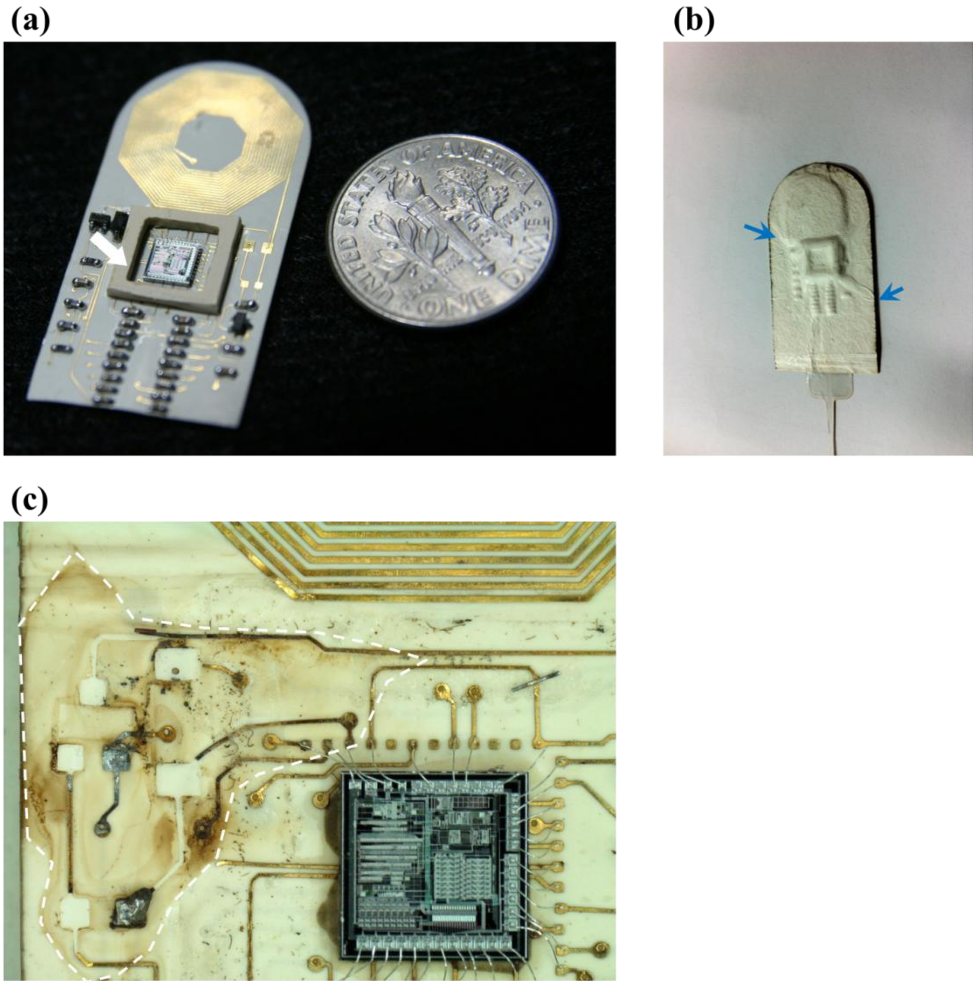

Figure 3.2 (a) First version of the LCP-based cochlear electronics. (b) LCP encapsulated electronics using first packaging method. (c) Harvested sample after 15 days of soaking in 75 ℃ PBS. Packaged LCP layers were removed to observe the water permeation path. Dashed area shows the traces of water penetration.

Figure 3.3 (a) shows the second version of the LCP-based electronics. In contrast with Figure 3.2 (a), planar coil was stacked using multilayered structure for miniaturization. With the second version electronics, we applied second packaging method. In the second packaging method, board outline was locally pressed by custom-made press jig to suppress the generation of wrinkles in board outline area, and identical chip protection guard was applied. As shown in Figure 3.3 (b), amount of large wrinkle is greatly reduced, but still exist small size wrinkles. After immersing the device in 75℃ PBS during the 9 days, we observed the device functionality, and result shows that electronics have broken down by water ingression. Aforementioned two results indicate that suppression of wrinkle is important in LCP electronics packaging. Therefore, we modified the package stack-up to suppress the wrinkles completely. Wrinkles are generated by uneven package stack-up. Due to the chip protection guard and a few discrete components, LCP cover layers are not flat during thermal lamination process.

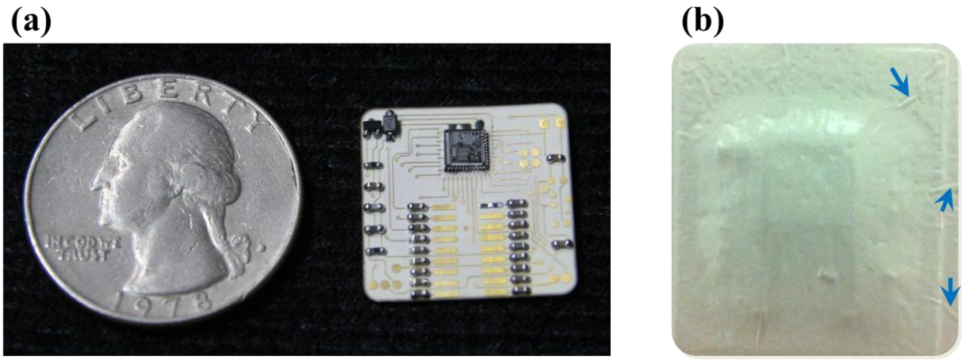

Figure 3.3 (a) Second version of the LCP-based cochlear electronics. (b) LCP encapsulated electronics using the second packaging method. Blue arrows indicate the small size wrinkles.

Instead of chip protection guard, we use multilayers of laser cut LCP films to create recessed cavity for electronics in third packaging method. All electronics including stimulator IC and discrete components are placed inside the recessed cavity, and height of multilayered LCP films is larger than maximum height of the electronic components. Thus, package stack-up can be flat during thermal lamination procedure, and does not generated wrinkles because LCP multilayers are only pressed. Also, Teflon films are used to produce entirely flat package stack-up including LCP-based cochlear electrodes.

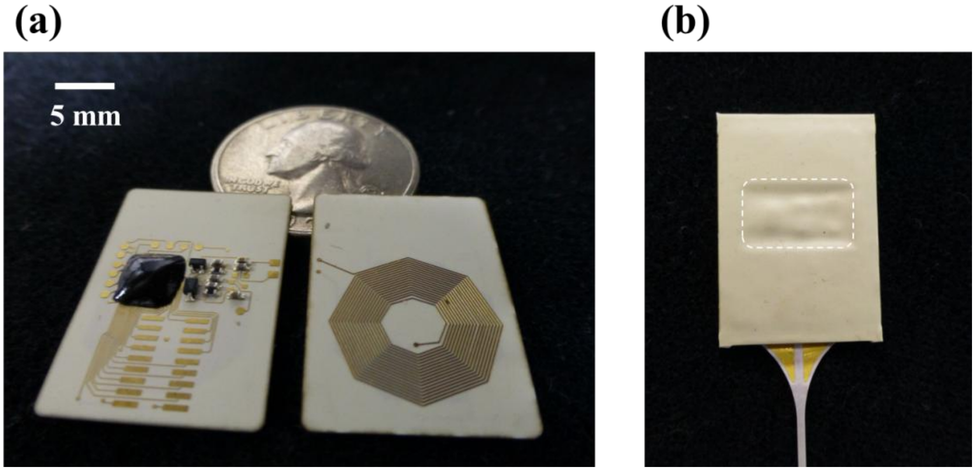

Figure 3.4 (a) Third version of the LCP-based cochlear electronics. (b) LCP encapsulated electronics using the third packaging method. No observable wrinkles were generated in the package. Dashed box indicates recessed cavity before LCP packaging.

3.1.2.2 Fabricated LCP-based Cochlear Implant

Figure 3.5 shows the fabricated LCP- and titanium-based cochlear implant. Developed LCP-based implant is more compact than conventional titanium-based device. The dimensions of the LCP-based device are only 20 mm (W) x 28 mm (L) x 1.2 mm (H). The area and thickness of the LCP-based device are reduced by approximately 70 % compared with the titanium-based device. Besides, LCP-based device weighs less than 1 g. Thus, LCP-based device is less invasive than the titanium-based implant because it needs extremely small incision and requires shallow or no mastoid drilling for the implantation surgery. Detailed information of the LCP- and titanium-based implant is summarized in Table 3.1.

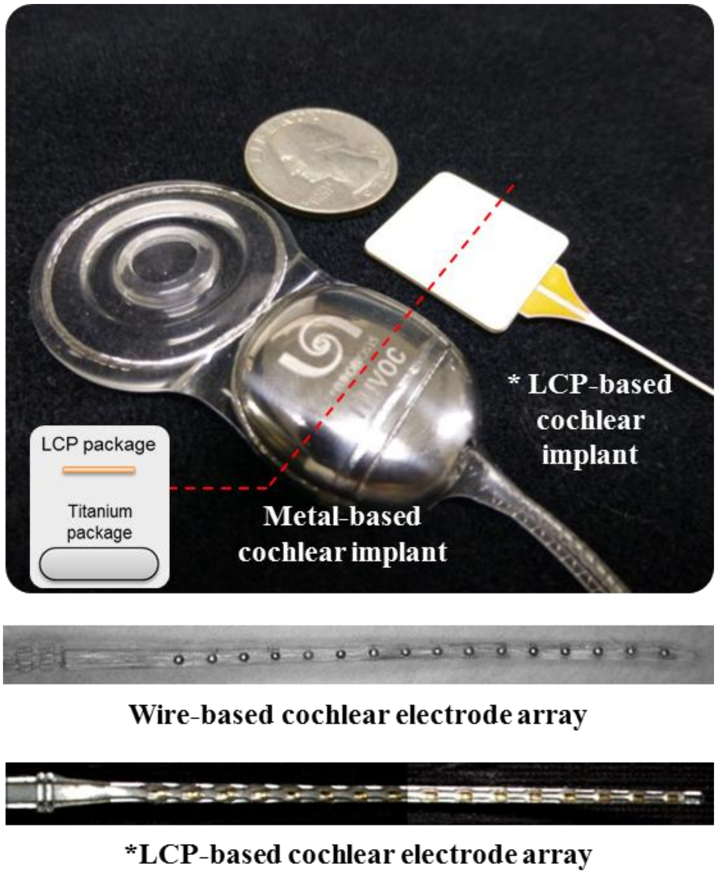

Figure 3.5 Developed *LCP- and conventional titanium-based cochlear implant systems for size comparison. Inset of the top panel shows the cross-sectional dimensions of two devices. Bottom two panels show conventional wire- and LCP-based cochlear electrode arrays [51].

Table 3.1 Size comparison table of the LCP- and titanium-based cochlear implants.

	Liquid Crystal Polymer-Based Cochlear Implant	***Conventional Titanium-Based Cochlear Implant***
Package Dimensions	20 x 28 mm^2	65.7 x 33.3 mm^2
Package Max. Thickness	(without magnet) 1.2 mm	(without magnet) 8.2 mm
	(with magnet) 3.7 mm	(with magnet) 8.2 mm
Weight	(without magnet) 0.45 g	(without magnet) 10.4 g
	(with magnet) 2.75 g	(with magnet) 12.7 g

3.1.2.3 Bench-Top Test of the LCP-Based Cochlear Implant

Figure 3.6 shows the bench-top test result of the fabricated LCP-based cochlear implant system. Figure 3.6 (a) shows the test setup to measure biphasic pulse with 1 kΩ resistive load connected between stimulation electrode and reference electrode. Amplitude and duration of the stimulation current pulse are set to 1.8 mA and 24 μs, respectively, and then applied to the implantable unit. Voltage excursion in air was measured. Measured voltage is about 1.8 V (1.8 mA x 1 kΩ).

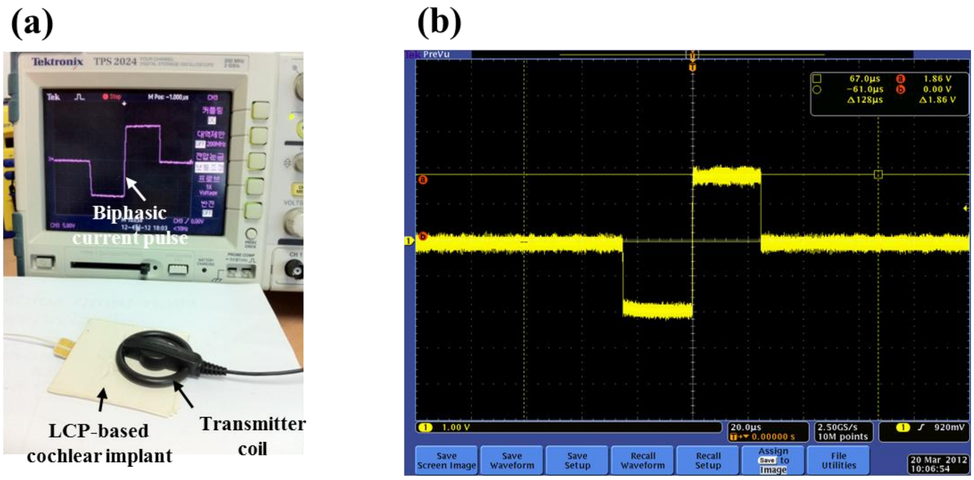

Figure 3.6 (a) Bench-top test setup of the LCP-based cochlear implant. (b) Measured biphasic pulse with 1 kΩ resistive load in air. Amplitude and duration of the stimulation current pulse are set to 1.8 mA and 24 μs, respectively.

Figure 3.7 shows voltage transients in response to biphasic current pulses with varying pulse amplitude and duration in PBS. Figure 3.7 (a) illustrates voltage transients in response to current pulses of fixed duration and varying amplitude from 219 μA (30 current level) to 1.752 mA (240 current level). In contrast to Figure 3.6 (b), sharp voltage transients were measured due to capacitance of the PBS. Peak amplitudes of the voltage transients are linearly increased without saturation. It means that electronics are successfully operated and electrode site has sufficient charge injection capabilities without corrosive reaction. Figure 3.7 (b) shows the voltage transients in response to current pulses of fixed amplitude and varying duration from from 8 μs (duration 1) to 56 μs (duration 7). Pulse durations of measured voltage excursions are also linearly increased.

(a)

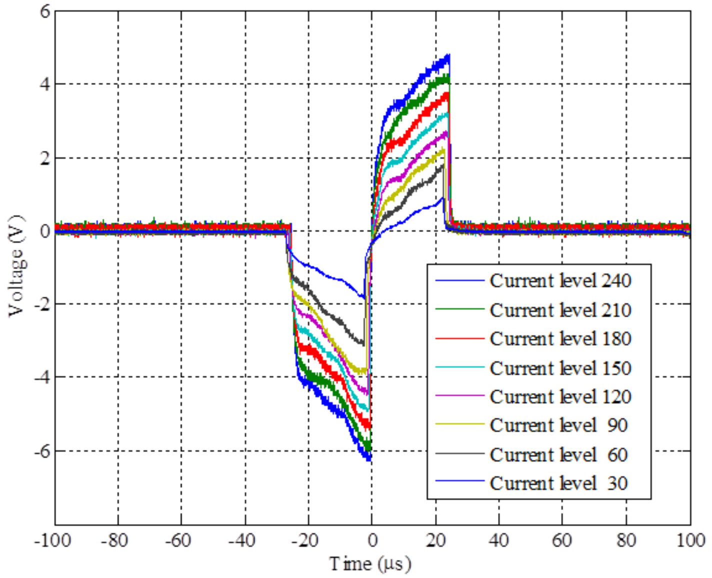

(b)

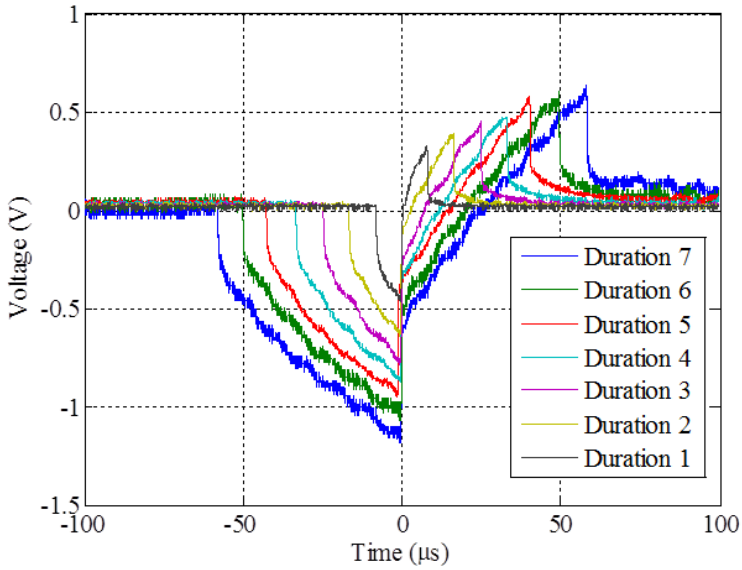

Figure 3.7 (a) Voltage transients in response to the pulse amplitude variation in PBS. (b) Voltage transients in response to the pulse duration variation in PBS.

3.2 *In Vivo* Animal Study

Figure 3.8 (a) shows the X-ray image of the guinea pig implanted with the LCP-based cochlear implant. Right arrow indicates electronics module with alignment magnet encased by titanium housing, and left arrow points out LCP-based electrode array and interconnection leadwire. Inset shows the enlarged view of the implanted LCP-based cochlear electrode array and interconnection lead. To the third electrode from the electrode tip was inserted into the scala tympani of the guinea pig cochlea. The result of preliminary EABR measurement test of the LCP-based device is presented in Figure 3.8 (b). The most apical electrode site (channel 1) is used as a stimulation channel. Stimulus artifact caused by cathodic first biphasic current pulse is presented in 0~3 ms, and followed by wave V of the EABR in about 4 ms. It means that the developed LCP-based cochlear implant system successfully deliver the stimulation pulse to the spiral ganglion cells of the experimental animal through designated electrode site.

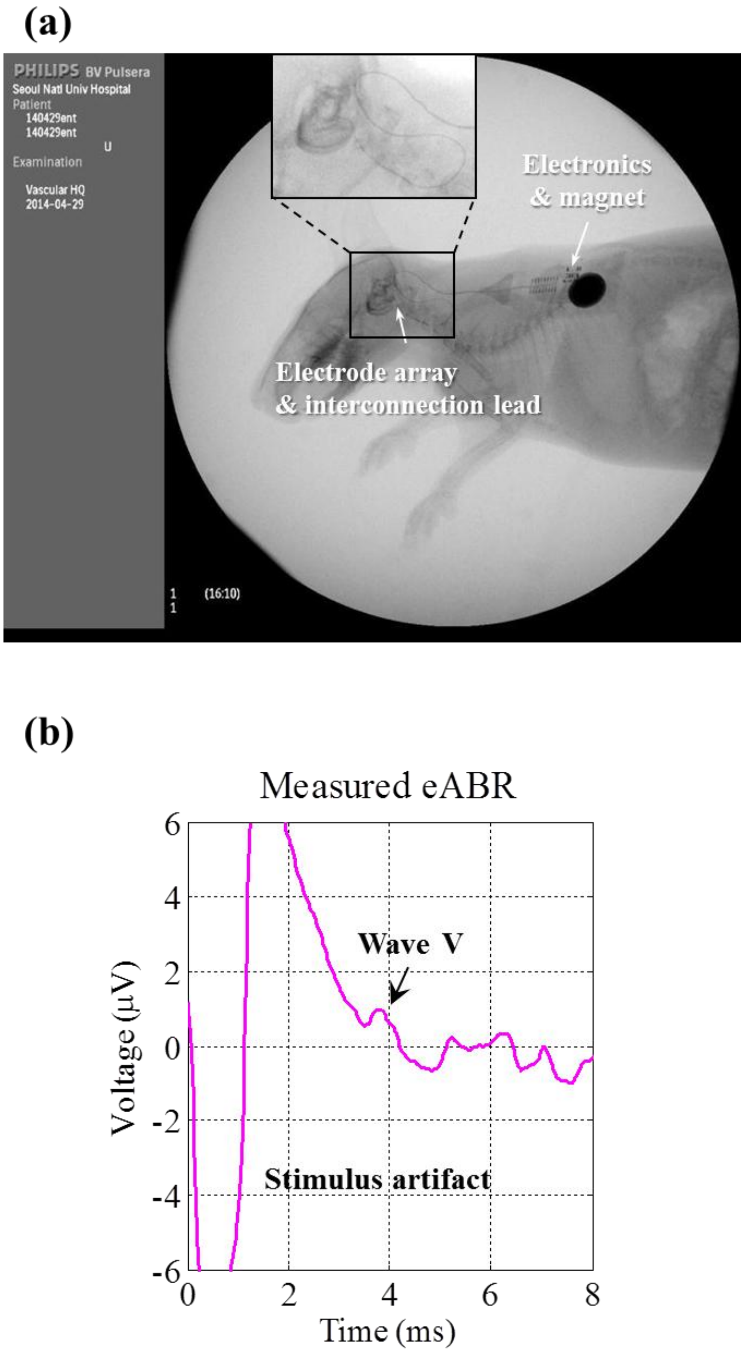

Figure 3.8 (a) X-ray image after cochlear implantation to the guinea pig. Inset indicates the enlarged view of the electrode array and interconnection lead. (b) Measured EABR waveform when applying 800 μA, 32 μs biphasic pulse. Stimulus artifact was presented in 0-3 ms, and followed by wave V of the EABR in 4 ms.

Figure 3.9 (a) and (b) show measured EABRs according to varying stimulation amplitude when pulse duration is fixed to 32 μs/phase and 48 μs/phase, respectively. The improved experimental setup described in section 2.3.3.2 was used to acquire EABRs. In Figure 3.9 (a), distinct positive peak was presented in the latency of 1.8 ms, when stimulation level is 1,825 μA. Amplitude of the positive peak in 1.8 ms was gradually decreased as stimulation level was reduced. When stimulation level is 365 μA, no positive peak is presented. Similar tendency was observed in Figure 3.9 (b). In the latency of 1 ms and 2 ms, clear positive peaks were presented when stimulation level is 1,825 μA. Positive peak in 1 ms was disappeared in lower stimulation level. However, peaks in 2 ms were clearly presented in the stimulation level from 1,533 μA to 365 μA. When stimulation level is lower than 365 μA, no peak was presented.

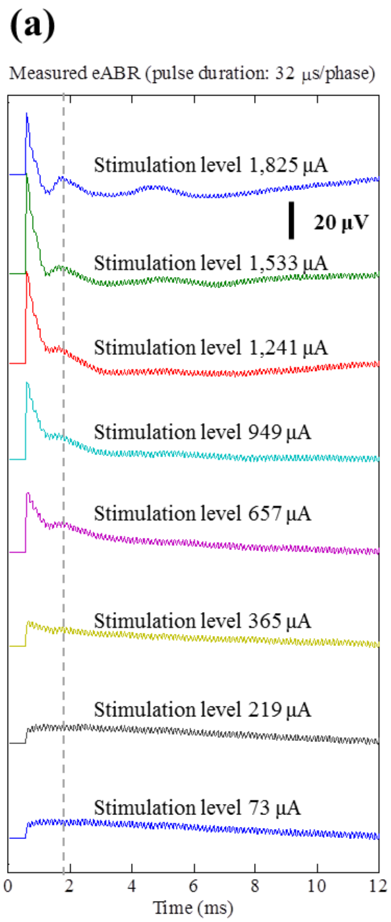

Figure 3.9 Measured EABRs according to varying stimulation amplitude from 1,825 μA to 73 μA when stimulation duration was fixed to (a) 32 μs/phase and (b) 48 μs/phase.

Figure 3.10 (a) shows the EABRs according to varying stimulation duration when pulse amplitude is fixed to 1,825 μA. Distinct peaks were presented in all conditions except for duration 3. Figure 3.10 (b) shows the EABRs before and after animal scarification. All test setup was maintained without changes, and the only variation was the animal was alive or not. Stimulation amplitude and duration were set to 1,825 μA and 48 μs/phase, respectively. In the latency of 1 ms and 2 ms, distinct positive peaks were presented when the animal was alive (top trace in Figure 3.10 (b)). In contrast, no peak was observed when the animal was sacrificed (bottom trace in Figure 3.10 (b)). It shows that meaningful EABR signals were acquired through implanted LCP-based cochlear implant system.

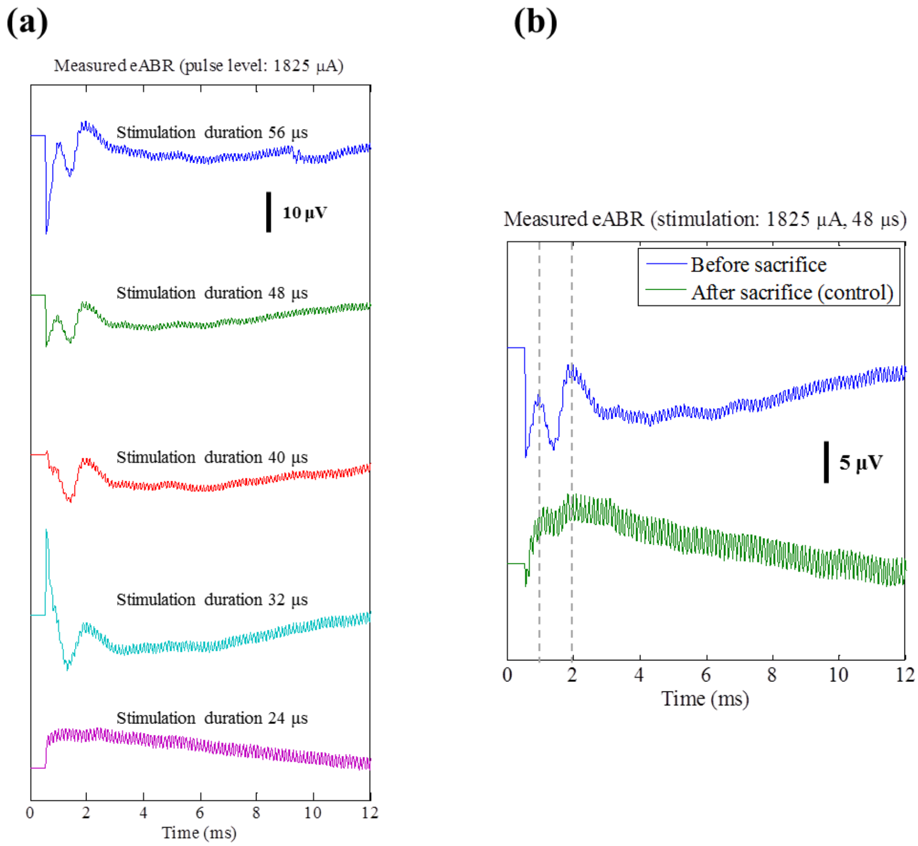

Figure 3.10 (a) Measured EABRs according to varying stimulation duration from 56 μs/phase to 24 μs/phase when stimulation amplitude was fixed to 1,825 μA. (b) Measured EABRs before and after scarification of the experimental animal. Stimulation amplitude and duration was set to 1,825 μA and 48 μs/phase, respectively.

3.3 Magnetic Resonance Imaging Compatibility

Figure 3.11 shows T1-weighted 3.0 T MR images of the head with the metal-based implant attached to the left side of the head and the LCP-based implanted on the opposite side. Figure 3.11 (a) and (b) are the axial and coronal images of the head, respectively. In Figure 3.11 (a), brain imaging of the right side is obscured by artifacts. The diameter of the artifact caused by the metal-based cochlear implant was approximately 69 mm. Contrary to the metal implant, very mild artifacts were generated by the LCP-based device on the left side. A similar tendency was observed in the coronal image of the head (Figure 3.11 (b)). There exist extremely small artifacts on the left side, while severe image distortion was generated on the right side by platinum coil and titanium packages. Therefore, if we use a functional MRI to see the neuronal activity from the auditory brain cortex of the metal-based cochlear implant recipients, it will be impossible to monitor the ipsilateral temporal lobe that was applied to the primary auditory cortex. It should also be noted that the distorted area of the MRI images can be smaller compared to the images of the cochlear implant recipients, since the metal- and LCP-based cochlear implants were attached to the outside of the skin, and not fully implanted inside the skin.

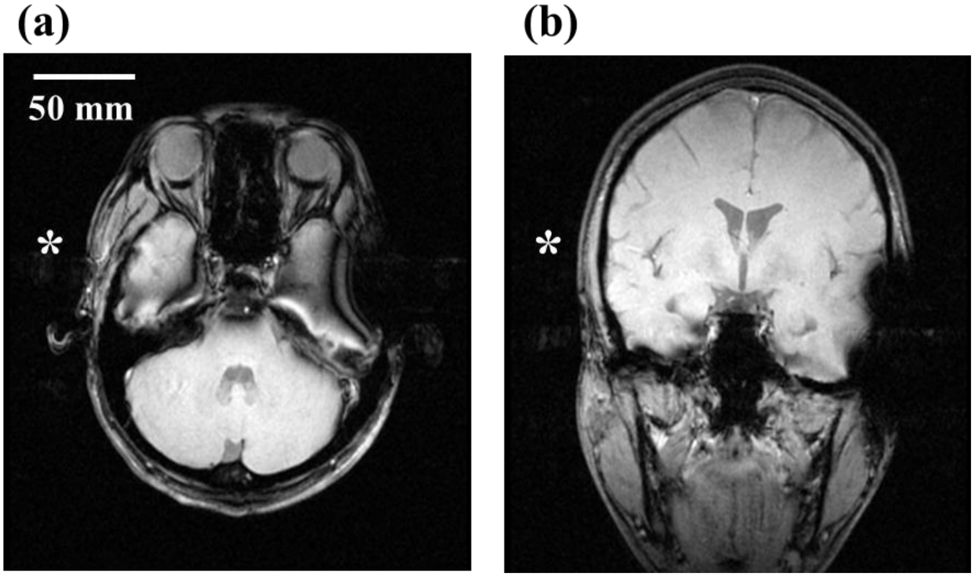

Figure 3.11 T1-weighted 3.0 T magnetic resonance images of the head: axial (a) and coronal (b) plane views when the LCP- and metal-based cochlear implants are attached to the left and right side of the head, respectively. Asterisk indicates the side of the LCP-based device.

Figure 3.12 (a) and (b) are the T2*-weighted 7.0 T MR images of the axial and coronal plane of the head, respectively. Since the spatial resolution is higher than the 3.0 T images, sulcus, gyrus, white matter, and gray matter are clearly distinguished. An identical device configuration was used to compare the artifact between the two implants. Similar to the 3.0 T images, severe artifacts created by a metal-based implant were observed on the right side of the metal packaged cochlear implant, while mild artifacts were observed on the left side. In 7.0 T images, a magnitude of the artifacts caused by LCP-based implant was slightly larger than 3.0 T images. It is likely that the LCP-based planar coil is more interactive with the RF coil of the 7.0 T MRI machine than the 3.0 T MRI.

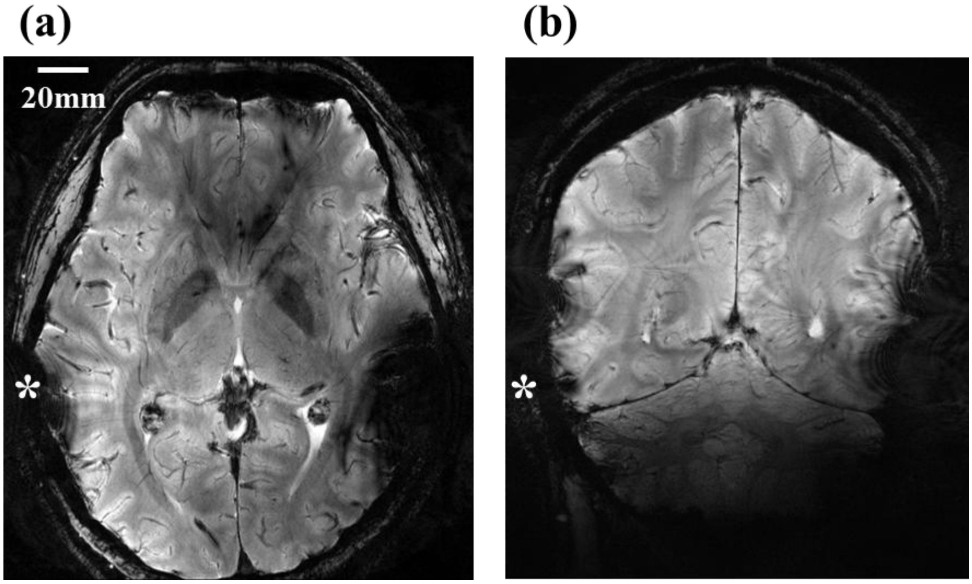

Figure 3.12 T2*-weighted ultra-high 7.0 T magnetic resonance images of the head: axial (a) and coronal (b) plane views when the LCP- and metal-based cochlear implants are attached to the left and right side of the head, respectively. Asterisk indicates the side of the LCP-based device.

3.4 Leak-Free LCP-Based Neural Electrode using Multiple Barrier Structures

3.4.1 Fabricated Electrode

Figure 3.13 shows the fabricated three groups of LCP-based neural electrode before insulation process. (Group 1 sample has smooth metal surface and no leak-barrier (Figure 3.13 (a). Group 2 sample has a nanoporous metal surface and no leak-barrier (Figure 3.13 (b). Group 3 sample has a nanoporous metal surface and leak-barriers (Figure 3.13 (c).) Micrographs of IDEs (80 μm width, 100 μm spacing) for leakage current measurements and bottom-right corner of the metal site are shown in top and bottom panels, respectively.

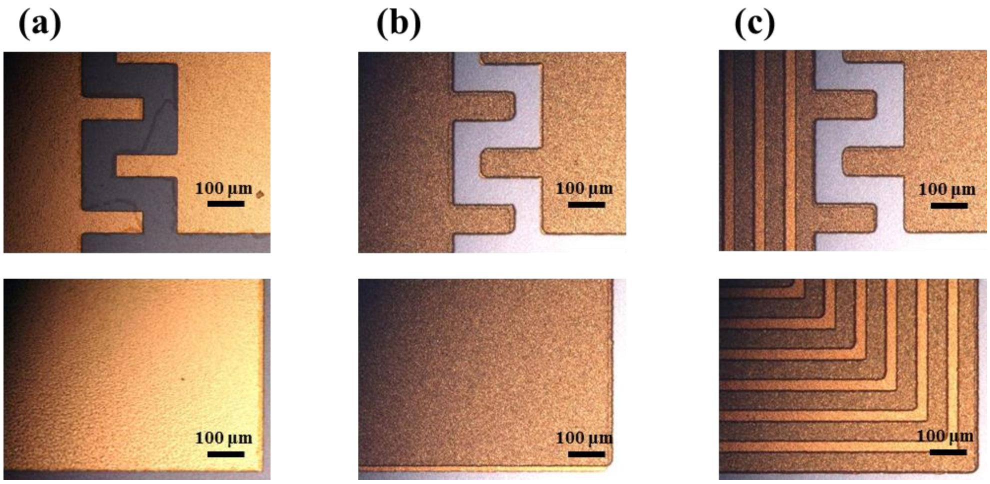

Figure 3.13 Micrographs of IDEs (top panels) and bottom-right corner of metal sites (bottom panels) before insulation process. (a) Group 1, (b) Group 2, (c) Group 3.

Fabricated samples in Figure 3.13 are encapsulated with 25 μm thick low temp LCP films. After packaging process, we observed the cross-section of leak-barrier sample (Group 3) using SEM. Figure 3.14 (a) shows the top view of the metal electrode site. Dimensions of the exposed electrode site are 800 μm x 800 μm. Figure 3.14 (b) shows the cross-sectional image of the leak-barrier sample. It shows that LCP substrate and insulation layers are seamlessly bonded each other. Figure 3.14 (c) shows the cross-sectional image of A-A' in Figure 3.14 (a). Each metallic leak-barrier has anti-trapezoidal interface for enhanced mechanical adhesion. Figure 3.14 (d) is image of the high magnification of dashed box of the Figure 3.14 (c). LCP insulation layer was tightly bonded to the leak-barrier structure without any voids.

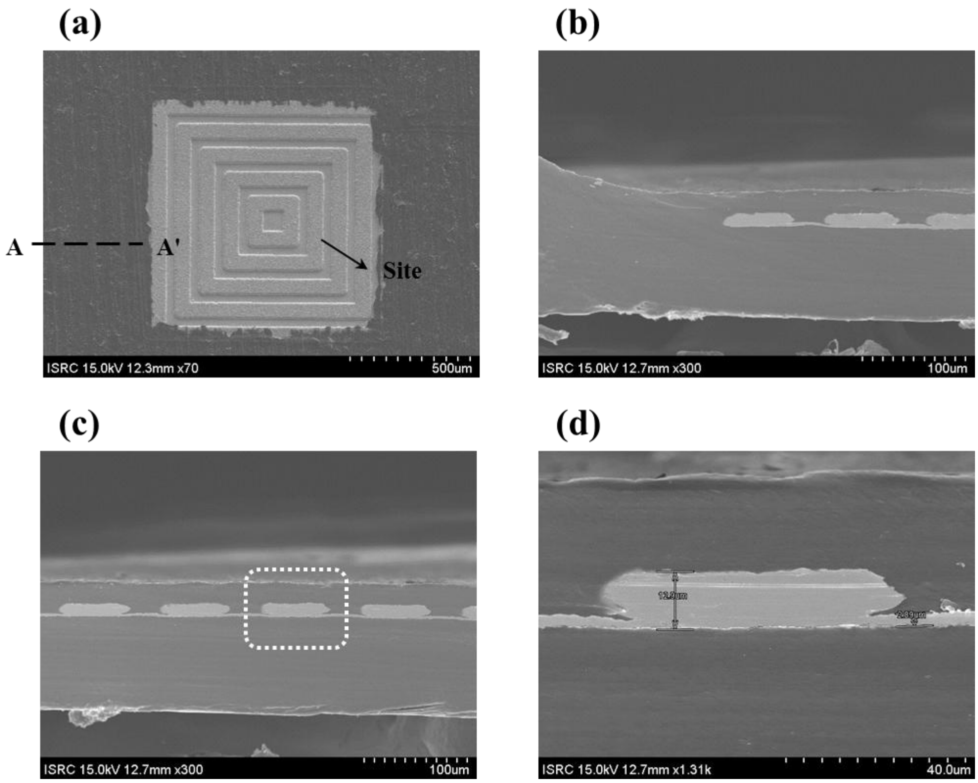

Figure 3.14 SEM images of the LCP-based electrode with leak-barrier structures after packaging (Group 3). (a) Top view of the electrode site. Dimensions of the electrode site are 800 x 800 μm^2 (b) Cross-sectional image of the leak-barrier sample. LCP substrate and insulation layer are seamlessly bonded each other. (c) Cross-sectional image (A-A') of the leak-barrier sample. Each leak-barrier has anti-trapezoidal interface for improved mechanical adhesion. (d) High magnification of dashed box of the (c). LCP insulation layer was tightly bonded to the leak-barrier without voids.

3.4.2 Characterization of the Electrode

We performed an impedance spectroscopy and a cyclic voltammetry to verify electrochemical properties of the fabricated electrodes. Figure 3.15 (a) shows the representative result of electrochemical impedance spectroscopy in three groups of electrodes. Impedances at 1 kHz were measured as 375.6 Ω, 559.6 Ω, 375.1 Ω in Group 1, 2, and 3, respectively. Also, Figure 3.15 (b) illustrates the cyclic voltammogram of three groups of electrodes. Cathodal charge storage capacities were measured as 164 $\mu C\ cm^{-2}$, 129 $\mu C\ cm^{-2}$, 279 $\mu C\ cm^{-2}$, in Group 1, 2, and 3, respectively.

(a)

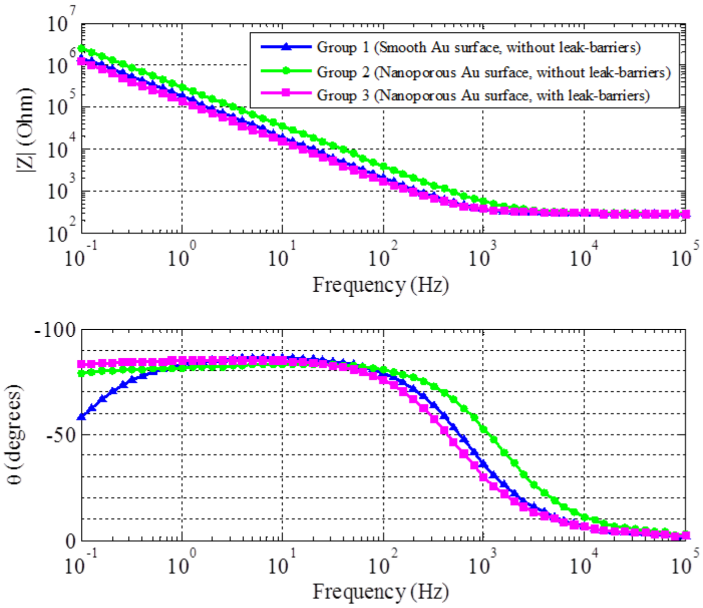

(b)

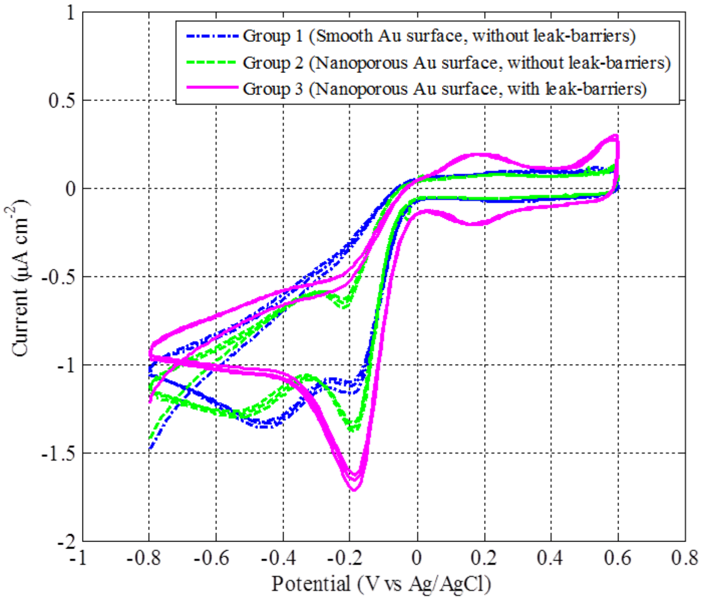

Figure 3.15 Result of the electrochemical analysis. (a) Electrochemical impedance spectroscopy and (b) cyclic voltammogram of the fabricated polymer-based electrode in three test groups.

3.4.3 Long-Term Reliability

Highly accelerated soak test in 110℃ PBS was performed to quickly verify the reliability of the LCP-based electrode which has the microscale barriers and a nanoporous surface. Figure 3.16 shows the leakage current curves of three test groups according to soaking days. Group 1 which has no leak-barriers and smooth gold surface was failed first within 26 days of soaking. Group 2 which has no microscale barriers and a nanoporous gold surface was failed secondly within 37 days of soaking. Group 3 which has microscale barriers and a nanoporous gold surface was failed lastly. If we simply apply the rule of 10 (Q10) as following equation which means for every 10 ℃, life will double,

$$\text{Acceleration factor} = 2^{\Delta T/10}$$

$$\text{where}, \Delta T = T - T_{ref}$$

$$T\text{: elevated temperature}$$

$$T_{ref}\text{: reference temperature (37℃)}$$

estimated lifetimes of three groups are about 11.23 years, 15.97 years, and 20.29 years, respectively. Leak-barrier sample (Group 3) shows roughly two times longer lifetime than Group 1 (no leak-barrier, smooth gold surface).

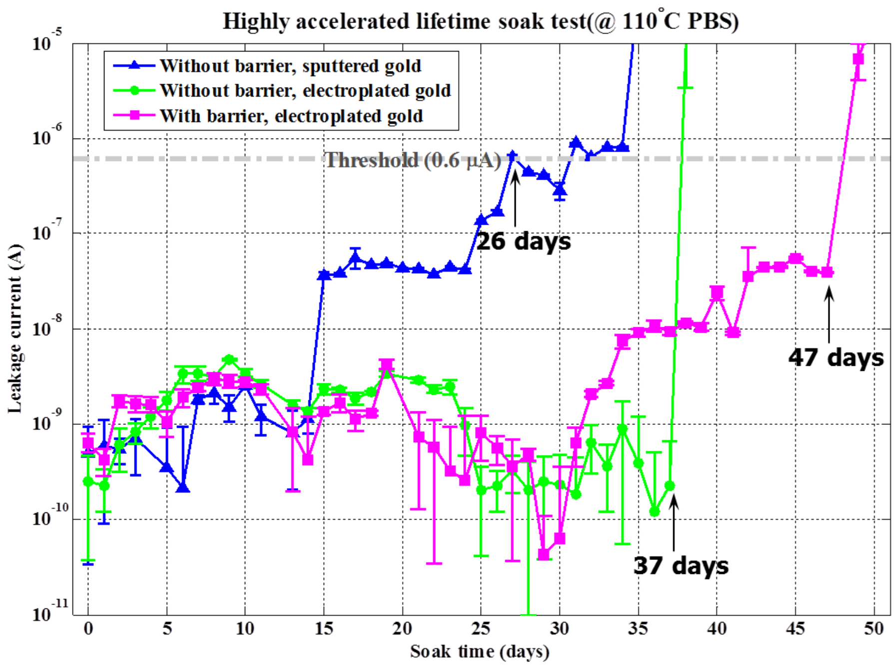

Figure 3.16 Result of the highly accelerated soak test in 110 ℃ PBS. Blue line with triangle marker indicates Group 1 sample. Green line with circle marker presents the leakage current curve of the Group 2 sample. Red line with square marker is the result of the Group 3 sample.

Harvested samples from the highly accelerated soak test are visually inspected with optical microscope and SEM. Figure 3.17 shows the microscopy images of three groups. Electrode site area of each group is presented in left panels, and IDE area is presented in right panels. In Group 1 and 2 samples, LCP cover layer was removed to observe the IDE in detail. In Group 3 sample, it is impossible to remove LCP cover layer because there’s no significant delamination between LCP cover and metal layer. Therefore, we observed IDE area using transmitted illumination mode of the microscope.

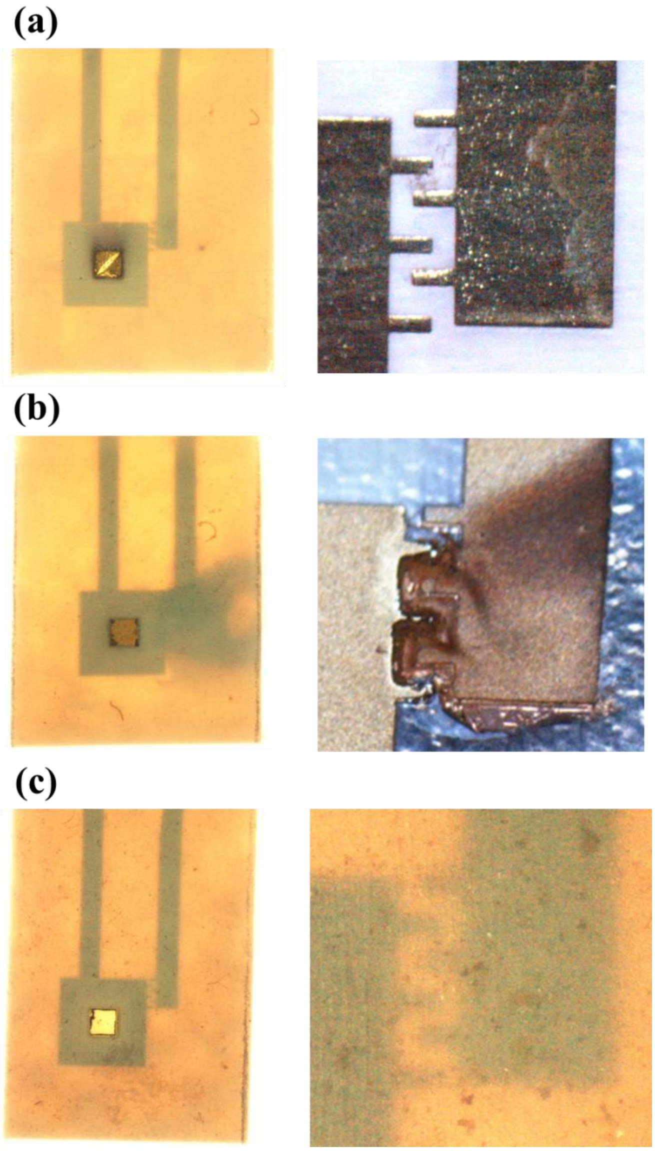

Figure 3.17 Microscopy images of harvested samples after 110 ℃ highly accelerated soak test. (a), (b) and (c) show the electrode site area (left panels) and IDE part (right panels) of Group 1, 2, and 3, respectively. In right panels of (a) and (b), LCP cover layer was removed. In right panel of (c), LCP cover layer was not removed due to high level of adhesion between LCP cover and metal layer with leak-barrier structure.

After visual inspection using optical microscope, we performed SEM imaging and image analysis to observe the delaminated condition of electrodes. Figure 3.18 (a) and (b) show the cross-sectional SEM images (B-B') of the Group 1 and cross-sectional SEM image (B-B') of the Group 2 sample, respectively. Figure 3.18 (c) shows the consecutive cross-sectional SEM images (C-C') of the Group 3 sample. In Figure 3.18 (a) and (b), delamination between LCP cover and metal layer was clearly observed. In contrast, no severe delamination was observed in Figure 3.18 (c). Also, leak-barriers are still interlocked with the LCP cover layer.

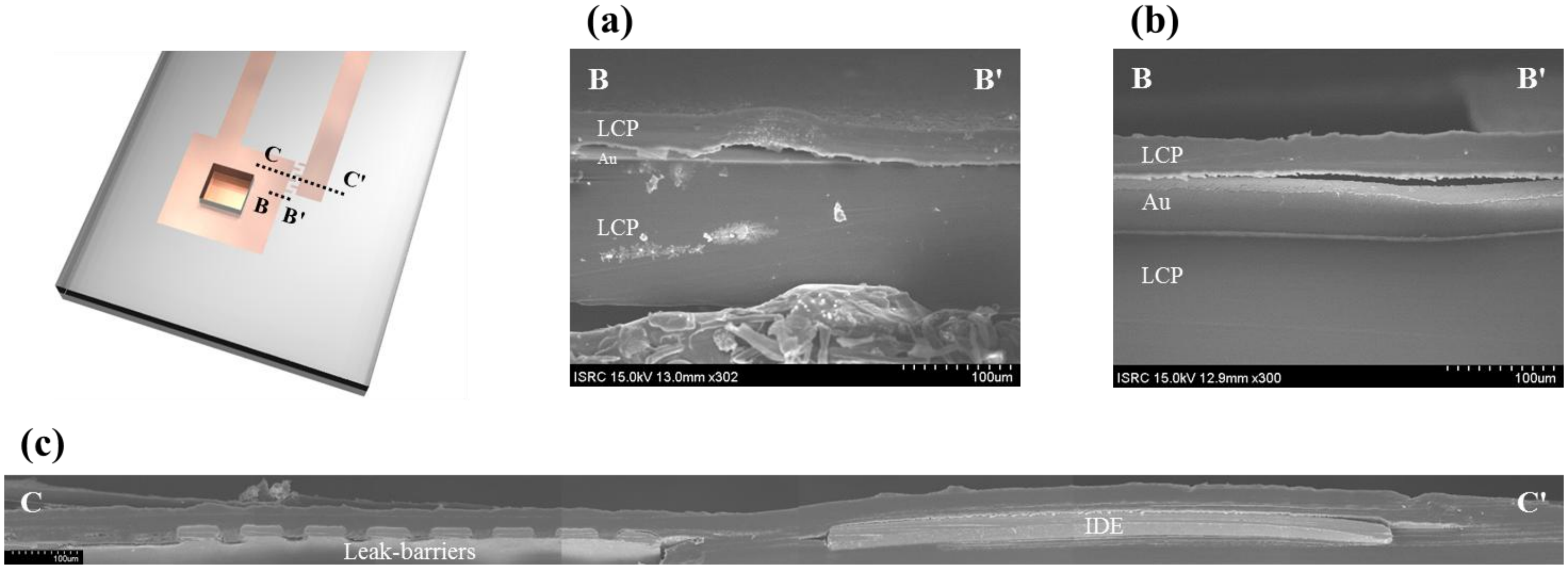

Figure 3.18 SEM images of test samples harvested after soaking in 110℃ PBS. (a) Cross-sectional image (B-B') of the Group 1 sample, (b) Cross-sectional image (B-B') of the Group 2 sample, (c) Consecutive cross-sectional image (C-C') of the Group 3 sample. In (a) and (b), delamination between LCP cover and metal layer was clearly observed. In contrast, no visible delamination was observed in (c).

Figure 3.19 (a) and (b) show ongoing results of the accelerated soak test in 95 ℃ and 75 ℃ PBS. All samples in Group 2 and 3 maintain constant leakage currents at the time of writing at least. Although estimating the aging factor for polymers at above 60 ℃ based on the Q10 is no accurate, a quick estimation is that 178 days at 95 ℃ is equivalent to 9,917 days (27 years) in 37 ℃ with an acceleration factor of about 56. It is relatively longer than estimated lifetime from the highly accelerated soak test in 110 ℃ PBS, probably due to unknown degradation mechanisms in higher temperature.

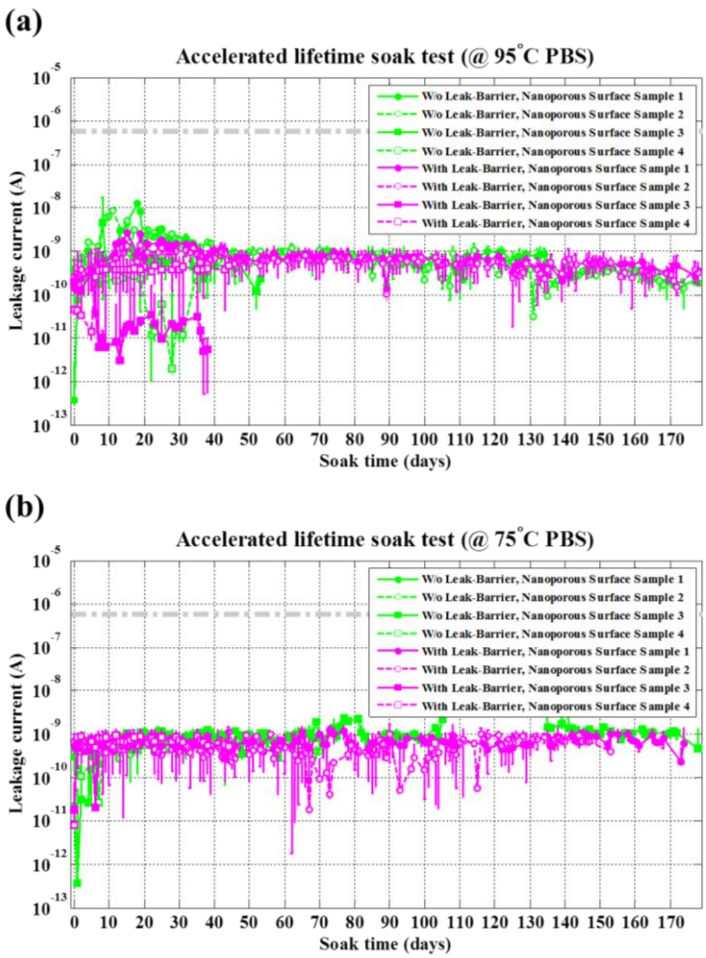

Figure 3.19 Ongoing accelerated soak test results in (a) 95 ℃ and (b) 75 ℃ PBS.

3.5 Comparative Analysis of the Manufacturing Cost of the LCP- and Titanium-based Cochlear Implants

Detailed manufacturing cost analysis of the titanium- and LCP-based cochlear implant is summarized in Table 3.2 and 3.3, respectively. Manufacturing cost per unit of the titanium-based cochlear implant is approximately $3,174. Contrary to metal-based device, manufacturing cost per unit of the LCP-based device is only $245 which is about one thirteenth of those of metal-based device. Figure 3.20 (a) shows the cost distribution chart relative to total manufacturing cost in titanium-based device. Direct labor cost is the largest portion in the manufacturing cost, and it means that conventional titanium-based cochlear implants are fabricated by labor-intensive processes. Direct material cost is the second-largest part of the cost. Conventional titanium-based device consist of expensive materials such as platinum-iridium alloy and medical grade titanium (Ti-6Al-4V). Especially, thick platinum coil, platinum feedthroughs, and platinum-iridium wires for cochlear electrode array greatly increase the material cost of the titanium-based cochlear implant. Figure 3.20 (b) shows the manufacturing cost distribution chart of the LCP-based cochlear implant. Unlike titanium-based device, direct expense shows the largest portion in the cost. It is caused by relatively lower costs of materials and labor for LCP-based device. LCP-based thin-film cochlear electrode is fabricated by automated semiconductor processes instead of manual fabrication, and packaging is done by simplified thermal compression process in place of complicated packaging including brazing and welding. We assumed that

LCP-based cochlear electrode array is fabricated on the 6" wafer. Ten electrode arrays can be fabricated onto the 6" wafer. We can further decrease the manufacturing cost of the electrode when we use larger wafers. Also, RF coil is integrated into the circuit board in the LCP-based device. Thus, we can save the material cost of thick platinum wire which is used in titanium-based device. Also, integrated planar coil is composed of copper which has higher conductivity than platinum. Thus, miniature transformer for scaling coil voltage is no longer necessary. Again we can reduce the direct material costs for ferrite bobbins and copper litz wires. On the other hand, stimulator IC is fabricated by semiconductor foundry, and this cost is allocated into the direct expense. This factor is not changed in both types of devices. As a result, the direct expense has relatively higher portion in Figure 3.20 (b).

Table 3.2 Summary of manufacturing cost analysis of the titanium-based cochlear implant.

Titanium-based CI

I. Direct Manufacturing Cost (=Direct Materials + Direct Expense + Direct Labor)

Part	Sub-part	Details	Sub-part cost for 100 units	Cost Category	Fabrication Yield	Part cost considering Yield
Electrode array	Stimulation electrode array	Pt:Ir (90:10) wire	$16,380	Direct material cost	50%	$32,760
	Reference electrode	Pt:Ir (90:10) wire	$3,511	Direct material cost	50%	$7,022
		Pt:Ir casting	$293	Direct expense	100%	$293
	Silicone elastomer	MED-6233	$161	Direct material cost	50%	$322
	Fabrication	20 days, 5 workers to produce 100 units	-	Direct labor cost	-	-
Electronics	Discrete components	R, C, MOS, Diodes	$91	Direct material cost	100%	$91
	Stimulator chip	Chip foundry fabrication, chip bonding	$13,286	Direct expense	100%	$13,286
	Miniature transformer	Winding	$1,463	Direct expense	100%	$1,463
	Printed circuit board	Fabrication	$300	Direct expense	100%	$300
Package and magnet	Titanium electronics housing	Ti-6Al-4V ELI alloy	$6,338	Direct material cost	100%	$6,338
		Machining	$19,500	Direct expense	100%	$19,500
	Ceramic plate	Alumina powder	$146	Direct material cost	100%	$146
		Alumina processing, sintering, shaping	$8,289	Direct expense	100%	$8,289
	Feedthroughs	TiNi67 filler metal, platinum feedthroughs	$8,113	Direct material cost	70%	$11,590
		Feedthrough casting	$293	Direct expense	100%	$293
	Silicone elastomer	MED-6233	$146	Direct material cost	100%	$146
	Titanium magnet cases	Ti-6Al-4V ELI alloy	$400	Direct material cost	100%	$400
	Titanium magnet cases	Machining	$800	Direct expense	100%	$800
	Magnet	Neodymium magnet	$59	Direct material cost	100%	$59
	Packaging (brazing, welding)	100 days by 1 worker	-	Direct labor cost	-	
	Final silicone elastomer molding	25 days by 2 workers	-	Direct labor cost	-	
Coil	Platinum coil	Thick platinum wire	$42,471	Direct material cost	100%	$42,471
1. Direct Materials Cost to Produce 100 units				-		**$101,345**
2. Direct Expense to Produce 100 units				-		**$44,224**
3. Direct Labor Cost to Produce 100 units				(145 days x 8 workers x 100 $/day)		**$116,000**

We assumed that daily wage for the production worker is 100 $, and jobs of all workers to be maintained during the period of device production.

Table 3.2 (Cont'd)

II. Indirect Manufacturing Cost (or Manufacturing Overhead)

Category	Assumption	Depreciation cost during the period of 100 units production (145 days)
Indirect manufacturing costs to produce "100 units" of titanium-based cochlear implant	· Indirect manufacturing cost = Depreciation cost of facilities · Total Cost of Facilities: see table below* · Period of depreciation: 10 yrs · Method of depreciation: straight-line method	**$55,815**

Depreciation cost = (Total cost of facilities/10yrs) x 145 days

Category	Item	Use	Cost per unit	Quantity	Cost
Facilities to produce titanium-based cochlear implant	Clean room	-	$1,000,000	1	$1,000,000
	Vacuum furnace	Brazing between feedthroughs and ceramic plate (or titanium case)	$200,000	1	$200,000
	Resistive welding machine	Platinum wire and feedthrough welding	$150,000	1	$150,000
	Laser welding machine	Weld titanium cases	$30,000	1	$30,000
	Microscope	Electrode fabrication, molding, brazing	$3,000	8	$24,000
	Dispenser	Molding	$500	2	$1,000
	Total cost of facilities	-	-	-	**$1,405,000**

► *Manufacturing Cost (=Direct Manufacturing Cost + Indirect Manufacturing Cost)*

Sum of Manufacturing Cost (100 units of Titanium-based CI)	**$317,384**
Manufacturing Cost per unit	**$3,174**

Sum of manufacturing cost (100 units) = (Direct Materials Cost+Direct Expense+Direct Labor Cost) +(Indirect Manufacturing Cost)

Table 3.3 Summary of manufacturing cost analysis of the LCP-based cochlear implant.

LCP-based CI

I. Direct Manufacturing Cost (=Direct Materials + Direct Expense + Direct Labor)

Part	Sub-part	Detailed materials and processes	Sub-part cost for 100 units	Cost Category	Fabrication Yield	Part Cost considering Yield
Electrode array (fabricated with 6-inch wafer)	Substrate and cover	Kuraray LCP film	$1,000	Direct material cost	90%	$1,111
	Silicone elastomer	MED-6233	$161	Direct material cost	100%	$161
	Semiconductor Process	2 days by 2 workers	-	Direct labor cost	-	-
Electronics	Discrete components	R, C, MOS, Diodes	$91	Direct material cost	100%	$91
	Stimulator chip	Chip foundry fabrication, chip bonding	$13,286	Direct expense	100%	$13,286
	Printed circuit board with patterned coil	Fabrication	$300	Direct expense	100%	$300
Package and magnet	Polymer package	Kuraray LCP film	$1,000	Direct material cost	100%	$1,000
	Silicone elastomer	MED-6233	$146	Direct material cost	100%	$146
	Titanium magnet cases	Ti-6Al-4V ELI alloy	$400	Direct material cost	100%	$400
	Titanium magnet cases	Ti-6Al-4V machining	$800	Direct expense	100%	$800
	Magnet	Neodymium magnet	$59	Direct material cost	100%	$59
	LCP packaging (lamination)	2 days by 1 worker	-	Direct labor cost	-	-
	Final silicone elastomer molding	3 days by 2 workers	-	Direct labor cost	-	-
Coil	-	None (integrated into the circuit board)	-	-	-	-
1. Direct Materials Cost to Produce 100 units			-			**$2,968**
2. Direct expense to Produce 100 units			-			**$14,386**
3. Direct Labor Cost to Produce 100 units			(7 days x 5 workers x 100 $/day)			**$3,500**

We assumed that daily wage for the production worker is 100 $, and jobs of all workers to be maintained during the period of device production.

Table 3.3 (cont'd)

II. Indirect manufacturing cost (or Manufacturing Overhead)

Category	Assumption	Depreciation cost during the period of 100 units production (7 days)
Indirect manufacturing costs (Depreciation costs of facilities) to produce "100 units" of LCP-based cochlear implant	· Indirect manufacturing cost = Depreciation cost of facilities · Total Cost of Facilities: see table below** · Period of depreciation: 10 yrs · Method of depreciation: straight-line method	**$3,632**

Depreciation cost = (Total cost of facilities/10yrs) x 7 days

(Based on Facilities of ISRC, SNU)

Category	Item	Use	Cost per unit	Quantity	Cost
Facilities to produce LCP-based cochlear implant	Clean room (yellow room)	-	$1,000,000	1	$1,000,000
	Inductively coupled plasma etcher	Film cleaning (package, electrode array)	$170,000	1	$170,000
	E-gun evaporator	Metal deposition (electrode array)	$200,000	1	$200,000
	Spin coater	Photoresist spin coating (electrode array)	$15,000	1	$15,000
	Hot plate	Photoresist baking (electrode array)	$5,000	1	$5,000
	Mask aligner	Photolithography (electrode array)	$270,000	1	$270,000
	Wet station	Metal patterning (electrode array)	$22,000	1	$22,000
	Electroplating machine	Patterned metal thickening (electrode array)	$4,000	1	$4,000
	Heat Press machine	LCP lamination (package, electrode array)	$12,000	4	$48,000
	Laser cutting machine	LCP film cutting (package, electrode array)	$150,000	1	$150,000
	Microscope	Molding (electrode array)	$3,000	3	$9,000
	Dispenser	Molding (package, electrode array)	$500	2	$1,000
	Total cost of facilities	-	-	-	**$1,894,000**

► *Manufacturing Cost (=Direct Manufacturing Cost + Indirect Manufacturing Cost)*

Sum of Manufacturing Cost (100 units of LCP-based CI)	**$24,486**
Manufacturing Cost per unit	**$245**

Sum of manufacturing cost (100 units) = (Direct Materials Cost+Direct Expense+Direct Labor Cost) +(Indirect Manufacturing Cost)

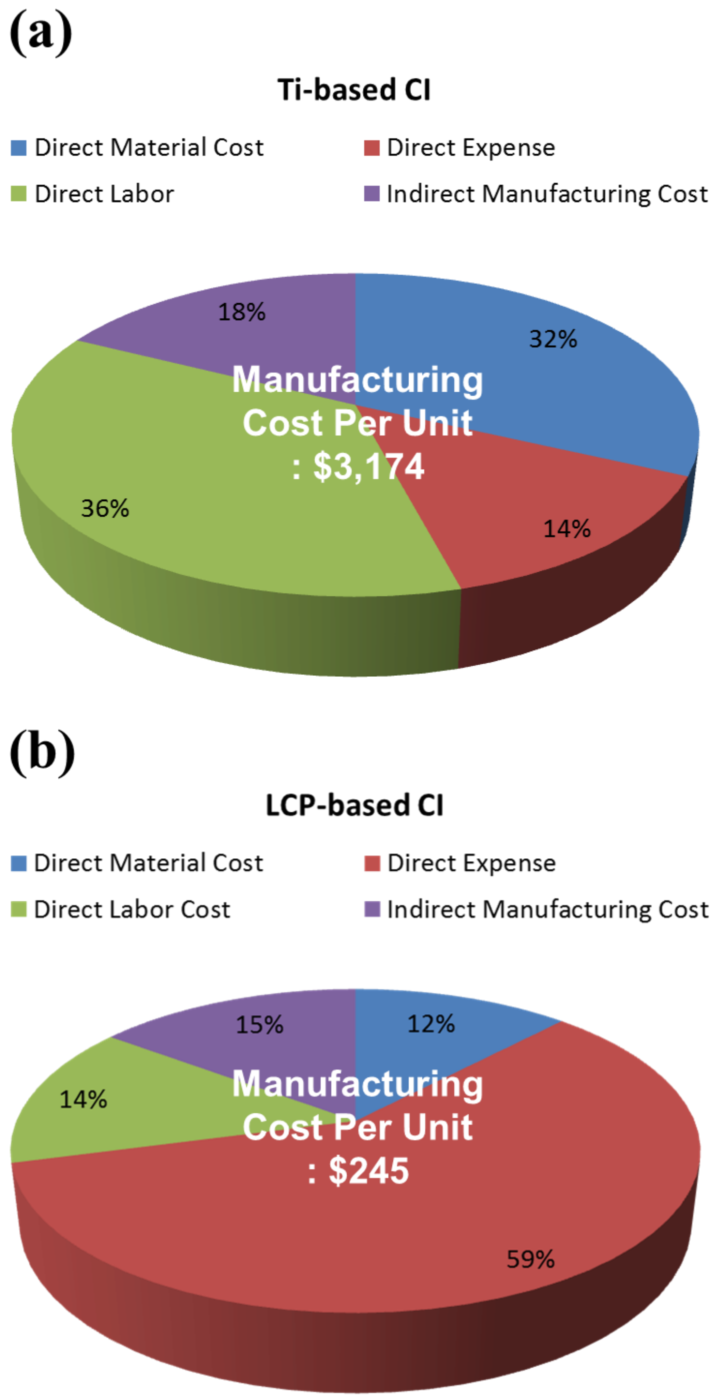

Figure 3.20 Distribution of costs of the (a) titanium- and (b) LCP-based cochlear implants.

Aforementioned trend is apparent in the cost ratio chart of each functional part in both devices. Figure 3.21 (a) and (b) show the distributions of costs per part percentage of the titanium- and LCP-based device, respectively, when considering cost for direct materials and direct expenses only. In the titanium-based device, electronics have the smallest ratio (10%) of the cost, whereas package, coil, electrode array have significantly higher ratio (about 30 %). In the LCP-based device, however, ratio of the electronics (79 %) shows remarkably larger than other parts of the device.

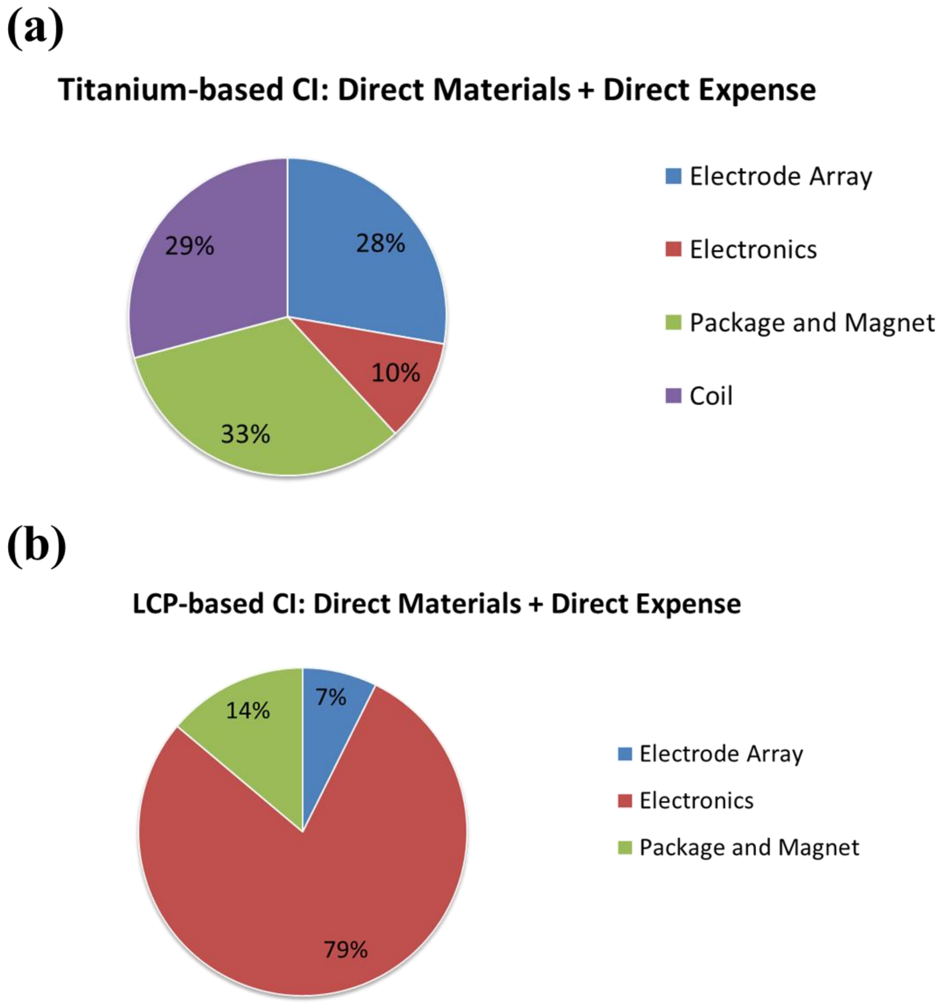

Figure 3.21 Distribution of costs per functional part of the (a) titanium- and (b) LCP-based cochlear implants.

Chapter IV

Discussion

4.1 LCP-Based Electronics Packaging

In this study, we developed novel LCP electronics packaging technique for polymer-based cochlear implant. Conventional LCP packaging method used thermoformed LCP cover which has higher melting temperature, additional laser cut LCP bonding layer which has lower melting temperature, and PDMS as a filling material of cavity. Due to the presence of PDMS, thermal lamination process should be done with localized cooling of PDMS filled cavity. Also, additional custom metal jigs for thermoforming and packaging are required. In developed packaging processes, we use only one type of LCP film which has lower melting temperature. Without thermoforming process of LCP cover, laser cut LCP films are stacked to create recessed cavity for electronics. Stimulator IC and discrete components are placed into the cavity. Stacked multilayers are laminated with thermal press without additional cooling process. LCP package using newly developed technology is more compact and thinner than those of conventional device. Moreover, developed packaging process is time-efficient and much simpler than conventional titanium-based packaging technique. We need only multiple sheets of low temp LCP films processed by laser cutting machine.

Development of aforementioned packaging techniques was achieved through several trials and errors. In first packaging method, we used 1 mm thick high temp LCP guard to protect interconnection wires of the stimulator IC. Due to the presence of the guard structure, height difference in the package stack-up was occurred. Most pressure was applied to not a border of packaging layer, but a chip protection guard. As a result, many wrinkles were generated due to non-uniform pressure. We showed that wrinkles of the package were act like a water permeation path. As a second packaging method, we have modified the structure of press jig so that localized pressure was applied to border area of the package while suppressing the wrinkle generation. Although amount of wrinkles were greatly reduced, there still exist small size wrinkles. Thus, uniform pressure applied to the package stack-up is especially important for successful LCP packaging of electronics. If there is height difference in the package stack-up, compensating materials which have higher degradation temperature than LCP (e.g., Teflon) or specialized metal jig should be applied.

4.2 Comparison of LCP-Based Cochlear Implant to Conventional Metal-Based Cochlear Implant

Conventional cochlear implants employ titanium-based electronics housing and platinum-iridium (90:10) wire-based electrode array. Ceramics such as Al_2O_3 are also used as a casing material for cochlear implant. However, the material is more brittle than titanium and thus more prone to breakage under significant mechanical stress [58, 59]. Concerto® of the Med-El is the smallest device among titanium-based cochlear implant. Figure 4.1 shows the size of the LCP-based cochlear implant in comparison with commercial devices. The figure is modified from [60]. Dimensions of the developed LCP-based device are about 40 % smaller than Concerto® device. Furthermore, LCP-based device is approximately 25 % thinner than Concerto® device when regardless of an alignment magnet. Compact and thin device enables less-invasive procedures with less-morbidity and improved cosmesis.

In titanium-packaged devices, electrical signals enter and exit from the metal package through hermetic feedthroughs. Feedthroughs are insulated by ceramic or glass plate. The number of feedthroughs increases proportionally to the number of sites. Feedthroughs are hermetically sealed by active brazing process using TiNi-50® active filler metal. Brazing is extremely time-consuming, labor-intensive, and low-yield process. In our experience, brazing yield of skilled worker who have two year’s brazing experience is only 70 %. Furthermore, feedthrougs are principal failure part of hermetic sealing in conventional titanium-based cochlear implants. In 2006, Advanced Bionics Corporation conducted product recall due to moisture ingression into the titanium package through the feedthrough. The reliability issues of titanium-based cochlear implant will be further discussed in section 4.4.

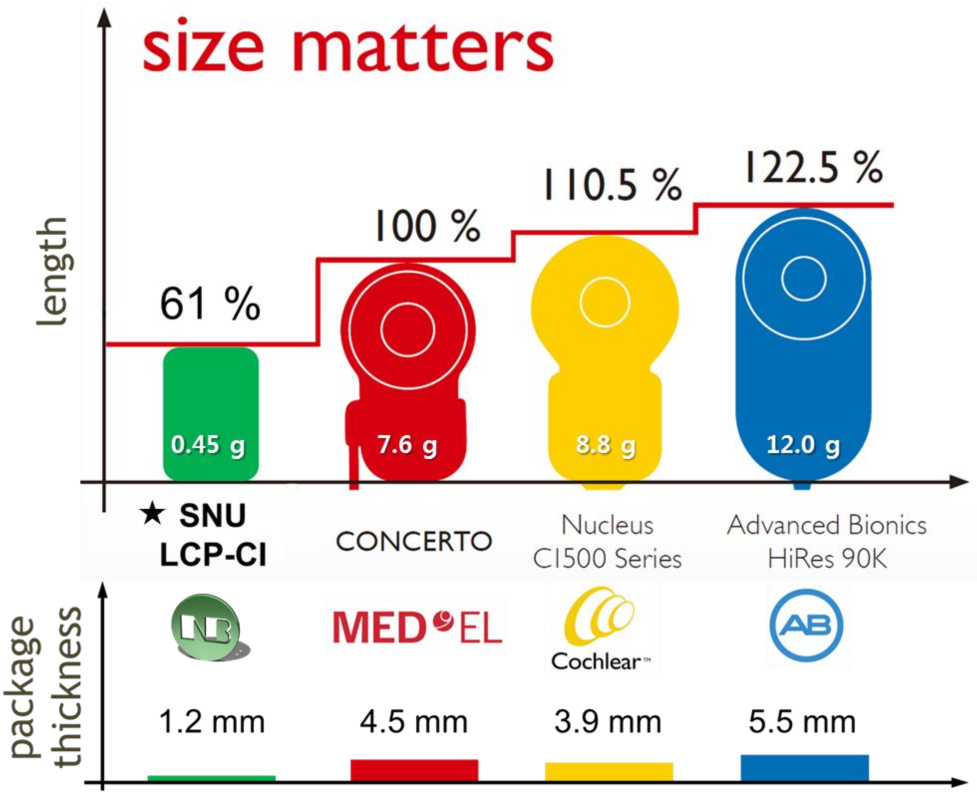

Figure 4.1 Size of the LCP-based cochlear implant in comparison to commercial devices. Alignment magnet was not considered in the package thickness. The figure was modified from [60].

4.3 Effectiveness of the LCP-Based Cochlear Implant

We verified the effectiveness of the developed LCP-based cochlear implant through an *in vivo* animal study. The device was fully implanted and EABRs as objective measure of hearing perception were measured in the guinea pig. In measured responses, increase in peak amplitude as a function of stimulus amplitude was apparently appeared. As shown in Figure 3.10 (b), two peaks in 1 and 2 ms were prominent. In auditory evoked auditory brainstem response (ABR), peak latency becomes shorter with increase of sound intensity due to sound propagation or synaptic delay. In contrast, latencies for the EABR are not changed with electrical stimulation intensity. Moreover, absolute latencies for the EABR are shorter than typical ABR values because electrical stimulus was directly delivered to the intracochlear electrode array not in tympanic membrane and ossicular chain in the middle ear. Figure 4.2 (a) and (b) show the EABRs in the guinea pig adopted in other literatures [61, 62]. In Figure 4.2 (a), stimuli were presented through a bipolar electrode pair inserted into the base of the cochlear to a depth of approximately 3 mm, and cathodic first biphasic current pulses with pulse duration of 20 μs/phase were used to evoke EABR. In Figure 4.2 (b), a stimulation electrode was positioned in the apical region of the scala tympani and a reference electrode was positioned in the Eustachian tube. Biphasic voltage pulses with pulse duration of 150 μs were used to evoke EABR. In both of Figure 4.2 (a) and (b), prominent positive peaks are presented around 1 and 2 ms similarly to Figure 3.10 (b) and 3.11 (a). In our study, we placed the reference or return electrode into the dorsal area of the guinea pig due to the relatively long length of the human cochlear electrode array. To increase the amount of current delivered to the spiral ganglion cell, a position of reference electrode will be modified to other region such as temporalis muscle or temporal skull using a fixation screw.

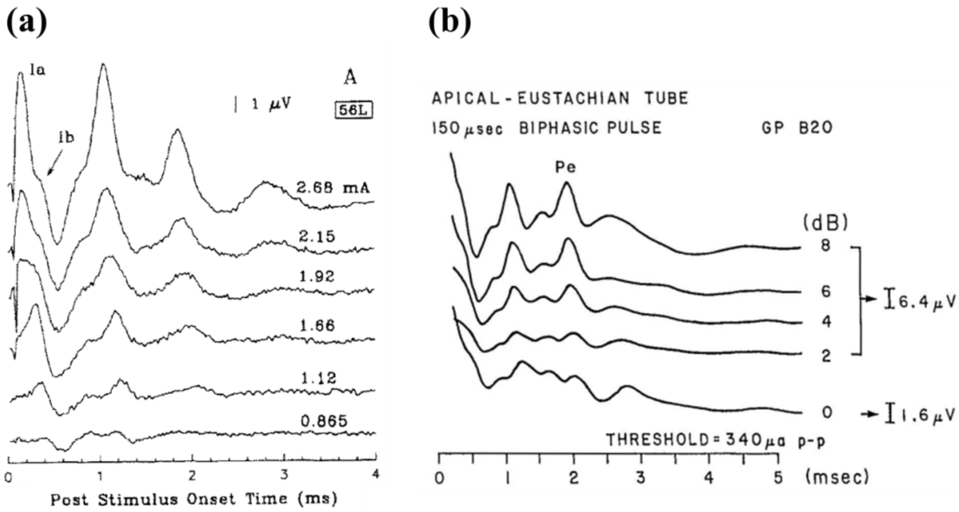

Figure 4.2 Reference EABR waveforms in the guinea pig. (a) and (b) were adopted from [61] and [62], respectively.

4.4 Reliability of the Titanium- and LCP-Based Neural Prostheses

In conventional titanium-based packaging, helium leak measurement is the general approach to quantify the hermeticity of the sealed package. However, organic polymers including LCPs are naturally absorb the helium, and thereby correct helium leakage through actual interfacial leakage path is difficult to measure. In some studies, helium leakage was measured after sufficient dwell time for eliminating helium elements absorbed onto LCP surface [48, 63]. They showed that an LCP cavity can achieve a measured fine leak rate of 3.7 x 10^{-8} atm-cc/s after 3 hours of dwell time [48, 63]. The leak rate was also similar to the value through optical leak rate testing which was not affected by helium adsorption on the LCP surface.

Although passing the relatively easy helium leak is desirable, it should not be touted as proof of hermeticity [64]. Helium leak test shows only the hermeticity of the device immediately after manufacturing. Long-term hermeticity or reliability is affected by several factors, including mechanical stress, status of sealing, moisture level, structure of the package, and so forth. Especially, feedthroughs are often a primary source of failure in many packages [65]. Figure 4.3 (a) shows the conceptual cross-sectional diagram of the titanium-based implant. Many feedthroughs for interconnection of stimulator IC and coil are insulated by ceramic plate, and thereby produce multiple braze joints. Feedthroughs protruding out of the titanium housing are encapsulated by silicone rubber which has higher water permeation. Accordingly, feedthroughs are exposed to body fluid after implantation. Although brazed joints show high helium leak rate of 1.0 x 10^{-10} atm-cc/s, increased number of sealed joints raises possibility of failure in hermetic sealing. $C\hat{o}t\acute{e}$ et al. reported the cause of failure in terms of cochlear reimplantation [66]. In case of hard failures, about 50 % of these were related to the corrosion of electronic parts because of high moisture levels inside the device as caused by a broken hermetic seal which was mainly due to feedthrough pin. Advanced Bionics Corporation performed global notification recall in 2006 due to loss of hermetic seal at feedthrough component. In 2011, Cochlear Ltd. also performed voluntary recall of Nucleus 5 [67]. They have noticed that a loss of hermeticity from unexpected variations in the brazing process during manufacturing. Variations in the brazing process have resulted in a limited number of implants being more susceptible to developing microcracks in the braze joints during subsequent manufacturing steps. These microcracks allow water molecules to enter the implant resulting in the malfunction of specific components.

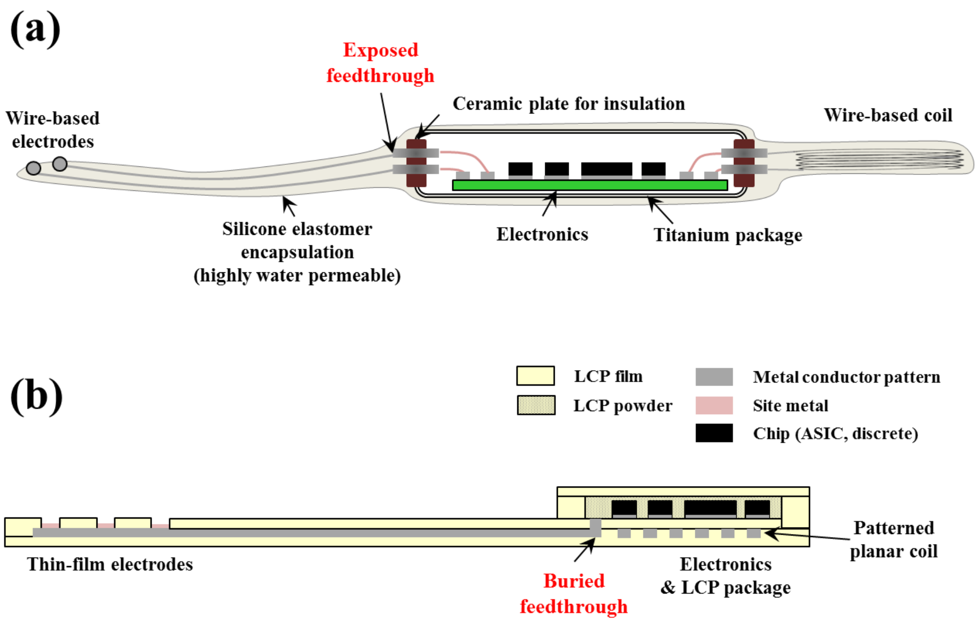

Figure 4.3 Cross-sectional diagrams of (a) titanium- and (b) LCP-based implantable devices.

Figure 4.3 (b) shows the cross-section of the LCP-based device. In the LCP-based devices, feedthrough patterns were buried in LCPs. Thus, feedthroughs were not exposed directly to the salted body fluid. However, water can permeate into the electronics package through electrode sites in the LCP-based device. To mitigate the water permeation via electrodes, we developed the leak-barrier structure. We showed that the leak-barrier structure which has microscale barrier structures and a nanorporous surface is helpful to achieve long-term reliability through highly accelerated lifetime soak tests in 110 °C PBS. Proposed leak-barrier structure enables increment of water leakage path length as well as mechanical interlocking force between polymer cover and metal layer.

Optimal adhesion or joint strength between two materials is multiplication of mechanical interlocking component and interfacial chemical effects as following equation [68].

$$\begin{aligned}\text{Optimal joint strength} = {} & (\text{constant}) \\ & \times (\text{mechanical interlocking component}) \\ & \times (\text{interfacial chemical component})\end{aligned}$$

Interfacial chemical bonding is dependent on the reactive willingness of both materials involved [54]. Noble metals such as gold and platinum have been widely used for sites and interconnection lines in polymer-based device as shown in Figure 4.3 (b). These noble metals have no reactive willingness with organic polymers including LCPs. The polymer is only attached to the electrode surface by intermolecular electrostatic and van der Waals force that are types of weak chemical bonding [69]. For further enhancement of reliability, we tried to the use chemical bonding between LCP cover and metal layer. Figure 4.4 (a) shows the test sample with an additional titanium layer for adhesion promotion between LCP and metal layer. Titanium which is one of the transition metals is capable of easily forming chemical bonding with LCP. Figure 4.4 (b) shows the IDE part of the titanium deposited electrode before LCP cover lamination.

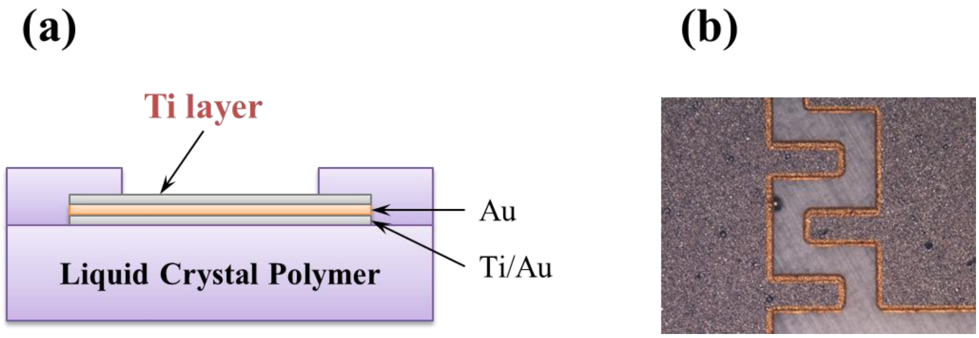

Figure 4.4 (a) Cross-section of the test sample with additional titanium layer for adhesion promotion between LCP and metal layer. (b) IDE part of the titanium deposited test sample before lamination.

As a one possibility of chemical bonding between LCP and titanium, hydrogen bonds can be formed when considering C=O of LCP and –OH (hydroxyl) of titanium surface. Dimethyl sulfoxide (DMSO) solution disrupts the hydrogen bonds between two materials. Thus, if we immerse the sample in DMSO solution, delamination between LCP cover and additional titanium layer should be occurred. However, we did not observe the delamination. It indicates that other chemical bonding exists in the interfacial joint. We performed X-ray photoelectron spectroscopy (XPS) analysis to verify binding states between titanium and LCP. Figure 4.5 (a) shows the cross-section of the test specimen for XPS analysis. Test specimen has e-gun evaporated 50 nm thick titanium layer and 200 nm gold layer on plasma treated LCP film. Figure 4.5 (b) presents XPS depth profile of the test specimen. Atomic concentrations of titanium, oxygen, and carbon are relatively higher at 250 nm depth which is interfacial boundary of the LCP and titanium. Figure 4.6 (a), (b), and (c) show the XPS spectrum of the oxygen, carbon, and titanium at 250 nm depth, respectively, and (d) presents the analyzed binding energy at the peak point and its binding state. It shows that formations of carbide and oxide bonding were created at the LCP-Ti interface. We expect that additional titanium layer for strong chemical bonding will be beneficial for enhancing long-term reliability of the polymer-based neural prostheses. Accelerated soak tests of titanium-deposited samples are now in progress.

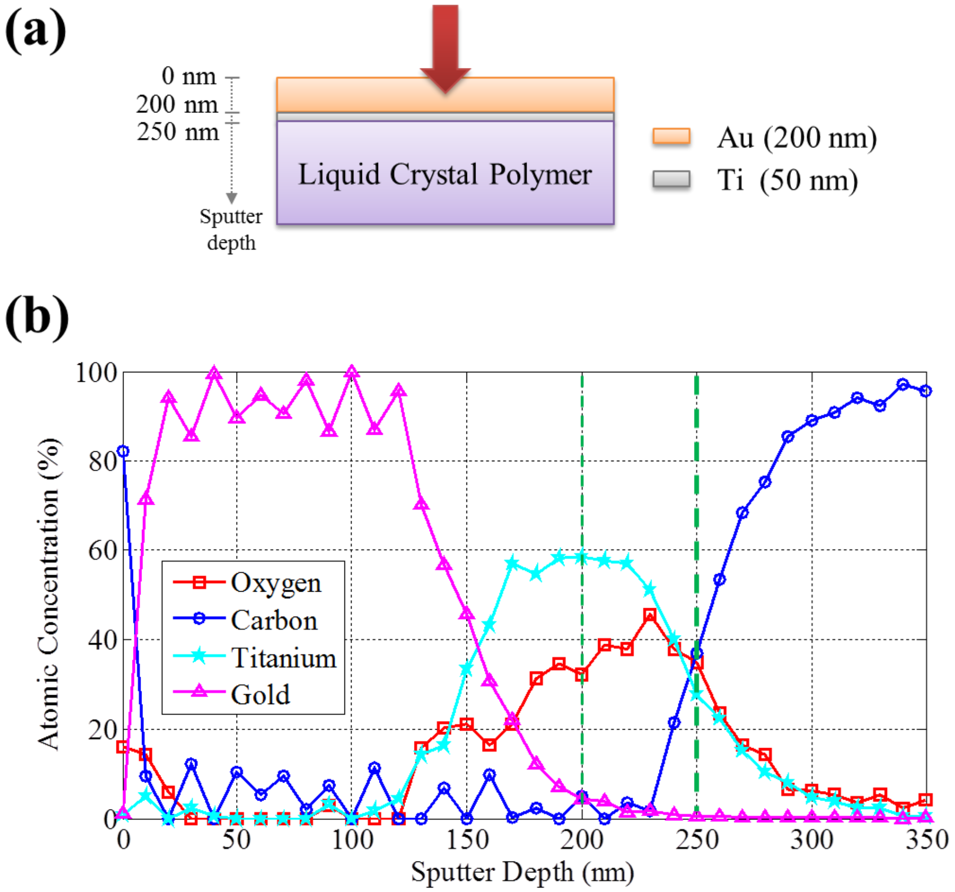

Figure 4.5 (a) Cross-section of the test specimen for XPS analysis. (b) XPS depth profile of the test specimen.

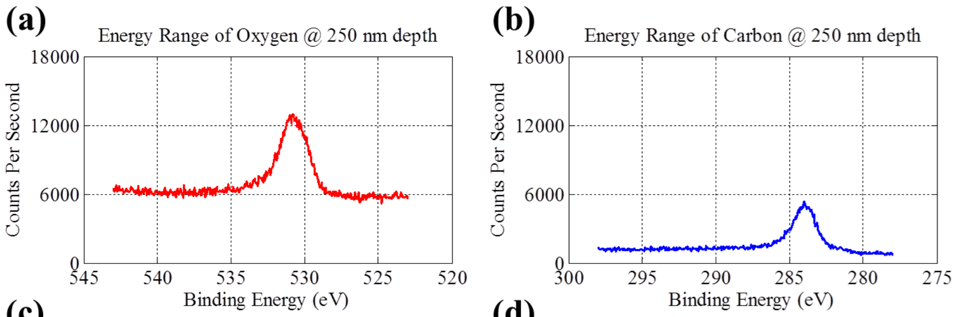

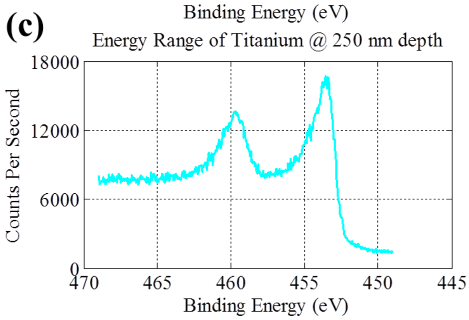

(d)

Binding Energy	***Binding State***
283.9 eV	C-H
459.1 eV	TiO_2
459.4 eV	$TiCl_3$
460.1 eV	TiC
530.8 eV	TiO
530.8 eV	TiO_2

Figure 4.6 (a)-(c) The XPS spectrum of the O1s, C1s, Ti2p, respectively.
(d) Binding energy at the peak point and its binding state.

4.5 MRI Compatibility

In this study, we compared the MR image artifacts caused by metal- and LCP-based cochlear implant systems. The magnitude of MR imaging artifact of the LCP-based one was much smaller than the metal implant in both 3.0 T and 7.0 T MR scans. It provides us with many possibilities to investigate the cognitive neuroscience or the top-down approach in neural pathway research; in particular, brain plasticity after deafness or cochlear implantation that is of interest among several researchers. One of the major reasons requiring such studies are that the variations of the cochlear implant performance depend on different patients. It has been reported that patients using the exact same cochlear implant system have a broad distribution of outcomes. For instance, some patients can hear monosyllabic words in noisy environments. On the other hand, there are patients who show poor sentence recognition even in a quiet situation. If we can monitor the auditory connectivity and the related brain plasticity while the functioning cochlear implant system remains inside the subject, it will be possible to develop a more powerful and effective cochlear implant system.

Recently, various innovative brain-imaging techniques have been developed, enabling us to understand the delicate structure and the functionality of the brain. Cho et al. [70] suggested a fusion PET-MRI system with a high-resolution research tomograph-PET and an ultra-high field 7.0 T MRI. Using this novel hybrid imaging technique, we can observe the human brain with higher temporal and spatial resolutions. Thus, MR compatibility with implantable neuroprosthetic devices will become increasingly more important along with the development of innovative high-Tesla MRI systems.

The MR compatibility is an unavoidable issue in all implantable neuroprosthetic devices, such as deep brain stimulation (DBS) systems and pacemakers. In DBS systems, electrical pulses are delivered through a macro electrode that is implanted into a subthalamic nucleus or internal globus pallidus (GPi). A conventional implantable pulse generator (IPG) of the DBS system is implanted in the chest area, and a long lead cable is used to connect the electrode array and the IPG. During MR scans, the long lead cable acts as a resonant antenna. Therefore, RF-induced heating occurs in the electrode sites [71-73]. This may lead to brain damage or a patient's death. To overcome this serious problem, some companies are currently developing a head mountable DBS system, which has no or very short lead wires. However, there remains an MR image artifact problem caused by metal packages of the implantable pulse generator (IPG). The use of LCP-based packages can minimize this artifact as shown in our study. It can also achieve an extremely smaller and thinner packaging for the IPG than conventional ones. Furthermore, a high-density LCP-based DBS microelectrode array can be monolithically assembled using automated semiconductor thin-film processes.

Although we showed that higher MRI compatibility of LCP-based device than conventional metal-based implant, the most harmful factor in the MR environment is the implant magnet for the coil alignment, because MRI machines use superconducting magnets for the hydrogen alignments of the body. Even though a compression dressing can keep the magnet from moving in the MRI machine, an exposure to the strong magnetic field can cause the demagnetization or the polarity change of the magnet [74, 75]. Furthermore, the magnet can severely deteriorate the MR images [76, 77]. In the commercial cochlear implant systems, the magnet can be removed temporarily during MR imaging even the local anesthesia and the small incision are necessary. In this study, we also conducted the 3.0 T and 7.0 T MR imaging of devices when alignment magnets were removed for safety. The magnet is placed in the silicone elastomer pocket, so it can be easily removed and put in. Apart from the MRI incompatibility, the use of the magnet frequently causes discomfort such as irritation or soreness of the skin due to continuous pressure on skin. Especially, skin inflammation commonly occurs in children due to their premature skin [78]. If inflammation fails to resolve after loosening the magnet, use of the cochlear implant should be discontinued temporarily. To overcome these problems, i.e., MRI incompatibility and discomfort of patients, magnetic attachment between the external processor and the implantable unit should be replaced by another alignment method. One solution to achieving magnet free attachment is to use eye glasses type speech processor. Figure 4.7 shows the conceptual illustration of the eye glasses type speech processor for cochlear implant as worn by user.

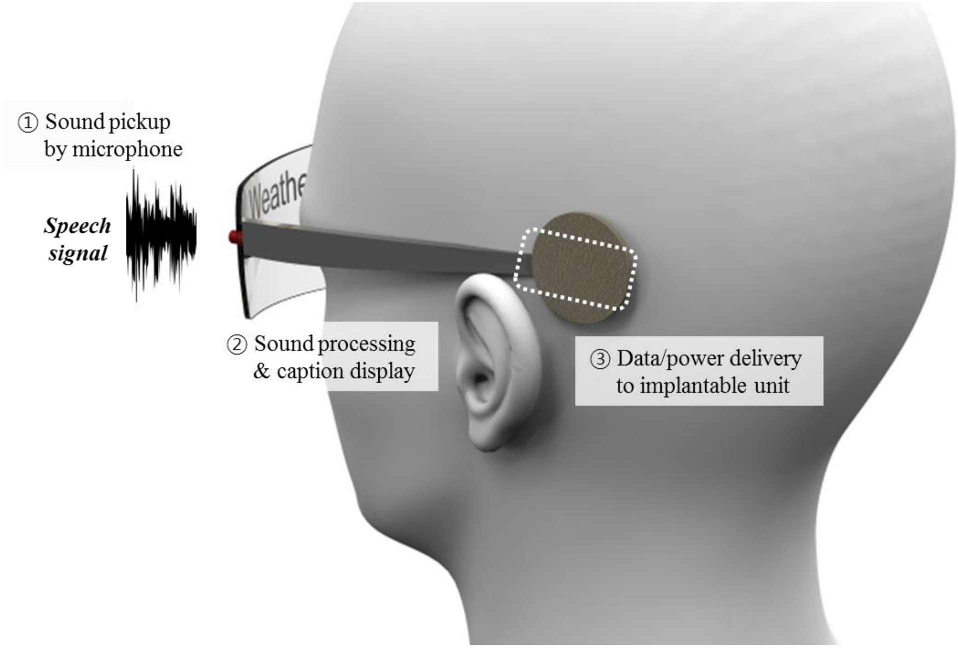

Figure 4.7 Illustration of the cochlear implant based on eye glasses type speech processor. Microphone and speech processing module are integrated into the leg or frame of the glasses. Transmitter coil is connected to the end of the frame-leg and interfaced with the LCP-based implantable unit.

Figure 4.8 (a) presents the conceptual figure of the novel cochlear implant system based on eye glasses type speech processor and the LCP-based implantable unit. Microphone and speech processor are integrated into the glasses legs or frames, and transmitting coil is connected to the end of the frame-leg. Also, small and thin LCP-based implantable unit including a planar coil is placed beneath the temporal skin. Two coils are naturally aligned without the magnet when patients wear glasses. Thus, we can achieve a fully MRI compatible system and maximize patient's comfort. According to the receiving coil location, two types of implantable units are possible as shown in Figure 4.8 (b). In the first type, the coil is stacked on the electronic board in multi layered form. LCP encapsulated electronics part including the coil is implanted in the mastoid pocket and interfaced with the eye glasses type speech processor. In the second type, the coil is separately located from the electronic board. The electronic board is implanted in the small mastoid pocket and the planar receiving coil is folded over the electronic board and placed outside of the mastoid or the temporalis muscle as illustrated in Figure 4.8 (c). Therefore, distance between transmitting and receiving coil is decreased, and more efficient coil coupling can be achieved. Skin thickness varied across patients from 4.1~9.0 mm in adults and 2.5~5.9 in children [79]. With the LCP-based device with a separated coil (type 2 in Figure 4.8 (b)) structure, we can prevent the telemetry failure or unstable inductive coupling in patients who have thick skin or temporalis muscle. Eye glasses type speech processor is also beneficial for better speech perception with visual cues. If we integrate the displaying module into the lens of the glasses, keyword captions or graphics which are helpful for understanding the complicated sentences or music will be displayed through the lens like a Google glass. Therefore, proposed cochlear implant system based on eye glasses type speech processor and miniaturized LCP-based device is helpful to realize patient friendly device as well as MRI compatible unit through removing magnet link.

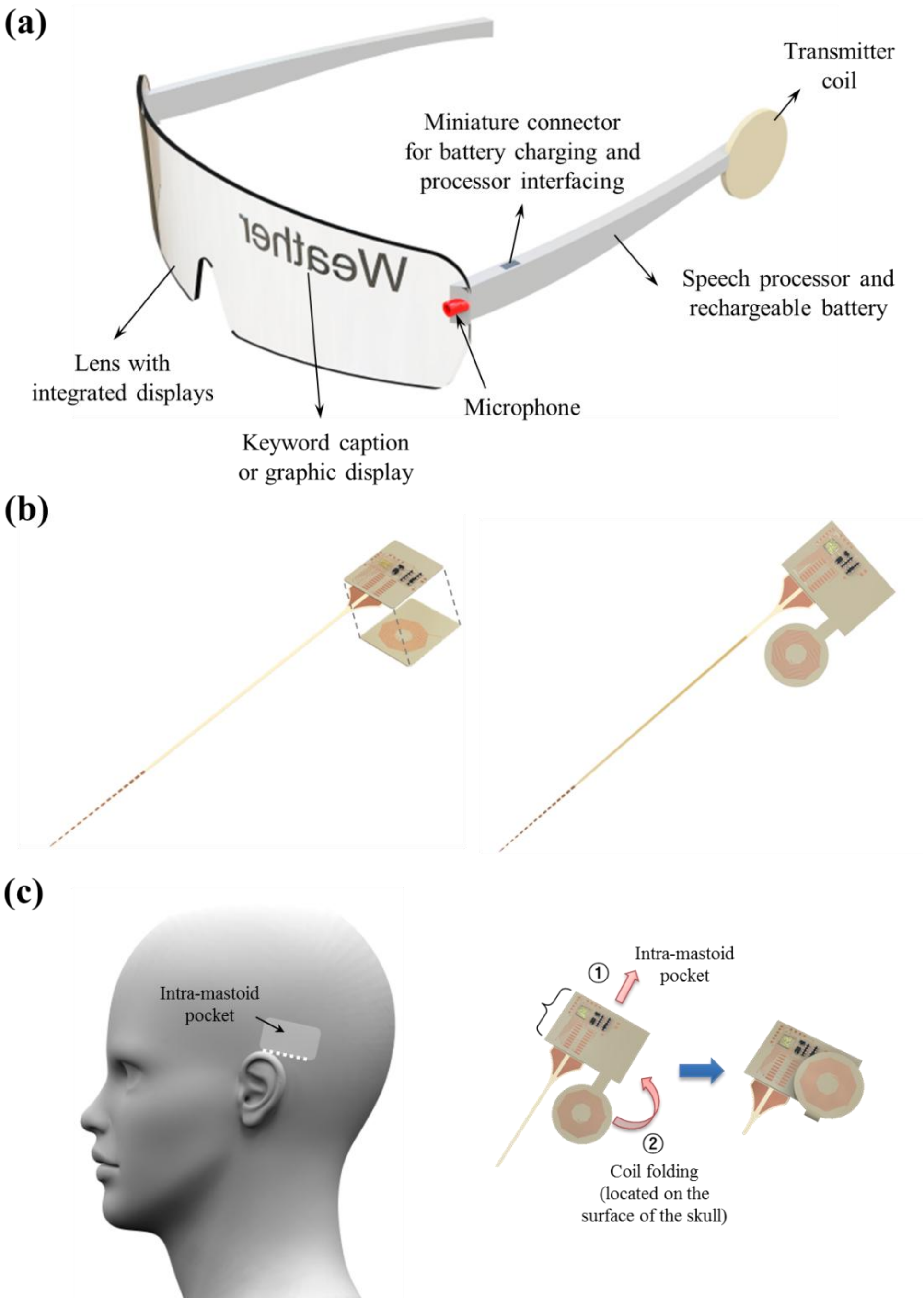

Figure 4.8 (a) Components of the eye glasses type speech processor. (b) Two types of LCP-based implantable unit according to the location of the planar type receiving coil (type 1: stacked coil, type 2: separated coil). (c) How to implant a device based on type 2 coil.

Moreover, the proposed device is advantageous to construct bilateral cochlear implants or bimodal hearing device such as an electric acoustic stimulation (EAS). For EAS, hybrid devices that combine hearing aids and cochlear implants are used. With this method, preserved low frequency hearing of the cochlear is stimulated by way of a hearing aid, whereas high frequency hearing is provided by means of a cochlear implant [80]. EAS shows improved performance in noisy situations or with music appreciation, because they utilize the fine structure of the low and mid frequency range of the sound. The proposed eye glasses type speech processor in Figure 4.7 and 4.8 is beneficial to implement the EAS without increasing device dimensions and wearing additional unit.

4.6 Manufacturing Cost Analysis of the LCP-Based Cochlear Implant

Cost of the present-day cochlear implant is about $30,000, way out of the reach of most deaf people or their families in low-income countries. Table 4.1 adopted from [81] shows the classification of countries according to gross national income per capita. Most deaf people who live in developing countries cannot afford cochlear implants due to high cost of the device which is several times of their annual income. We investigated the detailed manufacturing cost of the conventional titanium- and newly proposed LCP-based cochlear implant. Manufacturing cost is lowered with increasing production volume. Figure 4.9 shows manufacturing cost per unit with varying the volume of annual production from 100 to 10,000 to apply the ‘economies of scale’. We assumed that fixed cost is identical to the depreciation cost per year (see Table 3.2 and 3.3). Indirect manufacturing cost can be fixed and not changed with the volume of annual prediction. Fixed costs are $140,500 and $189,400 in titanium- and LCP-based device, respectively. Slightly higher fixed cost of LCP-based device is caused by relatively expensive semiconductor equipment which replaces the manual fabrication. Even though higher fixed cost, LCP-based cost has lower manufacturing cost due to lower variable cost. Variable cost includes cost for direct labor, direct material, and direct expense. In case of annual production is 100 units, manufacturing cost per unit of the LCP-based device is about 50% of those of titanium-based device due to higher facility cost. With the increase of volume of annual production, manufacturing cost per unit of LCP-based device is greatly reduced because relatively higher fixed cost is cancelled out. There remains only variable cost when annual production is above 10,000. If annual production is more than 1,000, then we fabricate the LCP-based cochlear implant with only 10% cost of titanium-based device. This reduction in manufacturing cost enables disruptive opportunities for the use of LCP-based cochlear implants in low- and middle income countries.

The sales price of cochlear implants is affected by multiple factors such as high manufacturing costs, marketing costs, R&D costs, profits, and so forth, as shown in Figure 2.28. Furthermore, price strategy of the company is also important. Entry barrier of medical devices including neural implants is very high, because time-consuming and difficult pre-clinical testing is required for regulatory approval. In these conservative circumstances, market monopoly can occur by leading company. At present, cochlear implants industry is dominated by Cochlear ltd., which controls about 65 % of market worldwide [82]. The cochlear implant market has been increasing steadily since 1985. In general, when the volume increases, the sales price should drop as shown in Figure 4.9. Cochlear ltd. however still maintains high-price policy. It prevents market penetration in low- and middle-income countries. Thus, humanitarian purpose of the company is also important to lower the sales price as well as reduction of manufacturing cost.

Table 4.1 Gross national income; classifications of developing countries. Adopted from [81].

Income group	***Income, US $***	***Classification***
Low income	≤825	Developing
Middle income (lower)	826-3,254	Developing
Middle income (higher)	3,255-10,065	Developing
Higher income	≥10,066	Developed

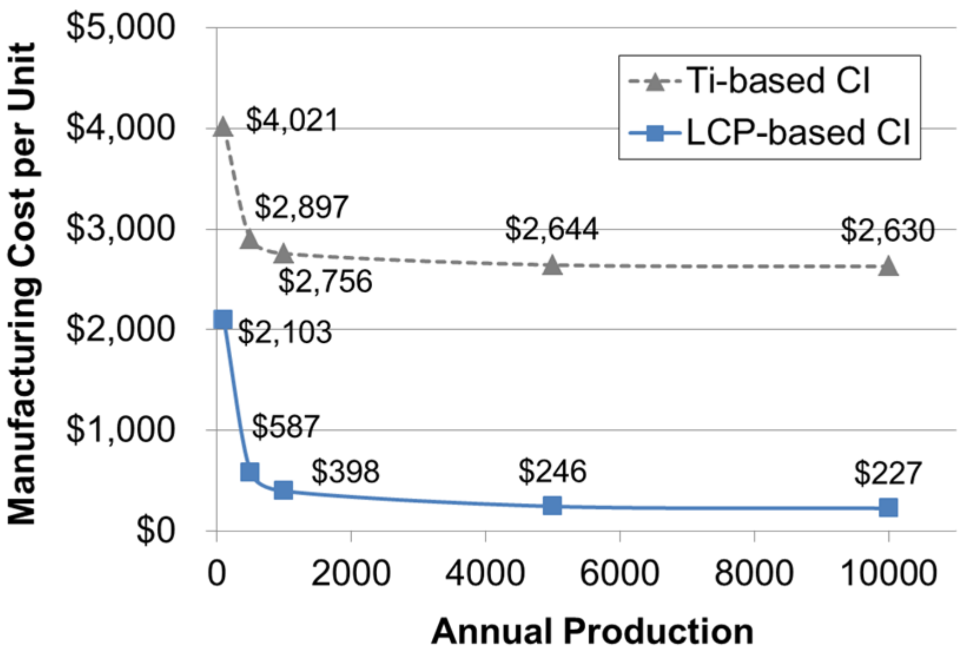

Figure 4.9 Economies of scale which presents manufacturing cost per unit with varying the volume of annual production from 100 to 10,000.

Chapter V

Conclusion

In the present study, we developed an LCP-based cochlear implant system using a newly developed electronics packaging technology. The developed packaging technology using recessed cavity enables the device packaging with a thin credit-card shape for miniaturized, simply fabricated and less invasive devices. Furthermore, all packaging layers are composed of same LCP films, which have a low melting temperature. Laser cut LCP films and thermal press are all we need for device packaging. Thus, developed packaging technology is simpler than conventional LCP packaging process and titanium-based hermetic sealing.

We also evaluated the effectiveness of the developed LCP-based cochlear implant system. EABR was successfully measured in the animal model. We also verified the MRI compatibility of the LCP-based device compared to a conventional metal-based device.

In order to enhance the long-term reliability of the LCP-based device, we developed leak-barrier structures which have a nanoporous surface and microscale barriers with an anti-trapezoidal cross-sectional shape. Aceelerated lifetime soak tests showed that both the nanoporous surface and microscale barriers significant contributions to improving the lifetime of the LCP-based electrode array.

We also conducted a manufacturing cost analysis of the LCP- and titanium-based cochlear implant system based on our group’s experience of manufacturing both devices for a better understanding of the detailed cost structure. The analysis showed that the developed LCP-based cochlear implant has a significantly lower cost with regard to the materials and labor. Manufacturing cost per unit is approximately 10 % of the cost of a conventional titanium-based cochlear implant.

Furthermore, the manufacturing cost is greatly reduced in proportion to the overall production. This result indicates that LCP with developed fabrication technologies enables truly low-cost manufacture of the cochlear implant while not sacrificing their performance metrics including effectiveness, long-term reliability, and MRI compatibility.

References

[1] A. R. Moller, *Hearing: anatomy, physiology, and disorders of the auditory system*: Academic press, 2006.

[2] P. C. Loizou, "Mimicking the human ear," *Signal Processing Magazine, IEEE,* vol. 15, pp. 101-130, 1998.

[3] B. S. Wilson, C. C. Finley, D. T. Lawson, R. D. Wolford, D. K. Eddington, and W. M. Rabinowitz, "Better speech recognition with cochlear implants," *Nature,* vol. 352, pp. 236-238, 07/18/print 1991.

[4] R. J. S. Briggs, H. C. Eder, P. M. Seligman, R. S. C. Cowan, K. L. Plant, J. Dalton, *et al.*, "Initial Clinical Experience With a Totally Implantable Cochlear Implant Research Device," *Otology & Neurotology,* vol. 29, pp. 114-119 10.1097/MAO.0b013e31814b242f, 2008.

[5] J. H. Park, J. H. Kim, Y.-K. Song, Y. Jung, S. Hur, W. Kim, *et al.*, "Design of an analog front end for a bio-inspired auditory sensor of a novel totally implantable cochlear implant," *Sensors and Materials,* vol. 25, pp. 553-565, 2013.

[6] H. Shintaku, T. Inaoka, T. Nakagawa, S. Kawano, and J. Ito, "Electrically Evoked Auditory Brainstem Response by Using Bionic Auditory Membrane in Guinea Pigs," *Journal of Biomechanical Science and Engineering,* vol. 8, pp. 198-208, 2013.

[7] T. Inaoka, H. Shintaku, T. Nakagawa, S. Kawano, H. Ogita, T. Sakamoto, *et al.*, "Piezoelectric materials mimic the function of the cochlear sensory epithelium," *Proceedings of the National Academy of Sciences,* vol. 108, pp. 18390-18395, 2011.

[8] K. D. Wise, P. T. Bhatti, J. Wang, and C. R. Friedrich, "High-density cochlear implants with position sensing and control," *Hearing Research,* vol. 242, pp. 22-30, 8// 2008.

[9] B. S. Wilson, S. Rebscher, F.-G. Zeng, R. V. Shannon, G. E. Loeb, D. T. Lawson, *et al.*, "Design for an inexpensive but effective cochlear implant," *Otolaryngology - Head and Neck Surgery,* vol. 118, pp. 235-241, 2// 1998.

[10] S. K. An, S. I. Park, S. B. Jun, C. J. Lee, K. M. Byun, J. H. Sung, *et al.*, "Design for a simplified cochlear implant system," *IEEE Trans Biomed Eng,* vol. 54, pp. 973-82, Jun 2007.

[11] S. K. An, S. I. Park, C. J. Lee, K. M. Byun, K. S. Min, J. M. Lee, *et al.*, "DESIGN FOR A SIMPLIFIED COCHLEAR IMPLANT SYSTEM," in *Conference on Implantable Auditory Prostheses,* Lake Tahoe, CA, 2007.

[12] T. Stieglitz, "Manufacturing, assembling and packaging of miniaturized neural implants," *Microsystem Technologies,* vol. 16, pp. 723-734, 2010/05/01 2010.

[13] F.-G. Zeng, "Cochlear implants: Why don't more people use them?," *The Hearing Journal,* vol. 60, pp. 48-49, 2007.

[14] N. Yoshikawa, B. Hirsch, and F. F. Telischi, "Cochlear Implant Fixation and Dura Exposure," *Otology & Neurotology,* vol. 31, pp. 1211-1214 10.1097/MAO.0b013e3181dd1400, 2010.

[15] S. E. Lee, S. B. Jun, H. J. Lee, J. Kim, S. W. Lee, C. Im, *et al.*, "A flexible depth probe using liquid crystal polymer," *Biomedical Engineering, IEEE Transactions on,* vol. 59, pp. 2085-2094, 2012.

[16] S. W. Lee, J.-M. Seo, S. Ha, E. T. Kim, H. Chung, and S. J. Kim, "Development of microelectrode arrays for artificial retinal implants using liquid crystal polymers," *Investigative ophthalmology & visual science,* vol. 50, pp. 5859-5866, 2009.

[17] E. T. Kim, C. Kim, S. W. Lee, J.-M. Seo, H. Chung, and S. J. Kim, "Feasibility of microelectrode array (MEA) based on silicone-polyimide hybrid for retina prosthesis," *Investigative ophthalmology & visual science,* vol. 50, pp. 4337-4341, 2009.

[18] D. C. Rodger, A. J. Fong, W. Li, H. Ameri, A. K. Ahuja, C. Gutierrez, *et al.*, "Flexible parylene-based multielectrode array technology for high-density neural stimulation and recording," *Sensors and Actuators B: Chemical,* vol. 132, pp. 449-460, 6/16/ 2008.

[19] S. Corbett, J. Ketterl, and T. Johnson, "Polymer-Based Microelectrode Arrays," *MRS Online Proceedings Library,* vol. 926, pp. null-null, 2006.

[20] S. Takeuchi, T. Suzuki, K. Mabuchi, and H. Fujita, "3D flexible multichannel neural probe array," *Journal of micromechanics and microengineering,* vol. 14, p. 104, 2004.

[21] K.-K. Lee, J. He, A. Singh, S. Massia, G. Ehteshami, B. Kim, *et al.*, "Polyimide-based intracortical neural implant with improved structural stiffness," *Journal of Micromechanics and Microengineering,* vol. 14, p. 32, 2004.

[22] N. A. Blum, B. G. Carkhuff, H. K. Charles Jr, R. L. Edwards, and R. A. Meyer, "Multisite microprobes for neural recordings," *Biomedical Engineering, IEEE*

Transactions on, vol. 38, pp. 68-74, 1991.

[23] L. Licklider, X.-Q. Wang, A. Desai, Y.-C. Tai, and T. D. Lee, "A micromachined chip-based electrospray source for mass spectrometry," *Analytical Chemistry*, vol. 72, pp. 367-375, 2000.

[24] X.-Q. Wang and Y.-C. Tai, "A normally closed in-channel micro check valve," in *Micro Electro Mechanical Systems, 2000. MEMS 2000. The Thirteenth Annual International Conference on*, 2000, pp. 68-73.

[25] J. Xie, J. Shih, and Y.-C. Tai, "Integrated surface-micromachined mass flow controller," in *Micro Electro Mechanical Systems, 2003. MEMS-03 Kyoto. IEEE The Sixteenth Annual International Conference on*, 2003, pp. 20-23.

[26] J. Xie, Y. Miao, J. Shih, Q. He, J. Liu, Y.-C. Tai, *et al.*, "An electrochemical pumping system for on-chip gradient generation," *Analytical chemistry*, vol. 76, pp. 3756-3763, 2004.

[27] J. Xie, J. Shih, and Y.-C. Tai, "Integrated parylene electrostatic peristaltic pump," *Proceedings of Micro TAS*, pp. 865-868, 2003.

[28] R. Pitwon, C. Smith, K. Wang, J. Graham-Jones, D. R. Selviah, M. Halter, *et al.*, "Polymer optical waveguides with reduced in-plane bend loss for electro-optical PCBs," in *SPIE OPTO*, 2012, pp. 82640Z-82640Z-10.

[29] E. Meng, P.-J. Chen, D. Rodger, Y.-C. Tai, and M. Humayun, "Implantable parylene MEMS for glaucoma therapy," in *Microtechnology in Medicine and Biology, 2005. 3rd IEEE/EMBS Special Topic Conference on*, 2005, pp. 116-119.

[30] P.-J. Chen, D. C. Rodger, E. Meng, M. S. Humayun, and Y.-C. Tai, "Implantable unpowered parylene MEMS intraocular pressure sensor," in *Microtechnologies in Medicine and Biology, 2006 International Conference on*, 2006, pp. 256-259.

[31] R. L. White, L. A. Roberts, N. E. Cotter, and O.-H. Kwon, "THIN-FILM ELECTRODE FABRICATION TECHNIQUESa," *Annals of the New York Academy of Sciences*, vol. 405, pp. 183-190, 1983.

[32] R. N. Dean, J. Weller, M. J. Bozack, C. L. Rodekohr, B. Farrell, L. Jauniskis, *et al.*, "Realization of ultra fine pitch traces on LCP substrates," *Components and Packaging Technologies, IEEE Transactions on*, vol. 31, pp. 315-321, 2008.

[33] H.-I. Kuo, R. Zhang, and W. H. Ko, "Development of micropackage technology for biomedical implantable microdevices using parylene C as water vapor barrier coatings," in *Sensors, 2010 IEEE*, 2010, pp. 438-441.

[34] W. Li, D. C. Rodger, E. Meng, J. D. Weiland, M. S. Humayun, and Y.-C. Tai,

"Wafer-level parylene packaging with integrated RF electronics for wireless retinal prostheses," *Microelectromechanical Systems, Journal of,* vol. 19, pp. 735-742, 2010.

[35] J. Hetke, K. Najafi, and K. Wise, "Flexible miniature ribbon cables for long-term connection to implantable sensors," *Sensors and Actuators A: Physical,* vol. 23, pp. 999-1002, 1990.

[36] J. S. Ordonez, C. Boehler, M. Schuettler, and T. Stieglitz, "Improved polyimide thin-film electrodes for neural implants," in *Engineering in Medicine and Biology Society (EMBC), 2012 Annual International Conference of the IEEE*, 2012, pp. 5134-5137.

[37] *Vecstar® Kuraray LCP Film*. Available: http://www.kuraray.co.jp/en/products/medical/pdf/vecstar_catalog.pdf

[38] *SUMIKASUPER LCP Technical Note*. Available: http://www.sumitomo-chem.co.jp/sep/english/products/pdf/lcp_technote_e.pdf

[39] *Product Bulletin - PI 2525, PI 2555 & PI 2574*. Available: http://hdmicrosystems.com/HDMicroSystems/en_US/pdf/PI-2525_2555_2574_ProductBulletin.pdf

[40] *Parylene Properties & Characteristics*. Available: http://vp-scientific.com/parylene_properties.htm

[41] *STABLE DIMENSIONS, HIGH-TEMPERATURE PERFORMANCE IN THIN-WALLED APPLICATIONS*. Available: http://www.celanese.com/engineered-materials/products/Vectra-LCPZenite-LCP.aspx

[42] C. Hassler, T. Boretius, and T. Stieglitz, "Polymers for neural implants," *Journal of Polymer Science Part B: Polymer Physics,* vol. 49, pp. 18-33, 2011.

[43] *Vectra® liquid crystal polymer (LCP)*. Available: http://www.hipolymers.com.ar/pdfs/vectra/diseno/Vectra%20brochure.pdf

[44] S. H. Bae, J.-H. Che, J.-M. Seo, J. Jeong, E. T. Kim, S. W. Lee*, et al.*, "In Vitro Biocompatibility of Various Polymer-Based Microelectrode Arrays for Retinal Prosthesis," *Investigative Ophthalmology & Visual Science*, vol. 53, pp. 2653-2657, May 1, 2012 2012.

[45] M. J. Braeckel. *How High Performance Liquid Crystal Polymers Cut the Cost of Precision Medical Parts*. Available: http://www.hipolymers.com.ar/pdfs/vectra/aplicaciones/LCP_Medical_Costres72dpi.pdf

[46] B. Canale and V. J. Notorgiacomo. *Medical Advancements through Miniaturization with Liquid Crystal Polymer – at a Cost Savings*. Available: http://tools.ticona.com/tools/documents/literature/LCP_MedCost_revi-10.pdf

[47] S. W. Lee, K. S. Min, J. Jeong, J. Kim, and S. J. Kim, "Monolithic encapsulation of implantable neuroprosthetic devices using liquid crystal polymers," *Biomedical Engineering, IEEE Transactions on,* vol. 58, pp. 2255-2263, 2011.

[48] A.-V. Pham, "Packaging with liquid crystal polymer," *Microwave Magazine, IEEE,* vol. 12, pp. 83-91, 2011.

[49] X. Wang, J. Engel, and C. Liu, "Liquid crystal polymer (LCP) for MEMS: processes and applications," *Journal of Micromechanics and Microengineering,* vol. 13, p. 628, 2003.

[50] K. Aihara, M. J. Chen, C. Chen, and A.-V. Pham, "Reliability of liquid crystal polymer air cavity packaging," *Components, Packaging and Manufacturing Technology, IEEE Transactions on,* vol. 2, pp. 224-230, 2012.

[51] K. S. Min, S. H. Oh, M.-H. Park, J. Jeong, and S. J. Kim, "A Polymer-Based Multichannel Cochlear Electrode Array," *Otology & Neurotology,* vol. 35, pp. 1179-1186, 2014.

[52] S. J. Kim, "Cochlear Implant - Stimulation IC Design for Neural Prostheses," in *IEEE International Solid-State Circuits Conference,* San Francisco, CA, 2010.

[53] J. H. Kim, K. S. Min, S. K. An, J. S. Jeong, S. B. Jun, M. H. Cho*, et al.*, "Magnetic Resonance Imaging Compatibility of the Polymer-based Cochlear Implant," *Clinical and Experimental Otorhinolaryngology,* vol. 5, pp. S19-S23, 2012.

[54] J. Ordonez, M. Schuettler, C. Boehler, T. Boretius, and T. Stieglitz, "Thin films and microelectrode arrays for neuroprosthetics," *MRS bulletin,* vol. 37, pp. 590-598, 2012.

[55] W. Chun, N. Chou, S. Cho, S. Yang, and S. Kim, "Evaluation of sub-micrometer parylene C films as an insulation layer using electrochemical impedance spectroscopy," *Progress in Organic Coatings,* vol. 77, pp. 537-547, 2// 2014.

[56] M. Ohring, *Reliability and failure of electronic materials and devices*: Academic Press, 1998.

[57] *Manufacturing Cost*. Available: http://en.wikipedia.org/wiki/Manufacturing_cost

[58] T. Stöver and T. Lenarz, "Biomaterials in cochlear implants," *GMS current topics in otorhinolaryngology, head and neck surgery,* vol. 8, 2009.

[59] J. Maurer, N. Marangos, and E. Ziegler, "Reliability of cochlear implants,"

Otolaryngology-Head and Neck Surgery, vol. 132, pp. 746-750, 2005.

[60] *Matters Flyer*. Available: http://s3.medel.com/downloadmanager/downloads/maestro/en-UK/20930_Matters_Flyer_English.pdf

[61] C. A. Miller, P. J. Abbas, and B. K. Robinson, "Characterization of wave I of the electrically evoked auditory brainstem response in the guinea pig," *Hearing research,* vol. 69, pp. 35-44, 1993.

[62] R. T. Miyamoto, "Electrically evoked potentials in cochlear implant subjects," *The Laryngoscope,* vol. 96, pp. 178-185, 1986.

[63] K. Aihara, M. J. Chen, C. Cheng, and A. V. H. Pham, "Reliability of liquid crystal polymer air cavity packaging," *Components, Packaging and Manufacturing Technology, IEEE Transactions on,* vol. 2, pp. 224-230, 2012.

[64] K. Gilleo, J. Belmonte, and G. Pham-Van-Diep, "Low ball BGA: a new concept in thermoplastic packaging," in *Electronics Manufacturing Technology Symposium, 2004. IEEE/CPMT/SEMI 29th International*, 2004, pp. 345-354.

[65] K. Najafi, "Micropackaging Technologies for Integrated Microsystems: Applications to MEMS and MOEMS," 2003, pp. 1-19.

[66] M. Côté, P. Ferron, F. Bergeron, and R. Bussières, "Cochlear reimplantation: causes of failure, outcomes, and audiologic performance," *The Laryngoscope,* vol. 117, pp. 1225-1235, 2007.

[67] *Cochlear -brazing for a comeback*. Available: http://www.macrobusiness.com.au/2011/12/cochlear-brazing-for-a-comeback/

[68] A. J. Kinloch, *Adhesion and adhesives: science and technology*: Springer, 1987.

[69] A. S. Widge, "Self-assembled Monolayers of Polythiophene'molecular Wires': A New Electrode Technology for Neuro-robotic Interfaces," Carnegie Mellon University, The Robotics Institute, 2007.

[70] Z. H. Cho, Y. D. Son, H. K. Kim, K. N. Kim, S. H. Oh, J. Y. Han*, et al.*, "A fusion PET-MRI system with a high-resolution research tomograph-PET and ultra-high field 7.0 T-MRI for the molecular-genetic imaging of the brain," *Proteomics,* vol. 8, pp. 1302-23, Mar 2008.

[71] R. Bhidayasiri, J. M. Bronstein, S. Sinha, S. E. Krahl, S. Ahn, E. J. Behnke*, et al.*, "Bilateral neurostimulation systems used for deep brain stimulation: in vitro study of MRI-related heating at 1.5 T and implications for clinical imaging of the brain,"

Magnetic Resonance Imaging, vol. 23, pp. 549-555, 2005.

[72] S. A. Mohsin, N. M. Sheikh, and A. Maalik, "The effect of the MRI radiofrequency field on medical leads embedded beneath skin tissue," in *Electromagnetics in Advanced Applications (ICEAA), 2010 International Conference on*, 2010, pp. 513-516.

[73] M. Tagliati, J. Jankovic, F. Pagan, F. Susatia, I. U. Isaias, and M. S. Okun, "Safety of MRI in patients with implanted deep brain stimulation devices," *Neuroimage*, vol. 47 Suppl 2, pp. T53-7, Aug 2009.

[74] S. P. Gubbels and S. O. McMenomey, "Safety study of the Cochlear Nucleus 24 device with internal magnet in the 1.5 Tesla magnetic resonance imaging scanner," *Laryngoscope*, vol. 116, pp. 865-71, Jun 2006.

[75] O. Majdani, M. Leinung, T. Rau, A. Akbarian, M. Zimmerling, M. Lenarz*, et al.*, "Demagnetization of cochlear implants and temperature changes in 3.0T MRI environment," *Otolaryngol Head Neck Surg*, vol. 139, pp. 833-9, Dec 2008.

[76] C. Vincent, I. Ruzza, F. M. Vaneecloo, and F. Dubrulle, "Magnetic resonance imaging with the Digisonic SP Neurelec cochlear implant," *Eur Arch Otorhinolaryngol*, vol. 265, pp. 1043-6, Sep 2008.

[77] O. Majdani, T. S. Rau, F. Gotz, M. Zimmerling, M. Lenarz, T. Lenarz*, et al.*, "Artifacts caused by cochlear implants with non-removable magnets in 3T MRI: phantom and cadaveric studies," *Eur Arch Otorhinolaryngol*, vol. 266, pp. 1885-90, Dec 2009.

[78] A. L. James, S. J. Daniel, L. Richmond, and B. C. Papsin, "Skin breakdown over cochlear implants: prevention of a magnet site complication," *The Journal of otolaryngology*, vol. 33, pp. 151-154, 2004.

[79] R. J. Fretz and R. P. Fravel, "Design and function: a physical and electrical description of the 3M House cochlear implant system," *Ear and hearing*, vol. 6, pp. 14S-19S, 1985.

[80] O. Adunka, J. Kiefer, M. H. Unkelbach, T. Lehnert, and W. Gstoettner, "Development and evaluation of an improved cochlear implant electrode design for electric acoustic stimulation," *The Laryngoscope*, vol. 114, pp. 1237-1241, 2004.

[81] D. L. Tucci, M. H. Merson, and B. S. Wilson, "A Summary of the Literature on Global Hearing Impairment: Current Status and Priorities for Action," *Otology & Neurotology*, vol. 31, pp. 31-41 10.1097/MAO.0b013e3181c0eaec, 2010.

[82] J. Cavuoto, G. Cornett, W. Grill, and D. Pope, "The market for neurotechnology: 2010–2014," *Neurotech Reports*, 2009.

국문 초록

기존의 신경보철장치 (neural prostheses)와 마찬가지로 현재의 인공와우 또는 인공달팽이 (cochlear implant) 시스템은 티타늄 합금을 이용한 밀봉패키지와 귀금속 와이어를 이용해 제작되는 전극을 이용한다. 티타늄 케이스를 밀봉하기 위해서는 브레이징 (brazing), 저항용접 (resistive welding), 레이저 용접 (laser welding) 등 복잡하고 높은 숙련도가 요구되는 패키징 기술이 요구된다. 또한 패키지가 커지고 두꺼워지게 된다. 와이어 기반 전극 또한 숙련공들에 의해 현미경을 이용한 수작업으로 제작된다. 따라서, 높은 재료비, 인건비가 요구되며 결과적으로 높은 판매가격이 형성된다. 이러한 높은 가격은 인공와우 장치가 개발도상국 (developing countries)으로 확대 보급되는 것을 제한하는 결과를 야기한다. 뿐만 아니라 기존의 인공와우 시스템은 두꺼운 금속패키지에 의해 MRI와 호환되지 않는 문제점이 있다. 본 연구에서는 액정폴리머 (liquid crystal polymer)를 이용하여 저가이면서도 유효성, 신뢰성, MRI 호환성이 뛰어난 새로운 폴리머 기반 인공와우를 개발하였다. 액정폴리머는 생체적합성 (biocompatibility)이 뛰어날 뿐만 아니라 기존에 주로 사용되어온 폴리이미드 (polyimide), 패릴린-C (parylene-C)와 달리 낮은 수분흡수율을 보이므로 장기간 신뢰성이 높은 장치를 구현할 수 있다. 본 연구에서는 액정폴리머를 기반으로 함몰형 공간 (recessed cavity)을

이용한 새로운 카드형태의 패키징 방법을 개발하였다. 기존의 패키징 방법은 메탈 지그와 열성형을 이용하여 고온의 녹는점을 갖는 액정폴리머 커버부를 미리 성형한 뒤 별도의 저온 액정폴리머를 접착층으로 사용하여 고온 액정폴리머 기판부와 라미네이션하는 방법을 사용하였다. 열성형을 통해 생성된 액정폴리머 커버부의 공간은 PDMS와 같은 물질로 채워져야 하므로 라미네이션 시에 이 부분을 냉각하는 별도의 장치가 필요하였다. 새롭게 개발된 함몰형 공간을 이용한 패키징 방법에서는 전자부품이 위치할 함몰형 공간을 레이저 커팅 된 여러 장의 저온 액정폴리머 필름을 쌓아서 생성한 뒤 라미네이션하는 방법을 사용한다. 모든 층이 동일한 액정폴리머 물질로 구성되며 별도의 접착층이나 열성형 과정 없이 라미네이션을 수행할 수 있으므로, 얇고 작은 카드 형태의 패키지를 구현할 수 있다. 본 연구에서는 개발된 패키징 기술과 연구실에서 개발된 액정폴리머 기반 16 채널 달팽이관 전극을 이용하여 액정폴리머 기반의 초소형 인공와우 시스템을 개발하였다.

제작된 액정폴리머 기반 인공와우 장치의 유효성은 장치를 동물모델에 이식한 후 전기자극 뇌간유발반응 (electrically evoked auditory brainstem response)을 측정함으로써 검증하였다. 또한 3.0 T, 7.0 T MRI 촬영을 통해 개발된 액정폴리머 기반 인공와우 장치가 기존의 티타늄 기반 장치보다 높은 호환성을 보임을 확인하였다.

또한 본 연구에서는 액정폴리머 기반 장치의 장기간 신뢰성

을 더욱 높이기 위해서 나노 다공 표면 (nanoporous surface)과 마이크로 스케일의 장벽 (microscale barrier)으로 구성된 새로운 누설장벽 구조를 제안하였다. 누설장벽 구조는 전극 사이트를 통한 수분 침투 경로의 길이와 복잡도를 증가 시킬 뿐만 아니라, 폴리머 커버부와 금속층 사이의 기계적 결합력을 증가시키는 역할을 한다. 개발된 누설장벽 구조의 신뢰성은 가속 수명 담금 시험 (accelerated lifetime soak test)을 통해 검증하였다. 시험 결과 누설장벽 구조의 나노 다공 표면과 마이크로 스케일 장벽이 폴리머 기반 전극의 수명에 기여한다는 것을 확인하였다. 110 °C 가속 수명 담금 시험에서는 누설장벽 구조를 갖는 전극샘플이 대조군 (나노다공 표면과 마이크로 스케일 장벽이 없는 샘플)에 비해 예측수명이 약 2배 높은 결과를 보였다.

개발된 액정폴리머 기반 인공와우의 세부적인 가격구성 및 절감요인을 파악하기 위하여 장치의 제조가격 분석을 수행하였다. 또한 연구실에서 산학협력을 통해 개발하여 2010년 식약처 승인을 받은 티타늄 기반 인공와우 장치의 제조가격을 분석하여 액정폴리머 기반 장치의 제조가격과 비교, 분석하였다. 액정폴리머 기반 장치가 티타늄 기반 장치에 비해 직접 재료비, 직접 인건비 등 모든 카테고리에서 현저히 낮게 분석되었다. 액정폴리머 기반 장치 1개당 제조가격은 티타늄 기반 장치의 약 10%에 불과하였다. 또한 이 제조가격은 생산량 증가에 따라 규모의 경제가 적용되어 더욱 감소함을 확인하였다. 따라서 저가이면서도 유효성, 신뢰성, MRI 호환성이 뛰어난 액정폴리머 기반 인공와우는 개발 도상국

등에 인공와우장치를 널리 보급할 수 있는 단초가 될 수 있다.

주요어: 인공와우, 액정폴리머, 저가, 이식형 패키지, 밀봉 패키지, 장기간 신뢰성, MRI 호환성, 폴리머 기반 신경보철장치

학 번: 2008-30871